Geoscience Laser Altimeter System (GLAS)

Algorithm Theoretical Basis Document
Version 3.0

PRECISION ATTITUDE DETERMINATION (PAD)

Prepared by

Sungkoo Bae
Noah Smith
Bob E. Schutz

Center for Space Research
The University of Texas at Austin

February 2012

Contents

GLOSSARY **3**

1 INTRODUCTION **4**
1.1 GLAS Measurement Requirement 4
1.2 GLAS Attitude/Pointing Requirement 6
1.3 Outline of Document 8

2 FUNDAMENTALS OF ATTITUDE DETERMINATION **11**
2.1 Coordinate Systems 11
2.2 Quaternion Representation 12
2.3 Kinematic Equations of Spacecraft Attitude 15
2.4 Dynamical Equations of Spacecraft Attitude 16
2.5 Attitude Determination Problem 17

3 MEASUREMENT SYSTEM **19**
3.1 CCD Star Tracker 19
3.1.1 HD-1003 Star Tracker 21
3.1.2 Star Measurement on CCD Star Tracker 21
3.1.3 Star Tracker Data Simulation 24
3.2 Hemispherical Resonator Gyro (HRG) 28
3.2.1 Gyro Model 28
3.2.2 Gyro Data Simulation 28
3.3 Star Catalog 29
3.3.1 Star Catalog for Star Field Simulation 29
3.3.2 Star Catalog for Real Application 31
3.3.3 Corrections of Star Measurement 32

4 STAR IDENTIFICATION **33**
4.1 Pattern Matching Algorithm 33
4.1.1 Sectioning of Star Catalog 33
4.1.2 Algorithm 35
4.1.3 Misidentification 38
4.1.4 Simulation Results 41
4.2 Direct Match Technique (DMT) 42
4.2.1 Algorithm 42
4.2.2 Catalog Star Search 44
4.2.3 Simulation Results 45

5 ATTITUDE DETERMINATION **47**
5.1 Single Frame Attitude Determination 47
5.2 Extended Kalman Filter 52
5.2.1 Basic Algorithm 52
5.2.2 Observation Model 54
5.2.3 Kalman Filter Update 55
5.3 Batch Method 56
5.4 Simulation Results 57

6 POINTING DETERMINATION **64**
6.1 POINTING DETERMINATION ALGORITHM 64
6.1.1 Estimation of the LRS frame in terms of the SCF 66
6.1.2 Absence of the LRC Star 68
6.1.3 LPA measurement projection into LRS frame 68
6.1.4 40 Hz LPA measurements 72
6.1.5 Collimated Reference Source (CRS) 73
6.2 Spacecraft Velocity Influence on Laser Pointing 73
6.3 Systematic Errors 75
6.3.1 Systematic Errors in the Stellar Reference System 75
6.3.2 Systematic Errors in Attitude Determination 75

7 IMPLEMENTATION CONSIDERATIONS **78**
7.1 Standards 78
7.2 Ancillary Inputs 79
7.3 Accuracy and Validation 79
7.4 Computational: CPU, Memory and Disk Storage 80
7.5 Sensor Failures 80

BIBLIOGRAPHY **85**

ACKNOWLEDGMENTS **86**

Appendix A ICESAT MISSION OUTLINE **87**

Appendix B PROCESSING METHODS FOR POINTING DETERMINATION **89**
B.1 IST Bracket Motion 89
B.2 Time-tag Problems in IST and SIRU Data 90
B.3 IST Sun-Blinding 90
B.4 Distortion Correction 90
B.5 Bad Star Removal 92

Appendix C LPA IMAGE CHARACTERISTICS **93**

Appendix D PROPERTIES OF QUATERNION **103**

GLOSSARY

ATBD	Algorithm Theoretical Basis Document
BD	Boresight Direction
BST	Ball (or Bus) Star Tracker
CCD	Charge Coupled Device
CRF	Celestial Reference Frame
CRS	Collimated Reference Source
DMT	Direct Match Technique
EKF	Extended Kalman Filter
FOAM	Fast Optimal Attitude Method
FOV	Field of View
GCF	Gyro Coordinate Frame
GSFC	Goddard Space Flight Center
HP	Hewlett Packard
HRG	Hemispherical Resonator Gyro
ICRF	International Celestial Reference Frame
IERS	International Earth Rotation Service
IPD	Improved Polar Decomposition
IST	Instrument Star Tracker
ITER	Iteration Method
ITRF	International Terrestrial Reference Frame
LPA	Laser Profiling Array
LRC	Laser Reference Camera
LRS	Laser Reference Sensor
LRT	Laser Reference Telescope
LTR	Lateral Transfer Retroreflector
MFOAM	Modified Fast Optimal Attitude Method
MSX	Midcourse Space Experiment
OBF	Optical Bench Coordinate Frame
PAD	Precision Attitude Determination
PD	Polar Decomposition
PMA	Pattern Matching Algorithm
POD	Precision Orbit Determination
QUEST	Quaternion Estimator
SCF	Star Tracker Coordinate Frame
SFAD	Single Frame Attitude Determination
SIRU	Space Inertial Reference Unit
SRS	Stellar Reference System
SVD	Singular Value Decomposition
TRF	Terrestrial Reference Frame
UVF	Unit Vector Filter

Chapter 1

INTRODUCTION

The Geoscience Laser Altimeter System (GLAS) instrument is planned to be launched on the *Ice, Cloud and land Elevation Satellite* (ICESAT) in January 2003 as a part of the Earth Observing System (EOS) of NASA. The primary purpose of the GLAS mission is to make ice sheet elevation measurements in the polar regions which will be used to determine the mass balance of the ice sheets and their contributions to global sea level change [41]. In addition, the measurements will meet science objectives to support atmospheric science, and land topography application. The laser altimeter will measure the height from the spacecraft to Greenland and Antarctic ice sheets to support investigations of the secular change in surface elevation, as well as annual, interannual, and other temporal variations. To support the science requirements to determine temporal elevation change, the measurements by the GLAS instrumentation must be very accurate. The ICESAT orbit will be near-circular (eccentricity = 0.0013), with a semimajor axis of 6970 km, and it will be near polar, with an inclination of 94°, in order to fly over Greenland and Antarctica. The orbit is frozen so that the mean perigee is fixed near the north pole. The GLAS/ICESAT has a 3 year lifetime requirement with a 5 year goal. The EOS program plans for follow-on satellites to extend the science data set to 15 years and longer.

1.1 GLAS Measurement Requirement

The GLAS Science Requirements [60] provide the error budget for the instrument and ancillary information necessary to meet the science requirements. The most stringent requirements are needed for the cryosphere objectives. For example, the accuracy of elevation change in the vicinity of the West Antarctic Ross ice streams is 1.5 cm/yr in a 100×100 km^2 area where surface slopes are $< 0.6°$. In summary, the error budget allows 10 cm instrument precision, 5 cm radial orbit position, 7.5 cm laser pointing knowledge and 2 cm or less for other error contributors. The GLAS orbit position will be obtained with the Global Positioning System (GPS) and ground-based Satellite Laser Ranging (SLR). In addition to the geocentric position vector, the accurate determination of the altimeter beam pointing angle in an Earth-fixed Terrestrial Reference Frame (TRF) is also required for high-precision satellite laser altimetry. The laser altimeter will provide the range between the spacecraft and the illuminated spot on the Earth surface by measuring the round-trip travel time of the laser pulse. A one arcsecond error in the laser pointing direction produces a 5 cm range measurement error from a 600 km spacecraft altitude on

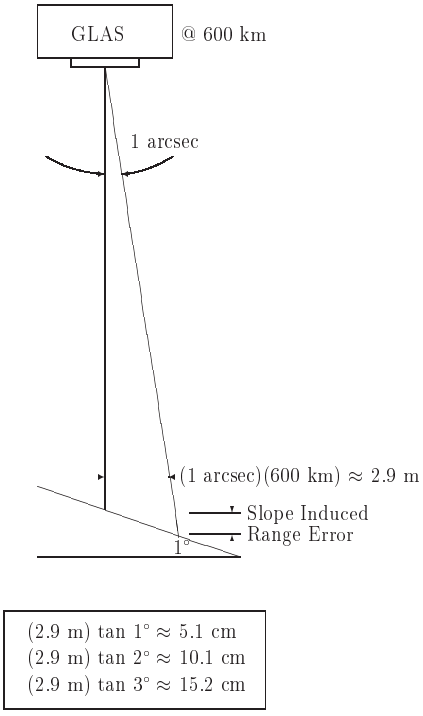

Figure 1.1: Surface slope induced range errors by one arcsecond pointing error

a 1° slope of the Earth's surface at the illuminated point(Figure 1.1). Therefore, to be able to interpret the laser altimeter height measurements with the required accuracy, it is required to determine the laser beam pointing direction to better than 1.5 arcsecond (1σ), which corresponds to a 7.5 cm range error, in post-processing.

The laser pointing direction is measured with respect to the spacecraft body-fixed frame. The GLAS precision attitude determination will first provide the orientation of spacecraft body-fixed axes, or attitude, with respect to a Celestial Reference Frame (CRF) by star cameras and gyros, to a high degree of accuracy. A specially designed Stellar Reference System (SRS) [60] will measure the pointing angle of the GLAS laser beam to better than 1.5 arcsecond (1σ) with respect to the star field for every laser shot fired with a frequency of 40 Hz. Calibrated knowledge of the laser pointing direction with respect to the spacecraft body-fixed axes, combined with the GLAS geocentric position vector, and the measured round trip travel time for the laser pulse enable determination of both the spot location on the Earth's surface and, hence, the surface elevation with respect to the adopted TRF. Figure 1.2 illustrates how the GLAS instrument can measure the illuminated surface and the surface's elevation.

In this document, which is known as the Precision Attitude Determination (PAD) Algorithm Theoretical Basis Document (ATBD), we are focusing on the determination of the pointing direction from the spacecraft to the laser illuminated surface spot in terms

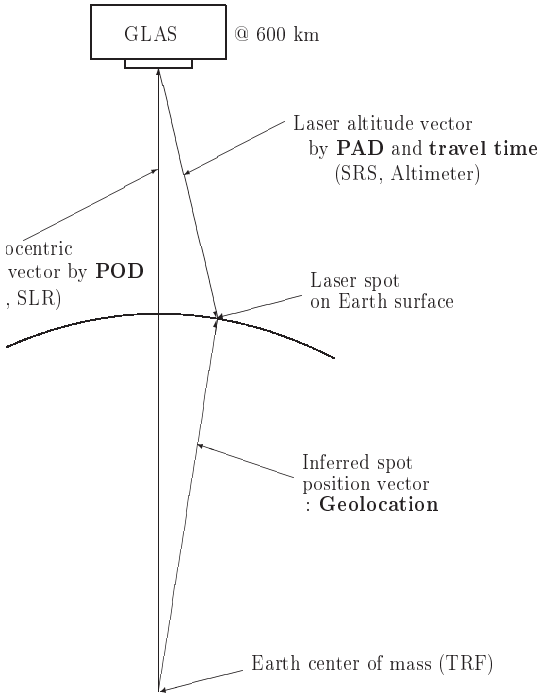

Figure 1.2: Illustration of the GLAS laser altimeter measurement

of direction cosines (or unit vector). The laser travel time will give the scalar distance between the GLAS measurement reference point and the surface spot. Combining this scalar distance with the direction cosines gives the laser altitude vector. Since the GLAS measurement reference point is not coincident with the spacecraft center of mass from which the geocentric position vector is measured, the displacement must be taken into account when the GLAS position vector is combined with the laser altitude vector to get the laser spot position vector. The detailed procedure for geolocating the spot illuminated by the GLAS laser is described in the Laser Footprint Location (Geolocation) and Surface Profiles ATBD [42].

1.2 GLAS Attitude/Pointing Requirement

Attitude generally refers to the angular orientation of a defined body-fixed coordinate system with respect to a separately defined external reference frame, such as a CRF. The term, spacecraft attitude, is generally related to the spacecraft body-fixed coordinate frame whose origin is the spacecraft center of mass. However, all the instruments related to the PAD will be attatched to the GLAS optical bench. Consequently, the more convenient choice for the origin of the body-fixed coordinate frame is an instrument reference point positioned at the optical bench and the corresponing coordinate frame will define the

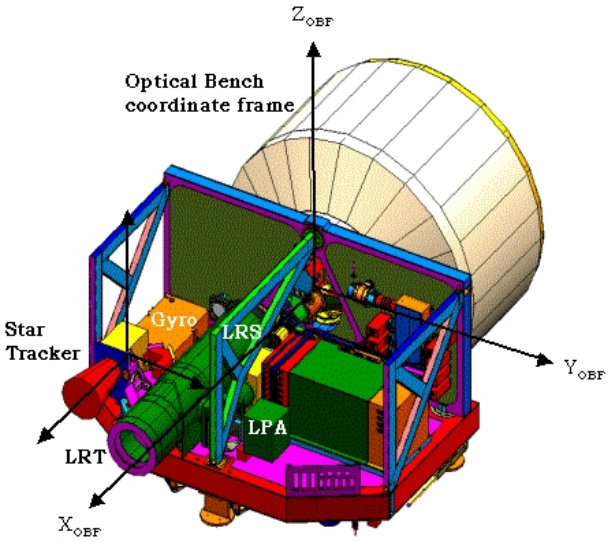

Figure 1.3: Stellar Reference System on the GLAS

optical bench attitude as a replacement of the common spacecraft attitude. Thoughout this document, we are basically concerned with the optical bench attitude for the GLAS, rather than the spacecraft attitude. Spacecraft attitude is sometimes mentioned, but it is an alternative terminology for the optical bench attitude when we discuss the GLAS PAD. *Attitude determination* refers to the process of determining the angular orientation of the spacecraft-fixed axes or optical bench axes from measurements obtained by various attitude sensors. This determination of attitude uses data from appropriate sensors and a sophisticated processing of the sensor data.

Laser *pointing*, in contrast, refers to the direction of the transmitted laser pulse with respect to spacecraft-fixed axes or in an Earth-fixed coordinate system. *Pointing determination* of the GLAS refers to the process of determining the laser pointing at a 40 Hz rate in a selected coordinate system. Once the laser pointing is determined in the spacecraft-fixed axes, it will be transformed to the vector in the adopted CRF using the determined optical bench attitude or an Earth-fixed TRF using the proper transformation between CRF and TRF. (Most coordinate systems involved in the GLAS PAD, including CRF and TRF, will be described in Section 2.1.) The pointing variation of the laser beam, stemming from both the instrument alignment change with respect to the optical bench axes and the laser's own shot to shot fluctuation, will be determined using the SRS specially designed for the GLAS PAD (Figure 1.3).

As will be seen in Chapter 6, the SRS requires the optical bench attitude for the determination of the laser pointing vector. In the process, the accuracy of the estimated

Table 1.1: Error Budget of the Stellar Reference System

Error Sources (RSS)	1σ **error**
total Laser Reference System errors	0.72 arcsecond
total unmeasured errors	0.45 arcsecond
total attitude determination system Errors	0.85 arcsecond
TOTAL SRS RSS ERRORS	**1.20 arcsecond**

attitude directly affects the quality of the laser pointing determination. Table 1.1 shows the simplified error budget of the SRS [60] when all of the error sources in the system are taken into account. Our simulation results, based on the algorithm introduced in this document, showed a strong effect of the attitude uncertainty on the overall laser pointing error. To meet the laser pointing knowledge requirement of 1.5 arcsecond (1σ), the optical bench attitude must be determined with an accuracy of better than one arcsecond.

Due to the essentially fixed position on the celestial sphere, a star is one of the best external sources to provide a reference for attitude determination. The star sensor, the attitude sensor which measures relative star positions, currently enables us to determine the spacecraft attitude with one arcsecond accuracy level. Among several different star sensors, the Charge Coupled Device (CCD) equipped star tracker has been the most recent development to provide multiple star images in a single measurement frame. The GLAS attitude system includes a Raytheon Optical System Inc.(ROSI) HD-1003 star tracker as the primary attitude sensor in order to achieve the required one arcsecond (or better) accuracy. Additionally, the Hemispherical Resonator Gyros (HRG) will provide continuously measured angular rates associated with spacecraft attitude changes. The measured angular rates support the attitude propagation between star tracker measurements and the attitude prediction when no stars are available. The star tracker and gyros will be mounted on a rigid optical bench of the GLAS instrument; thus, this tracker is referred to as the optical bench star tracker or the instrument star tracker.

Two Ball CT-602 star trackers, products of Ball Aerospace, will be mounted on the spacecraft structure to support real time attitude determination and control. In the nominal 600 km altitude orbit, the GLAS Attitude Control System (ACS) must continually change the spacecraft orientation with respect to the CRF to maintain a near-nadir laser pointing direction. Thus, magnetic torquers and momentum wheels must change the orientation by 223 arcsec/sec with respect to the stars, which define inertial directions. The real time attitude knowledge requirement of the ICESAT is 20 arcseconds (1σ) or better. The Ball CT-602 star trackers' data are intended to be used in the PAD with the optical bench star tracker or as a backup unit to the optical bench star tracker. The study in this document will only utilize the optical bench star tracker.

1.3 Outline of Document

The main purpose of this document is to describe the algorithm that has been developed for the GLAS precision attitude and pointing determination, while the title of the document, PAD, only expresses attitude determination. The overview of the process for the optical bench attitude determination is illustrated in Figure 1.4 and briefly described here

based on the figure. At the first step, raw data received from the orbiting GLAS should be converted to data written in engineering units. After the conversion, the stars observed by the star tracker need to be identified from a star catalog using a priori attitude knowledge, in order to determine the star coordinates in a CRF defined by the star catalog. Stellar aberrations due to the spacecraft velocity with respect to the barycenter of the solar system should be corrected before we actually use the identified star coordinates in attitude determination algorithms. Modified Fast Optimal Attitude Method (MFOAM) and Quarternion Estimator (QUEST) are deterministic approaches for the attitude determination using vector measurements. Attitude parameters determined by these methods can be used for quality check of the star tracker measurement data. The optical bench attitude of ICESat GLAS is determined using star tracker and gyro data, and Extended Kalman Filter estimation.

The next four chapters are related to the attitude data processing shown in Figure 1.4 except the fact that the conversion of the raw data to engineering units will not be covered in this document. In Chapter 2, fundamental coordinate systems, basic attitude equations and well-known attitude problems are introduced. The primary attitude sensors for the GLAS are the optical bench star tracker and gyro, which are reviewed in Chapter 3. The simulation algorithms for star tracker and gyro data are also described in Chapter 3. As a part of the attitude determination system, the star catalog is described in Section 3.3. The star identification algorithm and simulation results are discussed in Chapter 4. In Chapter 5, several deterministic and statistical methods for attitude determination are introduced. The simulation results from various methods are presented in Chapter 5. In Chapter 6, the implementation of the SRS for the laser pointing determination is discussed and some simulation results are presented.* Systematic errors which are imbedded in the GLAS PAD system, but intentionally ignored in the previous chapters, will be fully discussed. Chapter 7 will address problems related to the actual implementation of the attitude/pointing determination system in the GLAS. Quaternions, the preferred set of attitude parameters are reviewed in Appendix D as an extension of Chapter 2.

*An alternative algorithm was used in practice due to degraded performance of the SRS. The new algorithm is described in Appendix B.

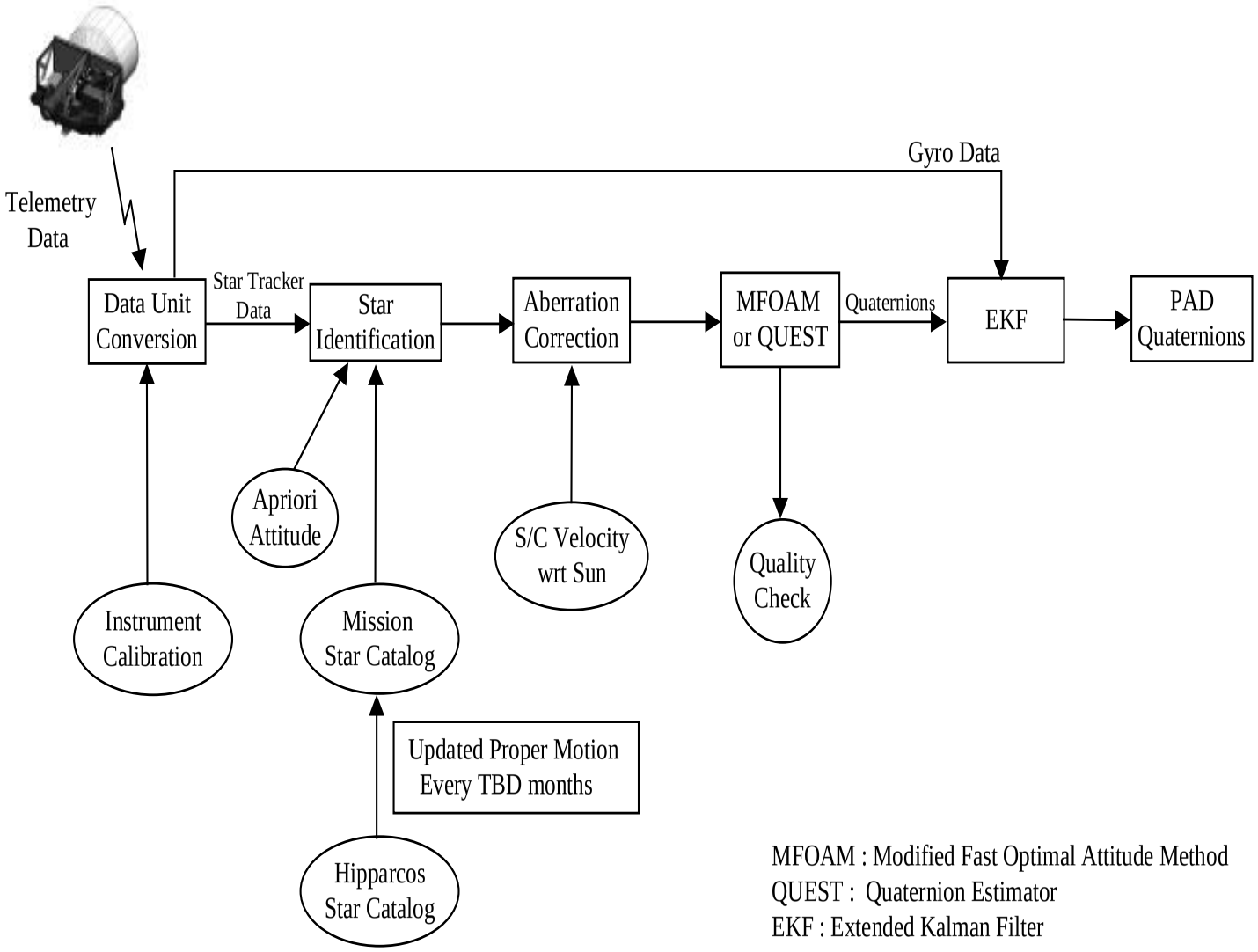

Figure 1.4: Attitude determination overview

Chapter 2

FUNDAMENTALS OF ATTITUDE DETERMINATION

2.1 Coordinate Systems

It is presumed that all of the following coordinate systems have a common origin in the spacecraft except for the Terrestrial Reference Frame. The relevant coordinate systems are :

- **Optical Bench Coordinate Frame (OBF)**
  The OBF is a coordinate frame fixed in the optical bench and is used to define the optical bench attitude. The origin of the OBF is an instrument reference point located at the optical bench. The orientation of each instrument attached to the optical bench will usually be described in terms of the OBF. The OBF x-axis is nominally coincident with the optical bench star tracker boresight direction, which is zenith pointing. The other two axes complete the proper orthogonal system. The adopted OBF for the GLAS is illustrated in Fig 1.3. To maximize the solar arrays' power generation, the ICESAT will be operated in two nominal attitude modes [36]. The velocity direction of the ICESAT will change between the OBF $\pm z$-axis and the $\pm y$-axis, controlled by yaw maneuvers. Througout this document, z_{OBF} axis is perpendicular to the orbital plane (upward) and y_{OBF} completes the proper orthogonal system. Since the definition of the OBF used here is not the same as the definition of the planned OBF in Fig 1.3, the appropriate coordinate transformation should be applied before actually using the developed algorithm. The angle rotations about the (x, y, z)-axes of the OBF are frequently named yaw, roll, and pitch angles, respectively. The term, spacecraft attitude, will actually mean the optical bench attitude for the GLAS instrument in this document.

- **Celestial Reference Frame (CRF)**
  The CRF is a non-rotating coordinate frame defined by appropriate celestial objects. Ultimately, it is the inertial reference system which all the other coordinate systems are referred to. The simplified description of the CRF can be : the X axis is to the vernal equinox direction of a specified date, and Y axis is in the equator and the Z axis completes the proper orthogonal system. The CRF will be realized by the International Celestial Reference Frame (ICRF) maintained by the International

Earth Rotation Service (IERS).

- **Star Tracker Coordinate Frame (SCF)**
  The SCF is the coordinate frame fixed to the star tracker mounted on the GLAS optical bench. The direction perpendicular to the star tracker field of view (FOV) at the center of it is called the boresight direction (BD). While the narrow FOV star tracker such as the HD-1003 can give precise knowledge for the direction of the BD vector, it gives relatively poor information about the rotation of the BD vector. For the precise determination of the laser altimeter pointing direction, therefore, the BD of the optical bench star tracker will be aiming at the zenith direction, which is the opposite direction that laser altimeter will be pointing. For our description, the z_{SCF} is aligned to the BD, the x_{SCF} is toward the orbit normal (downward, being equal to the nominal $-z_{OBF}$), and the y_{SCF} completes the proper orthogonal system (the nominal y_{OBF}). The orientation of the SCF with respect to the OBF will change slowly due to the local deformation of the optical bench and the internal error of the star tracker itself. The alignment of the SCF in terms of the OBF is assumed to be *fixed* for the attitude determination process in Chapter 5. The alignment variations and the corresponding calibrations will be discussed along with the SRS in Chapter 6.

- **Gyro Coordinate Frame (GCF)**
  The definition of the GCF is similar to that of the SCF in the sense that the orientation is defined with respect to the OBF. The GCF may be defined by the axes of three orthogonal gyros (usually including a redundant one) in a package, which is often called the Inertial Reference Unit (IRU). In this document, we simplify the GLAS attitude system by assuming the GCF to be coincident with the OBF. The GCF and the OBF may not coincide in the real GLAS attitude system, however, the results from this document will not be affected by the change of the GCF orientation with respect to the OBF, as long as both GCF and OBF are orthogonal coordinate systems.

- **Terrestrial Reference Frame (TRF)**
  The TRF is an Earth-fixed coordinate frame whose origin is coincident with the center of mass of the Earth. Ultimately, the laser spot location on the Earth's surface will be described in the International Terrestrial Reference Frame (ITRF).

2.2 Quaternion Representation

The attitude of the three axis stabilized spacecraft is most conveniently thought of as a rotation matrix which transforms a set of reference axes in inertial space to the axes in the spacecraft OBF. The rotation matrix is an orthonormal matrix and is also called a *direction cosine matrix* or an *attitude matrix*.

Three Euler angles may be used to represent the orientation of a rigid body since the rotational motion of the rigid body has three degrees of freedom. There are twelve possible sets of Euler angles by the sequence of axes to be rotated. The 3-1-3 Euler angles, which rotate the body about the third axis first, the first axis next and the third axis last in newly defined coordinate axes obtained by sequential rotations, have been particularly popular

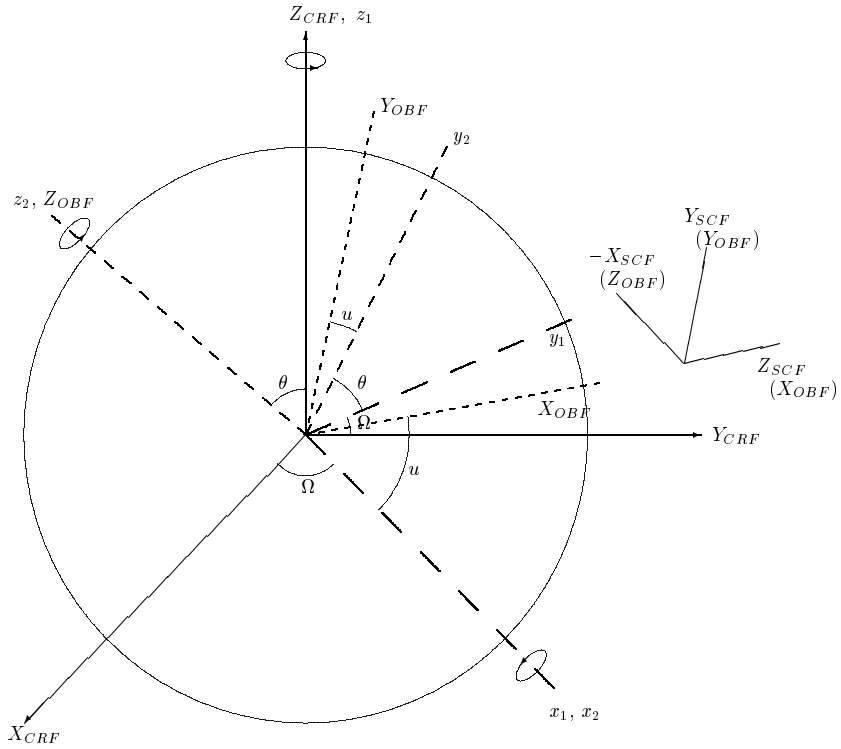

Figure 2.1: Coordinate frames

for attitude determination and control. These Euler angles are shown in Figure 2.1 where the coordinate frames are illustrated.

Although the Euler angles are visually helpful to understand the rotational motion of a spacecraft, there is a disadvantage in the Euler angles which is known as a *singularity* or *gimbal lock* [18]. The 3-1-3 Euler angles are singular when the second Euler angle is 0° or 180°, because of ambiguous determination of the other two Euler angles. The singularity occurs in any sequence of Euler angles and makes Euler angles only infrequently the best choice in attitude determination and control application.

In most modern attitude determination and control, four element *quaternions*, also called *Euler parameters*, are predominantly used. Their wide use has been the result of the following advantages :

- No geometric singularities
- Rigorous satisfaction of a set of linear differential equations.
- No requirement for the evaluation of trigonometric functions

The lack of trigonometric functions in the computation of quaternions is clearly an advantage in time-critical real time operations. Extensive use of trigonometric function in

Euler angles will significantly increase the computation time, especially with modest performance computers such as those used in on-board applications. The quaternions are defined based on Euler's rotation theorem [18] :

> *The most general displacement of a rigid body with one point fixed is equivalent to a single rotation about some axis through that point.*

For some axis, $\hat{e}$, and a single rotation angle, $\Delta\theta$, the quaternions are defined by

$$\begin{aligned} q_1 &= e_x \sin(\frac{\Delta\theta}{2}) \\ q_2 &= e_y \sin(\frac{\Delta\theta}{2}) \\ q_3 &= e_z \sin(\frac{\Delta\theta}{2}) \\ q_4 &= \cos(\frac{\Delta\theta}{2}) \end{aligned} \tag{2.1}$$

where e_x, e_y and e_z are components of rotation axes in terms of the OBF before the rotation. Since there are only three degrees of freedom for the rotational motion, the following constraint exists in the quaternion representation :

$$q_1^2 + q_2^2 + q_3^2 + q_4^2 = 1 \tag{2.2}$$

The single constraint to be observed is a minor disadvantage associated with the four quaternions. The detailed properties of quaternions and relevant equations are summarized in Appendix D.

The quaternion errors δq are frequently represented by another quaternion rotation, which must be composed with the estimated quaternions $\hat{q}$ in order to obtain the true quaternions q_{true} as

$$q_{true} = \delta q \otimes \hat{q}, \tag{2.3}$$

where the quaternion composition, $\otimes$, is defined in Equation D.9. A benefit of this error representation can be seen by applying the small angle approximations to Equation 2.1 :

$$\begin{aligned} \delta q_1 &= \frac{\theta_x}{2} \\ \delta q_2 &= \frac{\theta_y}{2} \\ \delta q_3 &= \frac{\theta_z}{2} \\ \delta q_4 &= 1, \end{aligned} \tag{2.4}$$

where θ_x, θ_y, and θ_z were defined in the previous section as yaw, roll, and pitch angles, respectively. Only the vector components of quaternions (see Equation D.1) correspond to angle errors and the scalar component becomes insignificant to the first order. By applying inverse quaternions (Equation D.2) to Equation 2.3, the error quaternions are expressed as

$$\delta q = q_{true} \otimes \hat{q}^{-1}. \tag{2.5}$$

Even though the Euler angles are not convenient for numerical computations, their geometrical significance in illustrating the rotational motion is more apparent than quaternions. Therefore, they are often used for computer input/output and for analysis. In this research, simulated attitude data were created by Euler angles and, then, converted to the quaternions using Equation D.13. Euler angles can be recalculated from estimated quaternions by Equation D.14.

2.3 Kinematic Equations of Spacecraft Attitude

If the quaternion composition (Equation D.9) is performed successively in time, the time evolution of quaternions during the time interval Δt is given by

$$q(t + \Delta t) = q(\Delta t) \otimes q(t). \tag{2.6}$$

Let ω_x, ω_y and ω_z be the components of angular velocity vector ($\vec{\omega}$) at time t, $|\omega|$ be the magnitude of the angular velocity, and $\Delta\theta$ be a rotation angle during Δt. From the definition of quaternions, we can derive

$$q(t + \Delta t) = [\frac{\cos(\Delta\theta)}{2} I_{4\times4} + \frac{\sin(\Delta\theta)}{2} \frac{\Omega(\vec{\omega})}{|\omega|}]q(t), \tag{2.7}$$

where $\Omega(\vec{\omega})$ is

$$\Omega(\vec{\omega}) \equiv \begin{bmatrix} 0 & \omega_z & -\omega_y & \omega_x \\ -\omega_z & 0 & \omega_x & \omega_y \\ \omega_y & -\omega_x & 0 & \omega_z \\ -\omega_x & -\omega_y & -\omega_z & 0 \end{bmatrix}. \tag{2.8}$$

This equation predicts the attitude at the future time based on the knowledge of the current attitude if the axis of rotation is invariant over the time interval Δt. If the average or instantaneous angular velocity of a spacecraft is known during Δt, the rotation angle is

$$\Delta\theta = |\omega|\Delta t \tag{2.9}$$

about the rotation axis. Assuming Δt is small enough, the small angle approximations

$$\cos\frac{\Delta\theta}{2} \approx 1, \qquad \sin\frac{\Delta\theta}{2} \approx \frac{1}{2}\omega\Delta t \tag{2.10}$$

lead to the attitude differential equation

$$\frac{d}{dt}q(t) = \frac{1}{2}\Omega(\omega(t))q(t) \tag{2.11}$$

from Equation 2.7. Equation 2.11 is the fundamental kinematic equation for the attitude determination and can be rearranged in a different order such that [12]

$$\frac{d}{dt}q = \frac{1}{2}\begin{bmatrix} q_4 & -q_3 & q_2 & q_1 \\ q_3 & q_4 & -q_1 & q_2 \\ -q_2 & q_1 & q_4 & q_3 \\ -q_1 & -q_2 & -q_3 & q_4 \end{bmatrix}\begin{bmatrix} 0 \\ \omega_x \\ \omega_y \\ \omega_z \end{bmatrix}. \tag{2.12}$$

Conversely,

$$\begin{aligned}
\omega_x &= 2(q_4\dot{q}_1 + q_3\dot{q}_2 - q_2\dot{q}_3 - q_1\dot{q}_4) \\
\omega_y &= 2(-q_3\dot{q}_1 + q_4\dot{q}_2 + q_1\dot{q}_3 - q_2\dot{q}_4) \\
\omega_z &= 2(q_2\dot{q}_1 - q_1\dot{q}_2 + q_4\dot{q}_3 - q_3\dot{q}_4).
\end{aligned} \tag{2.13}$$

For reference, the 3-1-3 Euler angle representation for angular velocity is

$$\begin{aligned}
\omega_x &= \dot{\psi}\ \sin\phi\ \sin\theta + \dot{\theta}\ \cos\phi \\
\omega_y &= \dot{\psi}\ \cos\phi\ \sin\theta - \dot{\theta}\ \sin\phi \\
\omega_z &= \dot{\psi}\ \cos\theta + \dot{\phi},
\end{aligned} \tag{2.14}$$

where ψ, θ and ϕ are three Euler angles in the sequential order.

2.4 Dynamical Equations of Spacecraft Attitude

The rotational motion of a body about its center of mass is

$$\frac{d\vec{h}}{dt} = \vec{T}, \tag{2.15}$$

where $\vec{T}$ is an applied torque and $\vec{h}$ is an angular momentum vector. With $\vec{h}$ described in the spacecraft body-fixed axes, it follows that

$$\dot{\vec{h}}_{OBF} + \vec{\omega} \times \vec{h}_{OBF} = \vec{T}, \tag{2.16}$$

where $\vec{\omega}$ is again an angular velocity vector. Expanding the above equation gives the general Euler equations of attitude :

$$\begin{aligned}
\dot{h_x} + \omega_y h_z - \omega_z h_y &= T_x \\
\dot{h_y} + \omega_z h_x - \omega_x h_z &= T_y \\
\dot{h_z} + \omega_x h_y - \omega_y h_x &= T_z,
\end{aligned} \tag{2.17}$$

where h_x, h_y, h_z are the angular momentum components along the OBF, and T_x, T_y, T_z are the body referenced external torque components. For the solution of these equations, the external torque of $\vec{T}$ must be modeled as a function of time as well as a function of the position and attitude of the spacecraft. The dominant sources of attitude disturbance torques are the Earth's gravitational and magnetic fields, solar radiation pressure, and aerodynamic drag [65].

In many spacecraft, gyros are grouped as an IRU. When the gyros are used to measure the angular velocity of the spacecraft, the numerical or analytical expression for external torques is not necessary. Angular velocities measured by gyros are substituted directly into the kinematic equation (Equation 2.11) for attitude prediction. Such gyro measurements actually include the effect of all torques acting on the spacecraft. Force model errors in this situation will exist only to the extent that the measurements from a gyro unit contain errors. Since the HRG will provide the measurement for the angular rate of the ICESAT, the Euler equations are not required for the attitude determination. The attitude determination in the event of gyro failure will be discussed in Chapter 5.

2.5 Attitude Determination Problem

The minimum required knowledge for three-axis attitude determination is the direction vectors to two celestial objects which are represented in the OBF (or the Spacecraft Body-Fixed Coordinate Frame generally) and are also known in the reference frame, such as the CRF. Since the stars are measured in the SCF, the unit vectors in the OBF are determined using the rotation matrix between two coordinate systems. Denote the two unit vector measurements by $\hat{W}_1$ and $\hat{W}_2$ in the OBF and $\hat{V}_1$ and $\hat{V}_2$ in the CRF. To obtain $\hat{V}_1$ and $\hat{V}_2$, the measured stars in the SCF must be identified in a given star catalog with the star identification algorithms developed in Chapter 4. A simple attitude determination problem is given as :

Find an attitude matrix A, to satisfy

$$\hat{W}_1 = A\hat{V}_1, \qquad \hat{W}_2 = A\hat{V}_2, \tag{2.18}$$

where the measured vectors and the catalog vectors require

$$\hat{W}_1 \cdot \hat{W}_2 = \hat{V}_1 \cdot \hat{V}_2 \tag{2.19}$$

within the measurement and the catalog error bound.

A simple algorithm to find the attitude matrix from any two vector measurements is called TRIAD [49] or an *algebraic method* [65]. The method has been applied for at least three decades and was employed in several missions, usually for coarse attitude determination. Whereas it is relatively easy to evaluate the TRIAD attitude matrix, it has many disadvantages. The most serious disadvantage might occur when more than three unit vectors are observed simultaneously, which is a common case in CCD star tracker measurements. (In Section 4.1, three observation vectors are the minimum number for utilizing a pattern matching algorithm.)

To take advantage of multiple unit vectors simultaneously obtained by a CCD star tracker (or the combination of multiple sensors), a least squares attitude problem was suggested in the early 1960's by Wahba [64]. The well-known *Wahba Problem* is :

Find the proper orthogonal matrix A that minimizes the loss function, J(A),

$$J(A) = \frac{1}{2}\sum_{i=1}^{n} a_i |\hat{W}_i - A\hat{V}_i|^2, \tag{2.20}$$

where the unit vectors $\hat{V}_i$ are representations in a reference frame of the directions to some observed objects, the $\hat{W}_i$ are the unit vector representations of corresponding observations in the spacecraft body frame, the a_i are positive weights, and n is the number of observations

The *Wahba Problem* is basically a weighted least squares problem for the attitude matrix, A. It is also known to be equivalent to a maximum likelihood estimation problem for a

simple, but realistic probabilistic model for vector measurements [46]. For error-free observations (and also error-free catalog positions), the true attitude matrix A_{true} will drive the loss function, $J(A)$, to be zero. In a practical situation, the A must be found that minimizes $J(A)$. The solutions of the *Wahba Problem*, which are deterministic approaches to the computation of the attitude matrix (or quaternions) will be introduced in Chapter 5.

Chapter 3

MEASUREMENT SYSTEM

Many spacecraft use gyro units to continuously measure their angular velocities. Traditional mechanical gyros react to the motion of the host spacecraft based on the principle of conservation of angular momentum. Non-mechanical gyros have been constructed on physical phenomena such as general relativity or the inertial vibration property of a standing vibration wave on a hemispherical body. Such gyros are usually sensitive to high frequency noise and able to measure attitude change very accurately. However, slowly drifting gyro biases will produce deviations of predicted attitude from true attitude. Some external sources such as the Sun, the Moon, the Earth and stars must be observed in order to prevent gyro biases from deteriorating the attitude determination process based on gyros. Measurements from external sources are relatively insensitive to the high frequency of attitude change due to instrument noise and jitter. However, such measurements provide good information in the low frequency of attitude motion because the positions of celestial objects are well-predicted (Sun, Moon, and Earth) or they are essentially fixed in space (stars). Therefore, gyros and sensors for the external sources are generally used together in the attitude determination system.

The CCD star tracker which measures multiple stars with a frequency of 10 Hz also enables angular rate information to be inferred and may be used alone for the accurate attitude determination. However, in reality, the high frequency jitter in the spacecraft motion, the irregular distribution of stars, CCD limitations for data read-out and the blockage of star measurements due to the Sun or the Moon require measurements of the spacecraft angular velocity from gyros for continuous attitude determination.

This chapter introduces CCD star trackers and gyros which will be used in the ICESAT/GLAS. In addition, a star catalog which is an essential component of the attitude determination using star sensors will be discussed.

3.1 CCD Star Tracker

The CCD image detector was developed in 1970 by Boyle and Smith at Bell Laboratories [10]. Unlike the traditional light detectors, two-dimensional CCD detectors allow one to obtain images of several objects in a single exposure and provide much better photometric accuracy than photometric emulsions do. In structure, the CCD is a two dimensional array of photo-detectors, and each individual detector is described as a picture element or pixel (see Figure 3.1). After a period of being exposed to light, called the integration

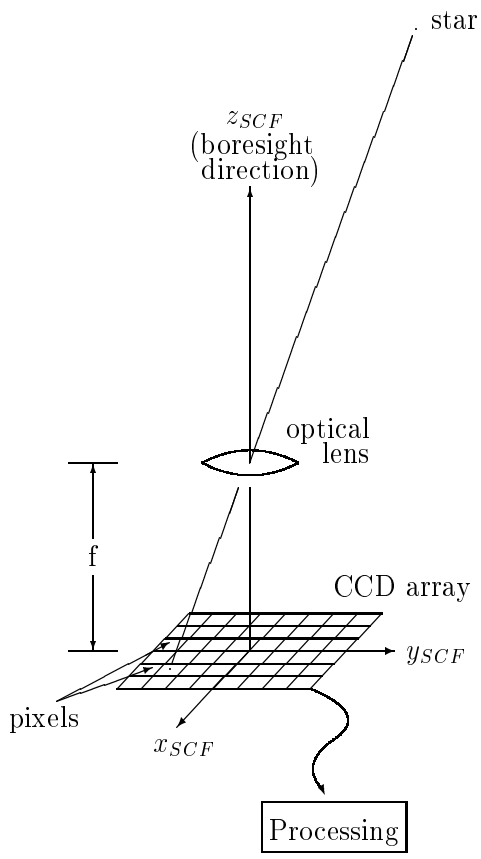

Figure 3.1: Simple illustration of the CCD star tracker

time, the photocharges in each pixel are transferred to an output stage by the external manipulation of voltages. The charges are measured, digitized and read into a computer's memory one pixel at a time, row by row. The area viewed by a two dimensional CCD array can be quickly reconstructed as a digitized image in a computer in order to analyze or process the light intensity distribution of an extended field. The high quantum efficiency of the CCD allows it to record about 60% of the photons falling on each pixel. The reconstructed image is extremely similar to the area projected onto the CCD due to the direct relationship between the exposure and the intensity of the recorded image over a broad range of exposures from threshold to saturation. Since each pixel represents a specific location on the CCD, a computer can be programmed to perform an analysis of a star field automatically. More detailed knowledge of the CCD can be obtained from many sources [10] [21] [57].

In space applications, CCDs have been used on many imaging missions including the Hubble Space Telescope. The CCD star tracker was developed in the late 1970's and it has recently begun to be used in space missions as a component in state-of-the-art attitude determination hardware. The traditional star sensor detects only one or two stars in its FOV, and therefore, has been used with other types of attitude hardware like Sun sensors,

horizon sensors or magnetometers. Since the CCD star tracker observes multiple stars simultaneously, it is sometimes referred to as a *star camera* and some spacecraft use a CCD star tracker as the sole attitude sensor except for initial attitude acquisition in real time applications. Even though the initial attitude acquisition may require other sensors for coarse attitude determination, this may be also performed by a star tracker with a wide FOV [33] [24]. A simplified illustration of the CCD array and lens in the star tracker is shown in Figure 3.1. The following sections describe characteristics of commercially available CCD star trackers.

3.1.1 HD-1003 Star Tracker

For the PAD of the GLAS, the Raytheon Optical System Inc.(ROSI) HD-1003 [11], a CCD star tracker, will be mounted on the instrument optical bench. It is an electro-optical sensor that implements CCD array detectors to search for and track up to six stars in an $8° \times 8°$ FOV with an array of 512×512 pixels. The star tracker operates at a 10 Hz rate, thereby measuring coordinates of tracking stars as well as their light intensities every 0.1 second. It provides the position of a star with a six arcseconds (1σ) error in each axis of pitch and roll. A magnitude measurement is given within 0.2 magnitude (1σ) uncertainty. The nominal sensitivity range of the star magnitude is between 2.0 and 6.0. Functionally, the HD-1003 star tracker is operated in search and track mode. The star tracker searches the entire FOV to find the six brightest stars in search mode. After acquisition, it continues tracking these stars and periodically computes updated angular positions as the stars pass across the FOV in track mode. The performance characteristics of the ROSI HD-1003 are summarized and compared to the characteristics of the Ball CT-601 and the Lockheed AST in Table 3.1.

The HD-1003 star tracker manufactured by Raytheon for GLAS was tested during the period between summer 1999 and spring 2000. Various tests were conducted, such as mechanical properties measurement, spectral calibration, thermal vacuum segment and acceptance vibration. Table 3.2 shows the results of the final performance test which was performed in an air conditioned room after electronics and software upgrades [13]. The static accuracy test measures the position accuracy of stars that are fixed relative to the tracker. The dynamic accuracy test measures the star location accuracy while tracking a moving star at a rate of 0.20 deg/second. The table presents only the post-vibration results, but the pre-vibration results showed similar values. All requirements were reported to have been met based on the pass/fail criteria specified in both pre/post vibration. The overall performance of the HD-1003 was not compromised by exposure to the random vibration, thermal or vacuum environment. After the final performance test, point sources were generated by the Scene Simulator computer in order to simulate multiple stars for the tracking performance test. For the Scene Simulator test, six stars were simultaneously placed in the full FOV ($8 \times 8°$) and one star in the reduced FOV ($0.5 \times 0.5°$). No test failures or anomalies were encountered during the testing.

3.1.2 Star Measurement on CCD Star Tracker

In the focused image on a CCD array, a star will appear as a point source because all luminous power from the star will end up in one pixel. By slightly defocusing the image, however, a star will cover several pixels, usually in an area of 3×3 or 4×4 pixels [59].

Table 3.1: Characteristics of the commercial star trackers [11] [7] [62]. The performance parameters of the Ball CT-602 is identical to the CT-601 except the weight and the power requirement.

CHARACTERISTICS	**HD-1003**	**CT-601**	**AST †**
Field of View	$8^\circ \times 8^\circ$	$8^\circ \times 8^\circ$	$8.8^\circ \times 8.8^\circ$
Sensitivity Range (M_v)	+2 to +6	+1 to +6	+7.5
Accuracy (arcsec, 1σ) ‡ in Roll and Pitch	6	3 (bias) 5 (random)	1
Update Rate (Hz)	10	10	10 or 5
Acquisition Time (Full Field, second)	6	5	N/A
Maximum Number of Stars Tracked	6	5	20
Maximum Power (W)	12 (average)	<10 @28V d.c.	4(0°)/7(50°)
Maximum Weight	8 lb (with shade)	18 lb (w/o shade)	3.5 kg (w/o shade)
Operating Temperature ($^\circ C$)	-20 to +60	-30 to +50	-30 to +50

† development goals
‡ Yaw is worse

The size of the illuminated square area will be determined by the brightness of each star. From the illuminated pixels, the centroid is mathematically computed with an accuracy of 0.1 pixel level [21]. The summation of transferred charges on those pixels is proportional to the brightness of the star, from which the instrumental magnitude of the star can be computed. Only the pixels that receive more than a certain amount (threshold) of photons will be recorded. Dimmer stars will be difficult to detect due to the increased noise. If the star is too bright, saturation may occur due to overflow of the photons to adjacent pixels. The sensitivity range of star magnitude is between 2.0 and 6.0 visual magnitude for the HD-1003. The central position of the star image can be determined precisely using the techniques such as *Image Moment Analysis* (up to the level of $\frac{1}{10}$) or *1-Dimensional Marginal Fitting* ($\frac{1}{20}$ pixel or better). The *Point Spread Function* [21] is the method to discriminate the overlapped stars in some pixels.

The two angles of star position measured by the star tracker are converted to a unit vector, $\vec{S}_{SCF}$, in the SCF, where the BD is regarded as the third axis. Then, the coordinates in the SCF are transformed to those in the OBF using the transformation matrix, M :

$$\vec{S}_{SCF} = M\vec{S}_{OBF}, \tag{3.1}$$

where $\vec{S}_{OBF}$ is the unit vector of the same star in the OBF. The transformation matrix M

Table 3.2: Test results of HD-1003 star tracker from final performance tests. The specific requirements were given for GLAS. For the dynamic accuracy test, the star position error is effectively *rms* of bias and random noise.

Star Position Error

Error Type	Source Magnitude	Requirement (1σ per axis)	Measured ROW axis error (1σ)	Measured COL axis error (1σ)
static bias	3.0 m_i	$\leq$ 4.5 arcsec	1.23 arcsec	1.28 arcsec
	5.5 m_i	$\leq$ 4.5 arcsec	2.44 arcsec	2.60 arcsec
static random noise	3.0 m_i	$\leq$ 3.3 arcsec	0.94 arcsec	0.54 arcsec
	5.5 m_i	$\leq$ 3.3 arcsec	2.53 arcsec	2.16 arcsec
dynamic *rms*	5.5 m_i	$\leq$ 5.0 arcsec	2.95 arcsec	3.23 arcsec

Magnitude Error

Error Type	Source Movement	Source Magnitude	Required	Measured error
3σ repeatability	static	3.0 m_i	$\leq$ 0.24 m_i	0.12 m_i
	static	5.5 m_i	$\leq$ 0.24 m_i	0.12 m_i
	dynamic	5.5 m_i	$\leq$ 0.24 m_i	0.18 m_i
bias	static	3.0 m_i	$\pm$ 0.12 m_i	-0.02 m_i
	static	5.5 m_i	$\pm$ 0.12 m_i	0.01 m_i
	dynamic	5.5 m_i	$\pm$ 0.12 m_i	0.05 m_i

Boresight(Pitch & Roll) and Yaw Measurement Results

Measured Axis	Required Range	Measured Position	Required Knowledge	Measured Knowledge
Pitch	255.5 $\pm$ 3 pixels	254.780	$\pm$ 2 arcsec	$\pm$ 1.6 arcsec
Roll	255.5 $\pm$ 3 pixels	255.385	$\pm$ 2 arcsec	$\pm$ 1.6 arcsec
Yaw	$0° \pm 0.20°$	$-0.004°$	$\pm$ 10 arcsec	$\pm$ 3 arcsec

is determined in prelaunch instrument calibration, but it may be changed slightly by the launch loads and other effects like temperature variation and atmospheric drag in orbit. This is known as the star tracker alignment error that is also represented by the star tracker BD excursion.

Using the SRS, the GLAS laser beam pointing direction would be determined against the star field viewed by the star tracker that defines the SCF. In other words, the laser beam pointing direction can be directly associated with the SCF through the SRS. Therefore, knowledge of the orientation of the SCF, not the orientation of the OBF, in terms of the CRF is needed for the GLAS PAD. This fact will allow us to determine the orientation of the OBF with respect to the CRF under the assumption that the star tracker is rigid in terms of the OBF. This assumption will not restrict the implementation of the estimated attitude to the laser pointing determination, as will be described in Chapter 6.

3.1.3 Star Tracker Data Simulation

The orbit of the ICESAT is near-circular (eccentricity = 0.0013), with a semimajor axis of 6970 km and an inclination of 94°. The BD is assumed to look at the zenith which is opposite to the laser pointing direction. The misalignment of the BD to the laser pointing direction will be discussed in Chapter 6. The BD can be calculated in the CRF along the ICESAT orbit at a specified interval, such as 0.1 second. The $8° \times 8°$ FOV whose center is the BD is constructed by specifying the FOV boundary in right ascension (α) and declination (δ). The stars located in a FOV are found in a star catalog and only the brightest stars (up to six) are selected as *measured* stars by the CCD star tracker at each measurement time. The star positions (in α and δ) and star magnitudes are given as the input parameters for the simulation. A schematic of the procedure is given in Figure 3.2.

The stars are selected from the star catalog in which star positions are described in a CRF. Since the real star tracker measures stars in the SCF, it is necessary to transform the coordinates of the selected stars. The relations between coordinate frames, described in Section 2.1, are used for coordinate transformations. In our simulation configuration, it is assumed that the OBF is obtained by the 3-1-3 Euler angle rotation from the CRF (Figure 2.1). The Euler angles are the longitude of the ascending node, Ω, inclination, i, and the argument of latitude, u. These 3-1-3 Euler angle rotations align x_{OBF} with the BD, z_{OBF} with the orbit normal direction (upward), and y_{OBF} with the velocity vector direction. The SCF is obtained by simple rotation about y_{OBF} to make the z_{SCF} to be the BD of star tracker.

Thus, the selected stars from the star catalog, whose coordinates are given in terms of the CRF, are now transformed to the OBF and the SCF successively by the following procedure :

1. α and δ to unit vector
   First, the two angles in the CRF are converted to a unit vector in the CRF by

$$\begin{bmatrix} X \\ Y \\ Z \end{bmatrix} = \begin{bmatrix} \cos\delta\cos\alpha \\ \cos\delta\sin\alpha \\ \sin\delta \end{bmatrix}. \tag{3.2}$$

2. CRF to OBF
   The unit vector of the star in the CRF is transformed to the unit vector in the OBF

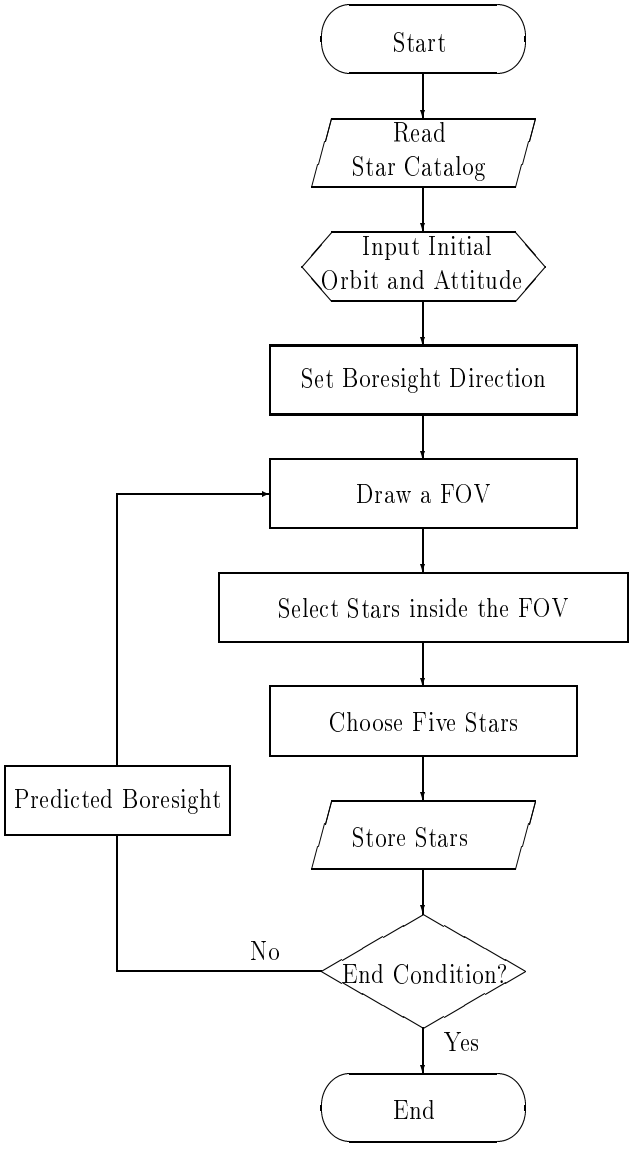

Figure 3.2: Flowchart of the star selection process for star tracker measurement data

through the 3-1-3 Euler angle rotations :

$$\begin{bmatrix} x_{OBF} \\ y_{OBF} \\ z_{OBF} \end{bmatrix} = \begin{bmatrix} \cos u & \sin u & 0 \\ -\sin u & \cos u & 0 \\ 0 & 0 & 1 \end{bmatrix} \begin{bmatrix} 1 & 0 & 0 \\ 0 & \cos i & \sin i \\ 0 & -\sin i & \cos i \end{bmatrix}$$
$$\begin{bmatrix} \cos \Omega & \sin \Omega & 0 \\ -\sin \Omega & \cos \Omega & 0 \\ 0 & 0 & 1 \end{bmatrix} \begin{bmatrix} X \\ Y \\ Z \end{bmatrix}. \tag{3.3}$$

The magnitude of Ω was varied in the simulation to comply with the 183 day repeat ground track of the ICESAT.

3. OBF to SCF
   The unit vector in the OBF is transformed to the unit vector in the SCF by the 90° rotation about y_{OBF}. This corresponds to the rotational matrix M defined in Equation 3.1. Then

$$\begin{bmatrix} x_{SCF} \\ y_{SCF} \\ z_{SCF} \end{bmatrix} = \begin{bmatrix} 0 & 0 & -1 \\ 0 & 1 & 0 \\ 1 & 0 & 0 \end{bmatrix} \begin{bmatrix} x_{OBF} \\ y_{OBF} \\ z_{OBF} \end{bmatrix}. \tag{3.4}$$

   This rotation aligns z_{SCF} with the BD, x_{SCF} with orbit normal direction (downward) and y_{SCF} completes the right hand coordinate system.

4. Unit vector to position angles (ϕ and λ)
   The two measurement angles, ϕ and λ, determined by the CCD star tracker are computed from the unit vector in the SCF. First, the focal length f (Figure 3.1) of the star tracker optical system is given in *millimeter*(mm) unit. If x_{mm} and y_{mm} are the distances to the star image from the center of the CCD array using the same mm units as f, the star position on the CCD detector array is given by

$$\begin{bmatrix} x_{mm} \\ y_{mm} \end{bmatrix} = \begin{bmatrix} x_{SCF}/z_{SCF} \times f \\ y_{SCF}/z_{SCF} \times f \end{bmatrix}. \tag{3.5}$$

   Then, the two measurement angles ϕ and λ in the SCF, analogous to α and δ in the CRF, are defined by

$$x_{mm} = \tan \phi \times f \tag{3.6}$$
$$y_{mm} = \tan \lambda \times \frac{f}{cos(\phi)}. \tag{3.7}$$

From the known noise characteristics of the CCD star tracker, noise components are added to ϕ and λ. A measurement noise is also added to the magnitude. A set of realistic noise characteristics for the GLAS star tracker are given in Table 3.3. The noisy position angles and magnitude in the SCF are considered to be the simulated measurements obtained by a star tracker. The purpose of the attitude determination that will be discussed in later chapters is to find input Euler angles which were used for data simulation. As mentioned in Chapter 2, quaternions will be used instead of Euler angles. The flowchart showing the procedure to get simulated star tracker data from the stars which were selected in a star catalog is illustrated in Figure 3.3.

Table 3.3: Some noise characteristics for the HD-1003 star tracker and the HRG [60]

Measurement	Noise (1σ)
HD-1003	
dim stars	7.3 arcseconds
bright stars	4.5 arcseconds
magnitude	0.2 magnitude
HRG	
Rate White Noise (RWN, σ_v)	0.05 arcsec/sec$^{\frac{1}{2}}$
Bias Stability (BS, σ_b)	1.33e-03 arcsec/sec
Rate Random Walk (RRW, σ_u)	3.19e-05 arcsec/sec$^{\frac{3}{2}}$

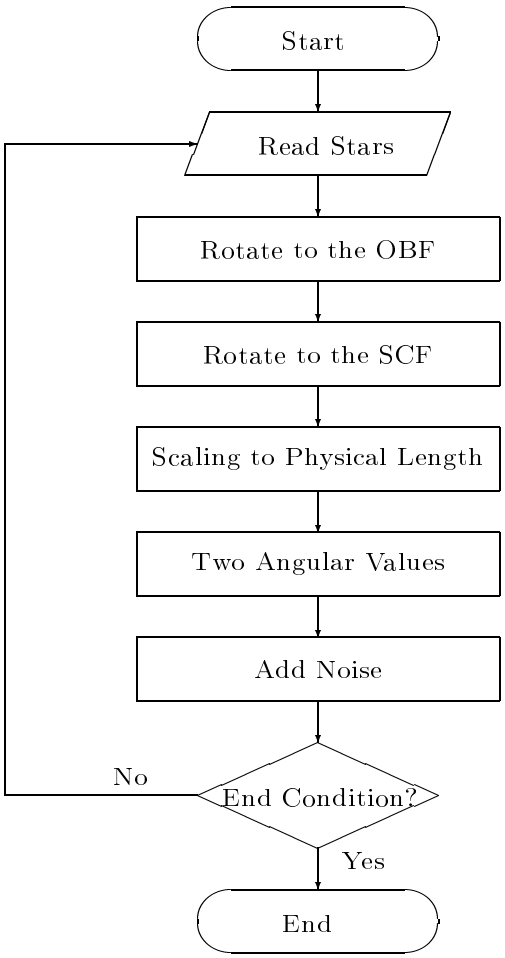

Figure 3.3: Flowchart of the star tracker data generation from the selected stars

3.2 Hemispherical Resonator Gyro (HRG)

Gyros provide the spacecraft angular rate, even though several independent technologies are used to design different gyros, such as the traditional mechanical gyro, laser gyros and the HRGs. The ICESAT will use a set of HRGs mounted on the instrument optical bench. An HRG is based on the inertial sensing property of a standing vibration wave on a hemispherical body [66]. It was noted that the location of a vibration pattern at the rim of a hemispherical shell precesses relative to a reference on the shell when the shell is rotated about its axis of symmetry. The vibration pattern precession was observed to be a constant fraction of the inertial input. Measuring the amount of precession provides the inertial rotation of the input axis. A carefully designed IRU consisting of a few HRGs provides the inherent small size, high reliability characteristics and precision performance with relatively long life time expected in space applications.

3.2.1 Gyro Model

Farrenkopf's gyro model [14] [65] has been widely accepted and used for many years. It basically separates the gyro noise into three noise types called electronic noise, float torque noise and float torque derivative noise. The electronic noise is a kind of scale factor error generated from electronic part of gyro. It is a colored noise, but it can be treated as white noise if the gyro time constant is much smaller than the gyro readout time interval, which is usually true for the modern gyros. The float torque noise (rate white noise) is simple white Gaussian noise superimposed on the gyro drift rate. The float torque derivative noise (drift rate ramp) is the cause of the gyro drift rate bias since its integration appears to be rate random walk. This gyro characteristic eventually causes the measured data to deviate systematically from the true angular rate and this is why gyros need help from the external sources such as star, Sun or Earth. The gyro rate bias, due to the float torque derivative, as well as the attitude parameters (e.g., quaternions) can be estimated with appropriate estimation algorithms.

3.2.2 Gyro Data Simulation

To keep the laser altimeter pointing direction to the nadir direction, the ICESAT must rotate about the orbit normal axis (z_{OBF}) once per orbital period. The nominal (and unperturbed) angular velocity with respect to the OBF can be assumed to be

$$\begin{bmatrix} \omega_x \\ \omega_y \\ \omega_z \end{bmatrix} = \begin{bmatrix} 0.0 \\ 0.0 \\ \frac{2\pi}{T} \end{bmatrix}, \tag{3.8}$$

where T is the orbital period of the ICESAT. However, when the attitude determination process is simulated for the multiple orbits of the ICESAT, the simple angular velocity in Equation 3.8 makes the CCD star tracker to repeatedly image the same group of stars. To avoid this unrealistic situation, Equation 2.14 is used to provide nominal angular velocity,

based on 3-1-3 Euler angle rotations from the CRF to the OBF :

$$\begin{aligned} \omega_x &= \dot{\Omega}\ \sin u\ \sin i + \frac{\mathrm{d}i}{\mathrm{d}t}\ \cos u \\ \omega_y &= \dot{\Omega}\ \cos u\ \sin i - \frac{\mathrm{d}i}{\mathrm{d}t}\ \sin u \\ \omega_z &= \dot{\Omega}\ \cos i + \dot{u}. \end{aligned} \tag{3.9}$$

The expected value of $\dot{\Omega}$ is approximately $0.5°/day$ for the ICESAT [26] and $\frac{\mathrm{d}i}{\mathrm{d}t}$ is zero by assuming the inclination of the spacecraft to be constant in the simulation.

To generate noisy gyro data, the expected gyro noises must be added. Assuming that the direction of the gyro's input axis is aligned with the OBF, the simulated (gyro-measured) angular velocity of the ith gyro, g_i, is obtained from *Farrenkopf's gyro model* [65] :

$$g_i = (1 + k_i)\,\omega_i + b_{i0} + b_i + \eta_{i1}, \tag{3.10}$$

where k_i is a scale factor error, ω_i is a true or nominal angular velocity, b_{i0} is an initial bias error, b_i is a gyro bias which is slowly varying in the orbit and η_{i1} is a white noise on gyro rate. The scale factor relates the gyro output counts to the physical unit measurements and is a function of the angular rate. Assuming that the $k_i\omega_i$ term is negligible in comparison with b_{i0} and b_i, Equation 3.10 reduces the gyro noise into white noise and random walk (non-white noise) components.

If the gyro measurement vector, $\vec{g}$, is measured in the GCF while other vectors are described in the OBF, then the vector form of Equation 3.10 becomes

$$\vec{g} = G\ (\vec{\omega} + \vec{b}_0 + \vec{b} + \vec{\eta}_1), \tag{3.11}$$

where $\vec{\omega}$ is the nominal spacecraft angular velocity vector in the OBF and G is an orthogonal matrix transforming the OBF into the GCF. The time varying gyro bias, $\vec{b}$, can be obtained by the following shaping filter :

$$\frac{d\vec{b}}{dt} = \vec{\eta}_2, \tag{3.12}$$

where $\vec{\eta}_2$ is another white noise uncorrelated to $\vec{\eta}_1$.

The noise characteristics of HRG under consideration for the ICESAT are given in Table 3.3. The components of Equation 3.11, such as $\vec{\eta}_1$, $\vec{b}_0$, and $\vec{b}$, can be derived from these values.

3.3 Star Catalog

3.3.1 Star Catalog for Star Field Simulation

The star catalog is a fundamental part of the attitude determination process that uses measurement data obtained from any type of star sensor. For the star field simulation, a star catalog, originally developed to support a spacecraft equipped with a Ball CT-601 star tracker, was obtained from the Smithsonian Astrophysical Observatory [56]. The star catalog contains 4853 stars and is a subset of *Yale Bright Star Catalog.* Two years of orbit simulation of ICESAT sampled the entire celestial sphere because of the complete rotation

Table 3.4: Probability of the number of stars in a FOV

Stars	**Whole Sky(4853)**		**South Pole(391)**		**North Pole(323)**	
	Poisson dist.(%)	Computer Simul.(%)	Poisson dist.(%)	Computer Simul.(%)	Poisson dist.(%)	Computer Simul.(%)
≤ 2	2.0	3.9	0.6	2.8	2.1	1.1
3	3.8	5.5	1.4	3.2	3.9	2.8
4	7.2	8.6	3.3	6.0	7.4	8.4
5	10.8	11.6	5.9	9.5	11.0	12.5
≥ 6	76.2	70.4	88.8	78.5	75.6	75.2

of node through 360°. The probabilities of a certain number of stars being in a FOV using the Poisson distribution and the computer simulation are presented in Table 3.4. From the main purpose of the GLAS mission, which measures ice sheet elevation over Greenland and Antarctica, the distribution of stars in both polar regions (above 60° and below −60° of declination) is more important than any other regions. Therefore the independent computations for polar regions were performed and presented in the table. The number of stars in each polar region is given in the parenthesis. If the distribution of stars were ideally uniform in the star catalog, the star tracker would observe seven or eight catalog stars in each image. However, the non-uniform distribution of stars in the star catalog (and on the celestial sphere) gives many different numbers of stars in each image as shown in Table 3.4. If there are more than six stars in the HD-1003 star tracker FOV, the built-in processor may select only six of them in terms of their brightness or relative positions. If there are one or two stars, the stars still can be identified using the direct match technique (DMT) which will be introduced in Chapter 4. However, the accuracy of the determined attitude is lower than that obtained from more stars. An approximate relation between the number of stars and the attitude determined by a deterministic method is [25] :

$$\sigma_{pd} = \frac{\sigma_{star}}{\sqrt{N_{FOV}}}, \tag{3.13}$$

where σ_{pd} is the accuracy of the pointing direction perpendicular to the detector plane, σ_{star} is the uncertainty of the star position and N_{FOV} is the number of stars in the FOV.

In the simulation, no cases occurred when no star was observed in the FOV. However, eclipses by the Sun or the Moon can produce periods with no star observations. The approximate ranges where the star tracker is adversely affected are approximately a 35° radius from the Sun and a 25° radius from the Moon [11]. For example, the 35° radius from the Sun may cause the maximum eclipse period of about 19 minutes. During the eclipses by the Sun or the Moon, the attitude determination based on the star tracker measurement is not available and then the attitude changes need to be detected by a set of gyros (e.g., IRU) until new star measurements are obtained in the FOV. However, if the time duration in which only gyro measurements are available is too long, the intrinsic bias drift of gyros will cause a significant deviation of the determined attitude from the truth. To reduce the influence of the Sun and the Moon, the ICESAT/GLAS PAD could use Ball CT-602 star trackers whose BDs are tilted in terms of the HD-1003. In the low declination the eclipsing due to the Sun and the Moon would be forecasted and pre-considered, but the low latitude region requires relatively relaxed attitude accuracy. For the ice-sheet

Table 3.5: Specifications of the Hipparcos Star Catalog [1]

Measurement Satellite	Hipparcos Satellite(ESA)
Measurement Period	1989.85-1993.21
Number of entries	118218
Catalogue epoch	J2000
Reference system	ICRS
Date Published	June 1997
Astrometry ($Hp < 9mag$)	
Median precision of positions, J1991.25	0.77/0.64 mas (RA/dec)
Median precision of parallaxes	0.97 mas
Median precision of proper motions	0.88/0.74 mas/yr (RA/dec)
Estimated systematic errors	< 0.1 mas
Photometry ($Hp < 9mag$)	
Median photometric precision	0.0015 mag
Mean number of photometric observations per star	110
Number of entries variable or possibly variable	11597
Number of solved or suspected double/multiple systems	23882

measurements in polar regions, solar and lunar eclipsing will not raise a serious problem because the Sun and the Moon are located in low declination ($-30° < \delta < 30°$). Planets are also positioned on or near the ecliptic plane and their movements are well predicted. Thus, planetary obscuration will be dealt with in a similar manner to eclipses by the Sun and the Moon.

3.3.2 Star Catalog for Real Application

For the PAD, the recently completed *Hipparcos Star Catalog* [1], containing the most accurate astrometric and photometric star data compared with other star catalogs, will be used.* The median precision of position and brightness of the *Hipparcos Star Catalog* are 0.77 milliarcsecond and 0.0015 magnitude respectively. The important features of the *Hipparcos Star Catalog* are given in Table 3.5.

**SKY2000 Master Catalog* (Version 2) was used in practice. The Hipparcos and Tycho catalogs provide high-quality astrometric and photometric data for virtually all SKY2000 stars in Version 2 and later versions. The *Tycho Catalog* is also the output from ESA's Hipparcos mission.

3.3.3 Corrections of Star Measurement

Aberration

Aberration is the apparent shift in the position of a star caused by the motion of the spacecraft. For Earth-orbiting spacecraft, the motion of the Earth around the Sun causes a maximum *aberration* of about 20 arcseconds. The motion of the spacecraft about the Earth at a 600 km altitude with a circular orbit accounts for about 6 arcseconds additional *aberration*. The *aberration* angle, β, is computed from the spacecraft velocity relative to the Sun, $\vec{v}$, by [65],

$$\beta = \frac{|\vec{v}|}{c} \sin\theta, \tag{3.14}$$

where c is the speed of light and θ is the angular separation between $\vec{v}$ and the true star direction. Because we need information for all directions, the vector form of *aberration* equation is necessary. By using the nutation angles, the *aberration* vector, $\vec{\kappa}$, and true obliquity of the ecliptic, the unit vector direction to the star corrected for annual *aberration*, $\hat{S}_A$, is [54]

$$\hat{S}_A = (1 + \hat{S}_T \cdot \vec{\kappa})\hat{S}_T - \kappa, \tag{3.15}$$

where $\hat{S}_T$ is the unit vector to the star rotated into true-of-date coordinates from the unit star vector in mean equatorial coordinates of date. The *aberration* due to the spacecraft motion around the Earth is approximately computed from

$$\hat{S} = (1 - \hat{S}_A \cdot \vec{v}/c)\hat{S}_A + \vec{v}/c, \tag{3.16}$$

where $\hat{S}$ is the unit vector to the apparent place of the star observed by the star sensor in the spacecraft. The *aberration* correction is applied right after the star identification.

Proper Motion

Many stars show continuous changes in position indicating a certain angular velocity. Such angular velocities are known as *proper motions*. The proper motion of an individual star may be as large as several arcseconds per year. Special considerations must be given to the stars which will show significant changes during the mission period due to large proper motions.

Parallax

The star catalog is usually created in the heliocentric inertial coordinate system. Since the Earth is moving around the Sun once a year, the direction of a star as seen from the Earth (and the spacecraft) is changing periodically and half of the changed angle is called *parallax*. For the GLAS mission, the corrections to the *parallax* are not required since the maximum *parallaxes* for the very few closest stars to the solar system are only 0.8 arcsecond and *parallaxes* of most stars are negligible. Furthermore, the attitude determination is based on all the stars in the FOV so that the *parallax* error on one or two stars will not affect the result significantly [25].

Chapter 4

STAR IDENTIFICATION

An essential component of CCD star tracker data processing is the star identification. Star measurement data must be identified using the star information in the mission star catalog to determine exactly which stars the sensor is tracking. Star identification algorithms require appropriate parameter adjustment depending on sensor characteristics, noise environments, and the given star catalog. There are several existing star identification techniques [65]. In the first section of this chapter, we will discuss a pattern matching algorithm (PMA), which matches the angular distances between pairs of observed stars with those of cataloged stars. Since the CCD star tracker enables us to detect multiple stars simultaneously, it seems appropriate to choose the PMA as a star identification method. An advantage of PMA is that this method can be used when no a priori attitude (or star) information is obtainable or the quality of the a priori information is in doubt. The PMA developed for this research requires at least three stars at a measurement time, but the simulation sometimes showed that only one or two stars were observed in a star tracker FOV. The second section of this chapter will discuss the DMT, which identifies every measured star separately in the star catalog. Since the ICESAT/GLAS will stay in the simple nadir pointing attitude mode and will estimate the attitude with one arcsecond accuracy at the measurement time, the predicted attitude would be close to the true attitude. In other words, we have good prediction for star positions at the new measurement time and then the area to be searched for in order to find the matched star should be small. In this way, it is possible to identify most of the measured stars, even when one or two stars are observed by the star tracker. The DMT could be used as the auxiliary method to help the PMA, but it could also be used as stand-alone method if the BD would be known all the time with sufficiently good accuracy either from the attitude prediction or from real time on-board attitude determination.

4.1 Pattern Matching Algorithm

4.1.1 Sectioning of Star Catalog

The star catalog for attitude determination contains at least several thousand stars. Therefore, a search for the matching stars in the star catalog that occur within an $8^\circ \times 8^\circ$ FOV might take an excessive length of time. This also increases the possibility of misidentification since there would be a significant probability of encountering similar distributions of observed stars in the star catalog. A search of the entire catalog will cause more serious

problems in real time attitude determination where fast processing is required. However, if we have a best guess of the star tracker BD available from a previous estimation or from other (coarse) sensors, only a small area in the star catalog around the BD would need to be searched to identify the measured stars. This will greatly reduce the required search time and the probability of misidentification. To support this technique, the celestial sphere must be divided into many cells (or segments) in an orderly pattern so that we can find the matched stars in several cells surrounding the estimated BD. Catalog stars will be preassigned in those cells by their positions in the star catalog.

As a first step to set up the divided cells in the celestial sphere, the locations of the cell centers are given by [59]

$$\begin{aligned} \delta_n &= \frac{\pi}{2} - \cos^{-1}(\xi_n) & n = 0, 1, 2....N \\ \alpha_{nj} &= \frac{2\pi j}{2n+1} & j = 0, 1, 2....2n \end{aligned} \tag{4.1}$$

where δ is declination, α is right ascension, and N determines the total number of cells and the size of each cell. The ξ_n is defined by

$$\xi_n = (-1)^n \cos(\frac{n\pi}{2N+1}) \qquad n = 0, 1, 2....N. \tag{4.2}$$

These equations divide the celestial sphere into $N+1$ declination zones and $(2n+1)$ equally spaced regions in each zone, yielding $(N+1)^2$ cells without overlapping.

If the cell size becomes larger, more stars will be stored in one cell and a smaller number of cells will be made. In contrast, the small cell size will require access to more cells in order to find the matching stars. The choice of cell size (i.e., N) affects the star identification efficiency both in time and in storage. The area of the star tracker FOV must be considered to determine the optimal cell size. If N is 22, each cell covers an area slightly larger than an $8^\circ \times 8^\circ$ celestial area which is the size of the FOV for typical star trackers (e.g., CT-601 and HD-1003). Assuming that the estimated BD of the star tracker is close to the true BD, Figure 4.1 shows that we only need to look at the area of $24^\circ \times 24^\circ$. If the star identification algorithm begins to search from the nearest stars to the estimated BD, the full search of $24^\circ \times 24^\circ$ would not be necessary in most cases.

The total number of cells is 529 for $N = 22$. Except for both polar regions, the cells are all trapezoidal shapes. After dividing the entire sky into 529 cells by the rule given in Equation 4.1 and 4.2, the 4853 stars in the star catalog were assigned into those cells by the star coordinates. Figure 4.2 and 4.3 show the cells near the north pole region and the south pole region, respectively. The number of stars in each cell is indicated within parentheses. The numbering of the cells starts from the north pole and it continues to the south pole. This alternative numbering between north and south hemispheres continues until it arrives at the celestial equator zone which contains 45 equally spaced cells with all the centers located at 2° declination. The maximum number of stars in a cell turns out to be 37, which occurs once. Three cells contain one star in a cell, however, there is no cell that has no stars. As we mentioned earlier in Section 3.3, either cells with excessive number of stars or with too few stars make the star identification troublesome and may degrade the accuracy of the attitude determination. It might be possible to develop more complicated codes to deal with dense and sparse regions with different criteria.

To access the desired cells with the knowledge of the estimated BD (in α and δ), the location of the cell is determined by a pointer, $n^2 + j$, where n and j are obtained from

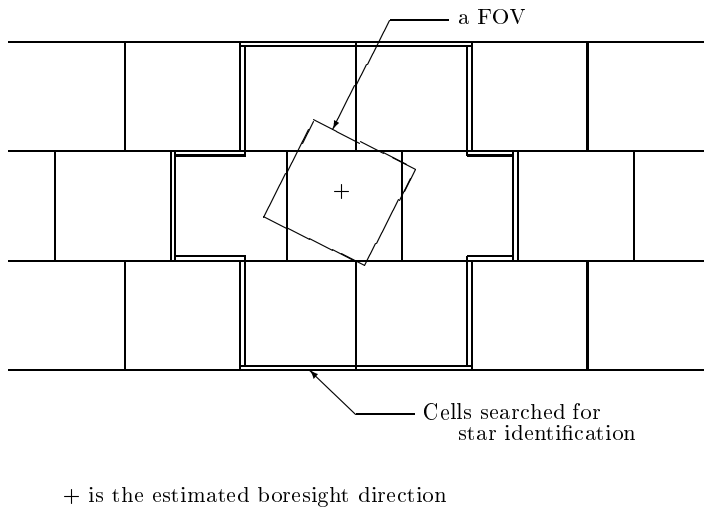

Figure 4.1: A cell pointed by an estimated boresight direction and nearby cells

[59]

$$
\begin{aligned}
n &= 2[(\frac{\pi}{2} - \delta)/\Delta\delta + 0.5] && (\delta > 0^\circ) \\
&= 2N + 1 - 2[(\frac{\pi}{2} - \theta)/\Delta\delta + 0.5] && (\delta < 0^\circ) \qquad (4.3) \\
j &= [\alpha/\Delta\alpha + 0.5], \qquad (4.4)
\end{aligned}
$$

where $\Delta\alpha$ and $\Delta\delta$ are the width of each cell in α and δ. The symbol [ ] indicates the smallest integer greater than (or equal to) the number inside.

To access the surrounding cells, we need to tabulate the numbers of surrounding cells for each cell number. Figure 4.1 shows the surrounding cells around a cell pointed by the BD. Once the cell number is given, whether it is a *pointed* cell by BD or a surrounding cell, the stars residing in the cell will be referred to one by one.

4.1.2 Algorithm

The position angles (ϕ and λ in Equation 3.6 and 3.7) of the observed stars in a FOV of a CCD star tracker are converted to the unit vectors by Equation 3.5. Two base stars can be selected arbitrarily. They might be the two brightest stars in the FOV to reduce the possibility of misidentification. The cosine of the angle, $D_m^{1,2}$, between a pair of measured stars is computed by

$$D_m^{1,2} = \hat{S}_1 \cdot \hat{S}_2, \qquad (4.5)$$

where $\hat{S}_1$ and $\hat{S}_2$ are the unit vectors of the base stars expressed in the SCF. From a priori attitude knowledge, the cell pointed by the BD and the surrounding cells are known at the measurement time. The catalog stars in those cells are considered as *candidate stars* for identification. With the assumption that the estimate of the BD is close to the true

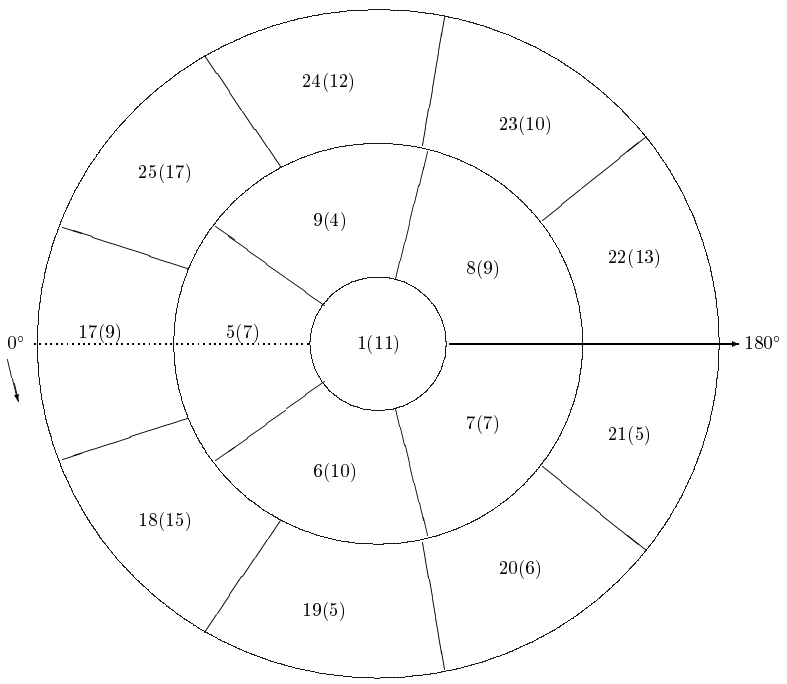

Figure 4.2: Catalog cell pattern near the north pole. The number of stars in each cell is given inside parenthesis.

BD, the *candidate stars* are paired by the distance from the estimated BD. The cosine of the angle between two paired catalog stars, i and j, is

$$D_c^{i,j} = \hat{S}_i \cdot \hat{S}_j, \tag{4.6}$$

where $\hat{S}_i$ and $\hat{S}_j$ are the unit vectors, defined in Equation 3.2, expressed in the CRF. Thus, the match is considered as found if the condition

$$|D_c^{i,j} - D_m^{1,2}| \leq \varepsilon \tag{4.7}$$

is satisfied, where ε is an error window depending on both the star tracker measurement error and the star catalog position uncertainty. If ε is too large, the possibility of a misidentification increases. If it is too small, a misidentification is unlikely, but the number of identified stars are apt to decrease.

It is reasonable to say that the selected catalog stars, $\hat{S}_i$ and $\hat{S}_j$, likely match the measured pair of stars, $\hat{S}_1$ and $\hat{S}_2$, when Equation 4.7 is satisfied. To resolve an inevitable 180° ambiguity stemming from the angular distance comparison, the magnitude test is performed. This is processed in two steps. First, the two catalog stars i and j must have a magnitude difference greater than the magnitude error bound, μ. The μ is determined by combining the star tracker magnitude error and the catalog magnitude uncertainty. Second, the magnitude of the catalog star i must be close to that of the measured star 1

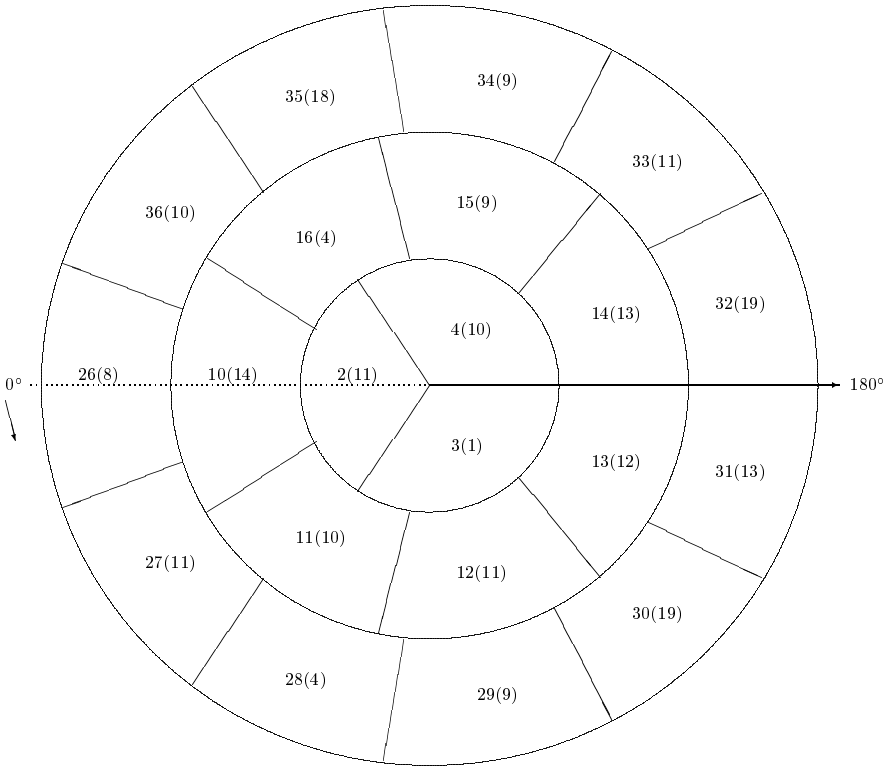

Figure 4.3: Catalog cell pattern near the south pole. The number of stars in each cell is given inside parenthesis.

(or 2) within μ, while being different from the magnitude of catalog star 2 (or 1) more than μ. If these conditions are satisfied, the base stars, 1 and 2, are temporarily considered to be identified.

Failure to resolve 180° ambiguity by the magnitude test will occur in two situations. First, the magnitudes of catalog stars may be unmatched with those of the measured stars in any combination. In this case, the catalog star pair, which satisfied Equation 4.7, are no longer considered as possible matches for the measured star pair. The catalog star pair are discarded and other pairs of *candidate stars* are examined sequentially. Second, when the brightness of the two catalog stars (or two measured stars) are too close, their separation with the parameter μ may not be obtainable. In this situation, the third identified star is required to solve the 180° ambiguity problem of the base stars. Even though the base stars pass the magnitude test, the third identified star is still necessary because there is relatively high probability of finding an invalid star pair match produced by too many catalog star combinations, the unregistered (on star catalog) background stars in the true sky, nearby space debris and/or ghost images [67] of the CCD star tracker. For this reason, the star identification is not initiated when only two stars (or less) are in a frame of the star tracker, and that frame is simply discarded.

The third star is searched for in the remaining *candidate stars*, whether the 180°

ambiguity of base stars are cleared or not, until a star satisfying the following conditions is found :

$$\begin{aligned} |D_c^{i,k} - D_m^{1,3}| &\leq \varepsilon \\ |D_c^{j,k} - D_m^{2,3}| &\leq \varepsilon, \end{aligned} \tag{4.8}$$

where k and 3 are the indices for the third star in the catalog and in the measurement, respectively. If the magnitude test for base stars is successful with the matches of $(i,\ 1)$ and $(j,\ 2)$, Equation 4.8 is the condition which must be satisfied for the *candidate star* to be the third identified star. In contrast, if there remains a 180° ambiguity problem in the base stars, another chance exists to match the third star by exchanging the order of the base stars using the conditions :

$$\begin{aligned} |D_c^{i,k} - D_m^{2,3}| &\leq \varepsilon \\ |D_c^{j,k} - D_m^{1,3}| &\leq \varepsilon. \end{aligned} \tag{4.9}$$

If the third star satisfies Equation 4.8 or Equation 4.9 and the measured magnitude of the third star is within the error bound of the corresponding catalog magnitude, all three stars are presumed to be identified. After the third star has been identified, the fourth star is matched in a similar way that was used for the third star. This process will be continued until all the measured stars (up to five or six stars) are checked with the *candidate stars*. If an observed star is not matched with any catalog star in this procedure, it is considered to be a *false* measurement and it is ignored. When only three stars are identified in a FOV of the CCD star tracker, there remains a chance of misidentification which will be discussed in the next section. If four or more stars are identified, the probability of misidentification is extremely small (negligible) primarily because the stars are searched in a limited number of cells with an orderly process and the estimated BD will be very close to the true BD.

The values for ε and μ are critical for the star identification. Those values can be initially determined by the noise characteristics of the star tracker measurements and the star catalog uncertainty, and must be adjusted in the real data process after launch. The outline of the star identification algorithm developed in this section is illustrated in Figure 4.4.

4.1.3 Misidentification

Using the PMA, the measured stars can be absolutely identified or *unidentified*. For the latter case, the angular velocity detected by the gyros will enable prediction of the spacecraft attitude until identified star data are available. When only three stars are identified, there is a possibility of misidentification if they satisfy

$$D_m^{2,3} \cong D_m^{1,3}. \tag{4.10}$$

This is the condition that three identified stars form an isosceles triangle with the third star on or near the vertex in the symmetric line, as illustrated in Figure 4.5. When two base stars are located at the positions 1 and 2 and the third star is located at position 3, there is little chance of a misidentification. However, the misidentification likely occurs when the third star is located on or near the symmetry line between the base stars. Then the three stars (1,2 and 3) form an isosceles triangle. If the distinctive magnitudes of

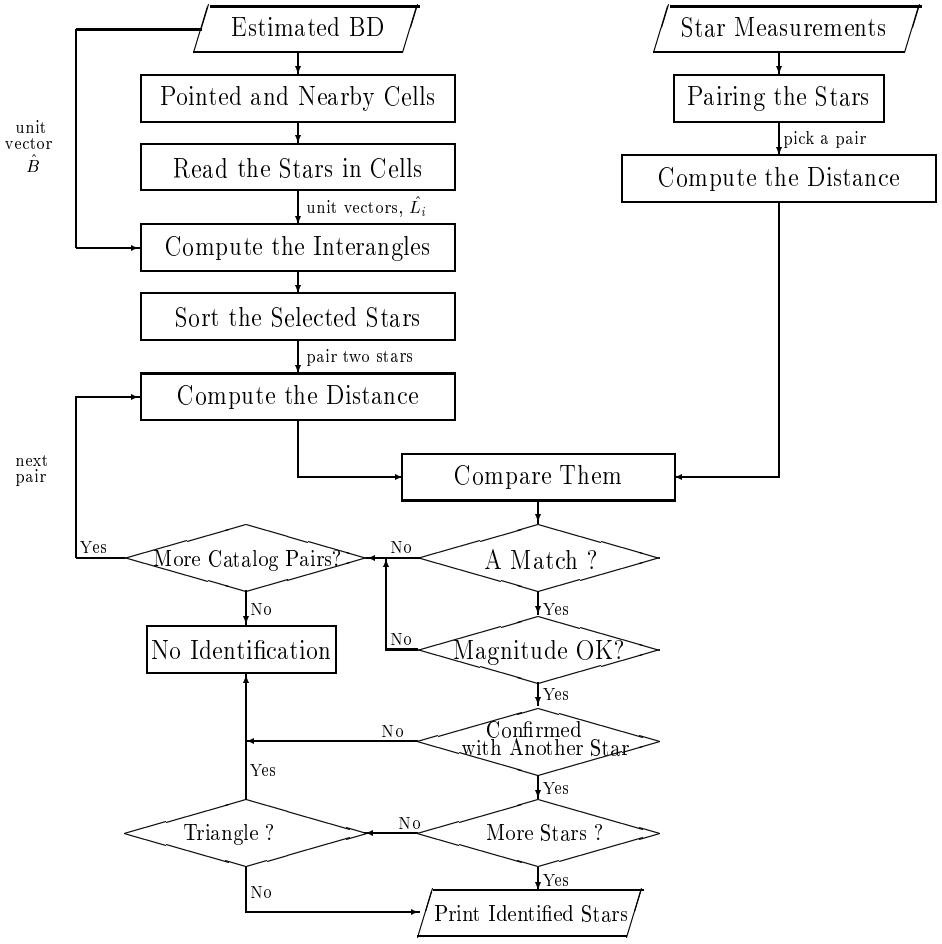

Figure 4.4: Outline of a star identification algorithm

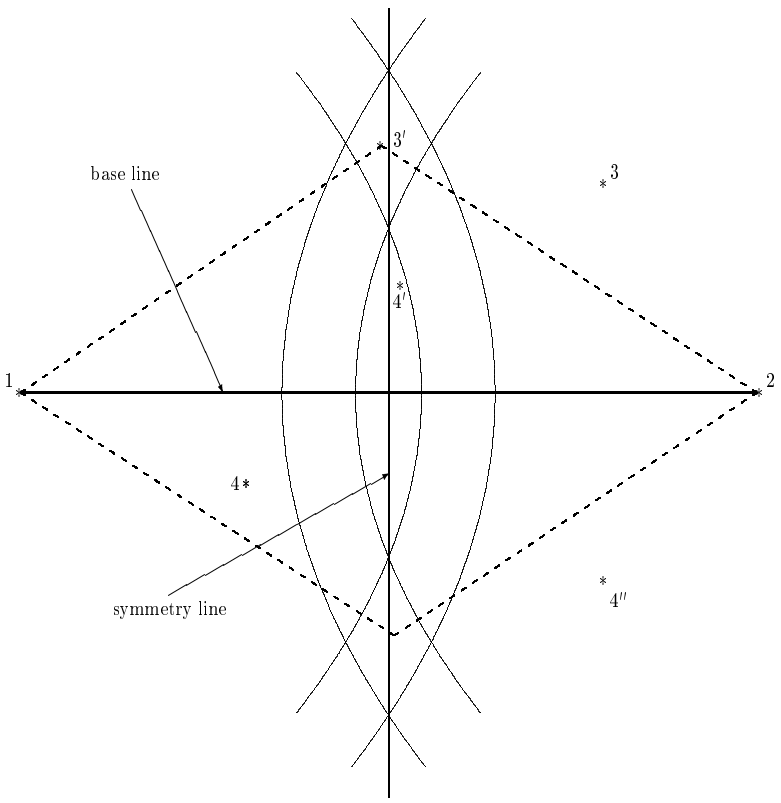

Figure 4.5: Example of a star distribution in a CCD star tracker frame. An isosceles triangle is drawn by base stars (1 and 2) and a star at $3'$ (or $4'$).

the base stars are known by the magnitude test, the third star located at or near the symmetry line provides more confidence on the correct identification of the base stars. However, as long as the 180° ambiguity of the base stars is not resolved and if the third star is located at or near the symmetry line, insufficient information exists to distinguish the base stars. That measurement frame is simply discarded and rendered as *unidentified* at the expense of the loss of the possible correct matches. Since it is not likely to have two (for example, $3'$ and $4'$ in Figure 4.5) or more stars located on or near the symmetry line, the case of only three identified stars would need to be checked for the possible source of the misidentification. Therefore, procedures to detect the isosceles triangle with a 180° ambiguity must be added to the star identification algorithm.

In addition to the isosceles triangle shape, there could be other special geometric configurations made by observed stars. For example, if there is a background star in position $4''$ (symmetric about the base line to the third star in position 3), it may be misidentified as a star 3 regardless that the star ($4''$) is a registered star in the star catalog or a simple background star. We can imagine other special geometries formed by three, four or five stars which require more sophisticated star identification algorithms to avoid misidentification.

There are other sources of misidentification that originate from non-geometrical rea-

sons. One example is space debris (or other satellites) near a star tracker BD. Since the star tracker does not discern these sources from a real star, debris may cause misidentification. (Debris actually caused a more serious problem in the star tracker performance of the X-ray Timing Explorer (XTE) spacecraft [15]). Ghost images of the CT-601 have been reported as an identification error source [67]. The star identification algorithm must be sufficiently smart to consider ghost images as background stars that are unregistered in the mission star catalog.

It is possible in the attitude estimation procedure to detect the measurement frame which has misidentified stars. The abnormal discontinuity of quaternions (or the computed angular velocity) obtained by Single Frame Attitude Determination (SFAD) methods (Chapter 5) could be interpreted as an outbreak of the misidentification. Even though we suppose that the PMA could include the detection of various misidentification sources, the complete escape from the misidentification would not be easy.

4.1.4 Simulation Results

The star tracker measurements were simulated for four circular orbits with 94° inclination using the algorithm developed in Section 3.1. The respective initial positions are 0°, 45°, 90° and 135° right ascensions at the equator. The time interval between successive FOVs is 0.1 second. The measurement noises were computed based on the 1σ values given in Section 3.1.3 for generating realistic simulation data.

The PMA was applied to the simulated star measurement data and the results are summarized in Table 4.1. In the simulation, the possible maximum number of FOVs for each orbit is 57901 corresponding to a 10Hz measurement rate for one GLAS orbital period. Since the minimum number of stars necessary for the identification process is three, the number of frames containing at least three stars are shown in the second column of Table 4.1. The Π in the third column is a parameter representing the range in which the third star is considered in a position to form an isosceles triangle with base stars. It is computed by

$$\Pi = |D_m^{1,3} - D_m^{2,3}| \tag{4.11}$$

which means the distance difference between two sides of triangles other than the base line. In other words, if the third star, 3, is located at a position to make the right side of Equation 4.11 less than Π, the three identified stars are considered to form an isosceles triangle. These stars are regarded as possible misidentification cases and are abandoned. The identification processing is resumed in order to find another group of stars which do not construct the isosceles triangle defined by Equation 4.11.

Table 4.1 shows that all the star tracker measurement frames are reported as identified (indicated by 100%) if the isosceles triangle formed by the three stars is simply regarded as a correct identification ($\Pi = 0$). However, the misidentification occurred in some frames as indicated in the last column of the Table 4.1, except for the case with 45° initial right ascension, α. For example, 0° initial α contains 167 misidentified frames, which is 0.3% of the reported identified frames. Computed results show that when the angle Π is increased, the occurrence of the misidentification is decreased and finally disappears. There are more reductions in the total number of identified frames (see the seventh column in Table 4.1) than the number of misidentified ones (the eighth column). This clearly indicates that the elimination of the misidentification source results in the removal of some correctly identified frames. Table 4.1 also shows that the number of frames with five identified

Table 4.1: Star identification simulation results using the pattern matching algorithm. One orbital period of simulated data were processed.

RA (α)	FOVs ($\geq$3)	Π (radian)	Number of Identified Frames				Mis. ID frames(%)
			3 stars	4 stars	5 stars	total(%)	
0°	54981	0.0	4418	6074	44487	54979(100)	167(0.3)
		2.0×10^{-4}	4399	6074	44487	54960(99.96)	167(0.3)
		1.0×10^{-3}	4296	6074	44487	54857(99.77)	167(0.3)
		5.0×10^{-3}	3477	6074	44654	54205(98.59)	0(0)
45°	53619	0.0	2729	4186	46704	53619(100)	0(0)
		2.0×10^{-4}	2717	4186	46704	53607(99.98)	0(0)
		1.0×10^{-3}	2655	4186	46704	53545(99.86)	0(0)
		5.0×10^{-3}	2577	4186	46704	53467(99.72)	0(0)
90°	56991	0.0	2450	5008	49533	56991(100)	72(0.1)
		2.0×10^{-4}	2441	5008	49537	56986(99.99)	68(0.1)
		1.0×10^{-3}	2401	5008	49552	56961(99.95)	53(0.1)
		5.0×10^{-3}	2190	5008	49605	56803(99.67)	0(0)
135°	55881	0.0	1666	3821	50394	55881(100)	115(0.2)
		2.0×10^{-4}	1662	3821	50394	55877(99.99)	115(0.2)
		1.0×10^{-3}	1642	3821	50394	55857(99.96)	115(0.2)
		5.0×10^{-3}	1299	3821	50468	55588(99.48)	41(0.1)
		1.0×10^{-2}	1258	3821	50509	55588(99.48)	0(0)

stars (the sixth column) increases as Π increases. This means that the misidentification in some frames hinders the determination of correct star matches. The lowest probability of successfully identifying stars without misidentification was 98.59% in the simulation. Even though this result is undoubtedly promising, further star identification tests (and necessary improvements) should be carried out with more background stars in which the magnitude range covers up to eighth or ninth.

4.2 Direct Match Technique (DMT)

4.2.1 Algorithm

The requirement of more than two stars as well as the relatively high possibility of the misidentification when only three stars are present in the star tracker FOV were pointed out as shortcomings of the PMA. The DMT enables us to identify the stars when the FOV contains only one or two stars. Once the GLAS attitude determination is initialized and determines attitude in the required accuracy, the DMT can identify almost all stars observed by the FOV. The prediction of attitude can be achieved by applying the kinematic equation of attitude quaternions, Equation 2.11. Alternatively, the quaternions obtained by the real time on-board attitude determination can be used. The accuracy requirement for real time is 10-20 arcseconds(1σ). Figure 4.6 illustrates the relations of the coordinate frames in the DMT.

The star tracker observes up to six stars at a measurement time. If either the predicted

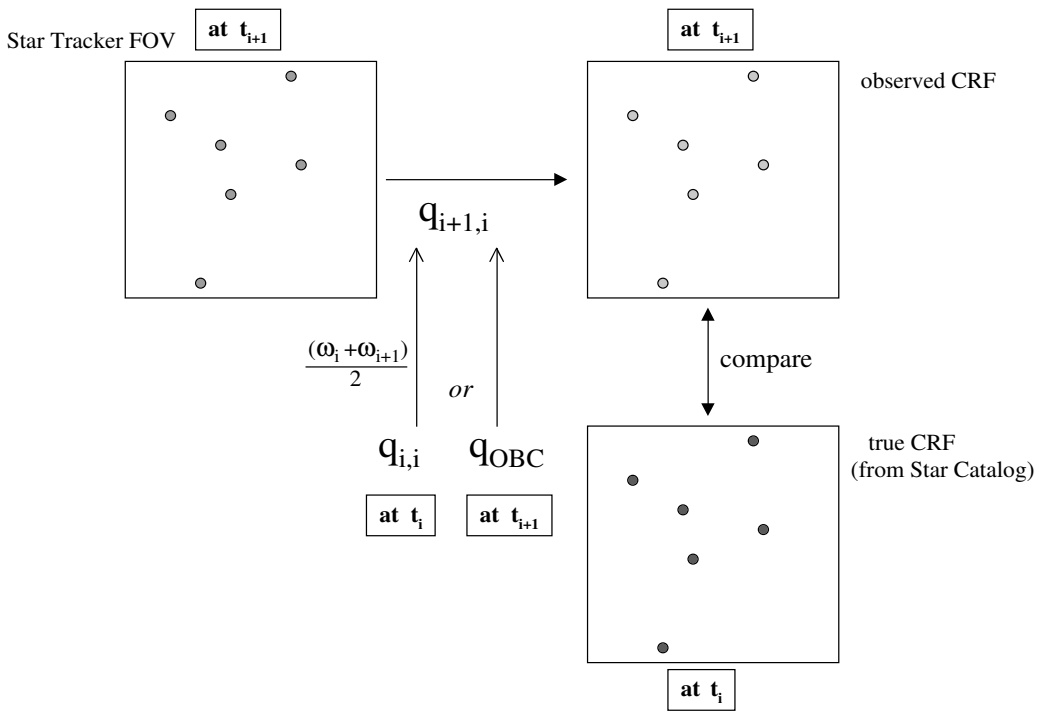

Figure 4.6: Coordinate systems in the direct match technique

or the real time attitude is known, the star positions will be transformed from the SCF to the CRF (the observed CRF in Figure 4.6). If either the predicted or the real time attitude is sufficiently close to the true attitude, the small circular area centered by the observed star will be searched in the star catalog (Figure 4.7). By defining ϵ as the error window radius of the circular area, the catalog star satisfying the equation

$$d(\hat{O}, \hat{S}) < \epsilon \tag{4.12}$$

will be considered as the matched star, where $d(\hat{O}, \hat{S})$ is the angular distance between $\hat{O}$, the observation unit vector in the observed CRF, and $\hat{S}$, the catalog star unit vector in the true CRF. The value for ϵ is determined by the accuracy of the predicted or real time attitude.

It is easy to see that the procedure described here would provide unique star identification if the density of star population is considered. Since the HD-1003 star tracker will observe stars brighter than magnitude 6, the number of stars in the corresponding star catalog is generally five or six thousand. In this case, the stellar density of the catalog is roughly less than 1 star per square degree. By selecting several tens of arcseconds as the error window radius, ϵ, in Equation 4.12, we are able to identify almost all stars uniquely. If multiple stars are found in the error window radius, additional work has to be done with the comparison of either star magnitudes or the error sizes, $d(\hat{O}, \hat{S})$, in order to achieve the unique identification. If no star is found within the radius ϵ, the observed star might be the non-star object or the predicted (or real time) attitude might have large error.

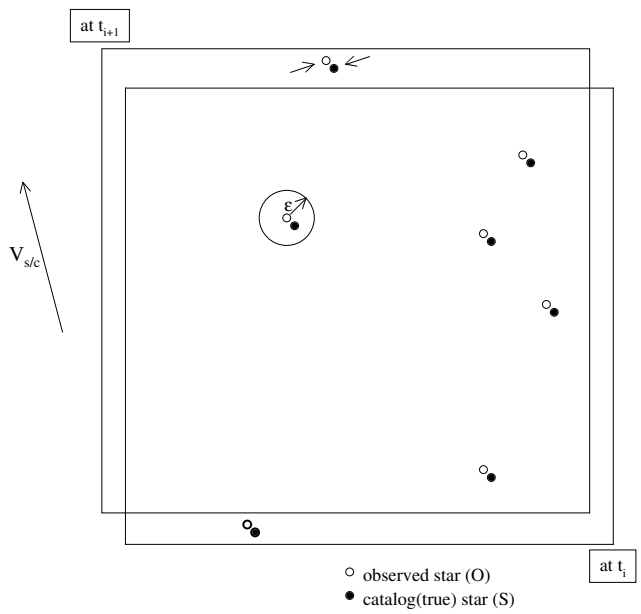

Figure 4.7: Catalog stars close to measured stars

4.2.2 Catalog Star Search

In the PMA, the area to search for the matched star should be larger than the star tracker FOV, $8° \times 8°$. It was required to divide the celestial sphere into many cells in order to look at the restricted region in stead of the whole sky. (see Section 4.1.1). In the DMT, a star can be identified by looking at the small circular area whose radius is usually tens of arcseconds with the observed star at the center. The method sectioning the star catalog into many cells could be applied to the DMT, but the size of each cell must be much smaller than that for the PMA in order to efficiently search the area of the several tens of arcseconds ϵ radius (Equation 4.12). This would require excessive work to create and organize more than several thousand cells and access to each cell in the search process would be problematic when we consider the limited computation time. Therefore, the DMT developed for the GLAS PAD applies a new approach that does not use the sectioning of the star catalog described in Section 4.1.1. As the first step of the new approach, the catalog stars whose right ascensions, α, are sufficiently close to the observed stars will be selected as candidate stars for identification. Since the star tracker is able to track the stars, the most probable matched star is the one that was identified at the previous measurement time. By looking at the catalog stars in both the increasing and decreasing direction of catalog numbers, from previously identified number, k, it is very likely to find catalog stars whose right ascensions, α, are in several tens of arcseconds from that of the observed star, unless the star is new to the star tracker FOV. Therefore, the search area can be restricted to :

$$\alpha_0 - \epsilon < \alpha < \alpha_0 + \epsilon, \tag{4.13}$$

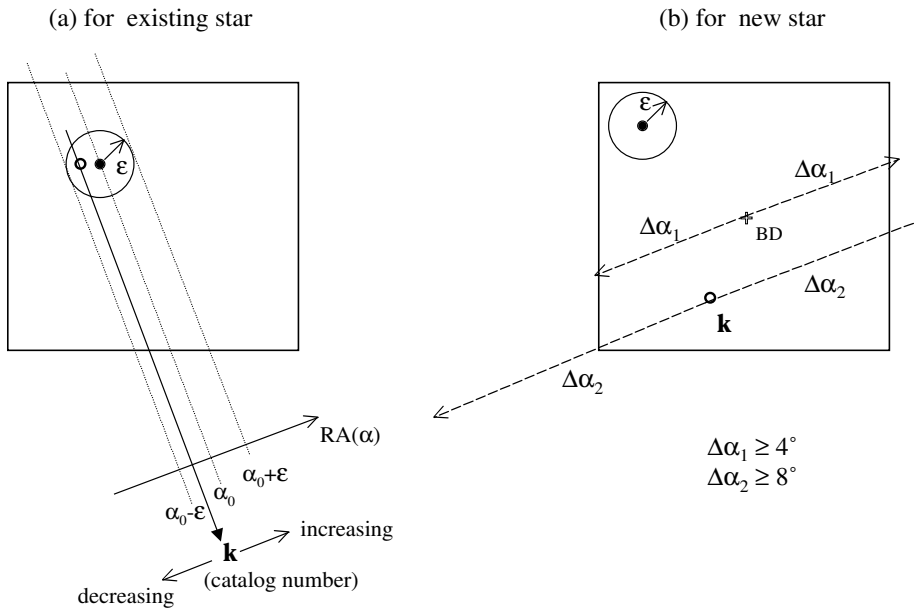

Figure 4.8: Search for matched star in star catalog

where α_0 is the observed star α (see Figure 4.8(a)) and ϵ is the error window radius already introduced in Equation 4.12.

For a star newly moving into the FOV (see the bottom of Figure 4.7), the ϵ boundary doesn't help find the match and we need to extend the search area. We refer to one of the previously identified star catalog numbers and need to search $\approx 8°$ right ascension range both in increasing and decreasing k directions (Figure 4.8(b)). To reduce the search time, we may further restrict the search area within $\approx \pm 4°$ right ascension range from the predicted BD. Equation 4.12 is applied to the stars residing in the selected α range in order to choose the correct match for the observed star.

The search method described here performed well in the simulation. However, due to the nature of the longitude and latitude system for the celestial sphere, a large number of stars (sometimes all the stars in the star catalog) had to be looked at when the star tracker observed the vicinity of the polar regions. This search method has been improved by dividing the celestial sphere according to *latitude zones* as shown in Figure 4.9.

This zoning of the star catalog is a reduced version of sectioning described in Section 4.1.1. To avoid looking up to nearby zones, each zone is overlapped with the neighboring zones. This could enable us to search only a rectangular area represented by thick lines in Figure 4.9(b) instead of the area indicated in 4.9(a).

4.2.3 Simulation Results

In the simulation of the DMT, we achieved almost 100% successful star identifications without any misidentification. Table 4.2 shows the results obtained by the DMT when the same simulation data as for the PMA were used.

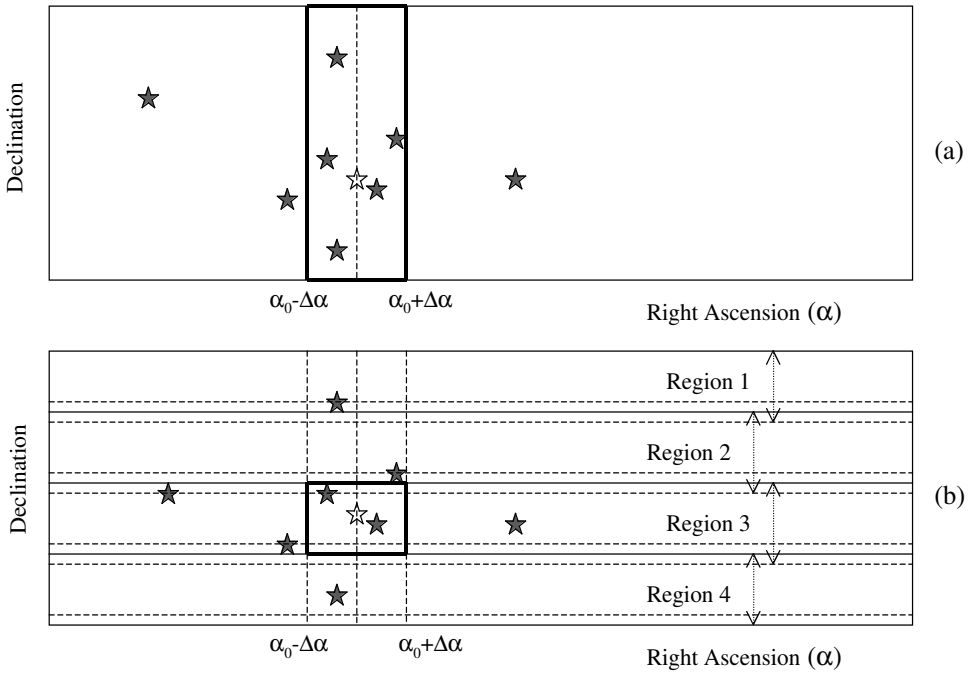

Figure 4.9: Searching area for star identification. Latitude zones more than 4 are expected.

Table 4.2: Star identification simulation results using the direct match technique. One orbital period of simulated data were processed.

RA (α)	Total Number of Observed Stars	Number of Identified Stars	Number of Misidentified Stars
0°	265738	265735 (99.999%)	0
45°	265003	265003 (100.00%)	0
90°	276872	276867 (99.998%)	0
135°	275330	275232 (99.964%)	0

Chapter 5

ATTITUDE DETERMINATION

5.1 Single Frame Attitude Determination

In this section, several algorithms will be introduced to determine the spacecraft attitude from the observed unit vectors. Since these algorithms determine attitude from measurement data obtained by a frame of a CCD star tracker, they will be called Single Frame Attitude Determination (SFAD) methods in this document.

Because the loss function $J(A)$ in *Wahba Problem* (Equation 2.20) can be scaled without affecting the optimum attitude matrix, A_{opt}, it is possible to normalize the weights such as

$$\sum_{i=1}^{n} a_i = 1 \tag{5.1}$$

with no loss of generality. Then the loss function can be easily manipulated to

$$\begin{aligned} J(A) &= 1 - \sum_{i=1}^{n} a_i \hat{W}_i^T A \hat{V}_i \\ &= 1 - g(A). \end{aligned} \tag{5.2}$$

The loss function $J(A)$ will have a minimum value when the gain function $g(A)$ has a maximum value. The $g(A)$ is given by

$$\begin{aligned} g(A) &= \sum_{i=1}^{n} a_i \hat{W}_i^T A \hat{V}_i \\ &= \sum_{i=1}^{n} a_i tr[A \hat{V}_i \hat{W}_i^T] \\ &= tr[AB^T], \end{aligned} \tag{5.3}$$

where tr means trace of a matrix and the *B-matrix* or *Attitude Profile Matrix*, B, is,

$$B = \sum_{i=1}^{n} a_i \hat{W}_i \hat{V}_i^T. \tag{5.4}$$

The *B-matrix* is very important since it contains all the information from the measurement and reference vectors. The construction of this matrix is the beginning of every solution

of the *Wahba Problem* in this section. Finally, the original *Wahba Problem* proposed in Equation 2.20 turns into the minimization problem of

$$J(A) = 1 - tr(AB^T) \tag{5.5}$$

or the maximization problem of

$$J'(A) = tr(AB^T). \tag{5.6}$$

There exist many SFAD algorithms. The simple description of these methods are given in the following sections, while the precise derivations of these can be found in the references.

QUEST

The QUEST algorithm is an improved version of the *q-method* developed by Davenport [65]. He has shown that the minimization of the loss function $J(A)$ can be transformed into an eigenvalue problem of a 4×4 matrix, K :

$$K = \begin{bmatrix} S - \sigma I & \vec{Z} \\ \vec{Z}^T & \sigma \end{bmatrix}. \tag{5.7}$$

where

$$\begin{aligned} S &= B^T + B \\ \vec{Z} &= \sum_{i=1}^{n} a_i \hat{W}_i \times \hat{V}_i \\ \sigma &= trB. \end{aligned} \tag{5.8}$$

It was shown that components of the eigenvector corresponding to the biggest eigenvalue in K matrix are the attitude quaternions. Shuster's QUEST algorithm [49] is a variation of the *q-method* in the last step of *q-method*. It avoids the necessity for solving the eigenvalue problem and saves computation time by using a simple Newton-Rhapson method. Through matrix manipulations, Shuster finally derived a fourth order characteristic equation for λ as

$$\lambda^4 - \alpha\lambda^2 - \beta\lambda + \gamma = 0, \tag{5.9}$$

where α, β and γ are defined in terms of S, $\vec{Z}$ and σ in Equation 5.8. Since λ_{max} is known to be very close to unity when the normalized weight is used, Equation 5.9 is solved for λ with the Newton-Raphson method using $\lambda = 1$ as an initial value. This is the point where the QUEST algorithm is preferable to the original *q-method* from a practical point of view. In the simulation performed for this study, only one or two iterations were required to solve Equation 5.9. Once λ_{max} is known, the corresponding optimal quaternions can be quickly computed from

$$q = \frac{1}{\sqrt{s + \|\vec{X}\|^2}} \begin{Bmatrix} \vec{X} \\ s \end{Bmatrix}, \tag{5.10}$$

where s and $\vec{X}$ are also obtained by combining the parameters in Equation 5.8.

QUEST Covariance Matrix

A rigorous derivation of the error covariance matrix is given by Markley [28] for the unit vector measurement. The general assumptions for the errors in the unit vector measurement are as follows :

- Because the vectors $\hat{V}_i$ and $\hat{W}_i$ are constrained to be unit vectors, the error in any one of them must, to the first order, lie in the plane perpendicular to that vector.
- The error vector has an axially symmetric distribution about the respective unit vector.
- Since the attitude estimation error must be independent of the true attitude, the statistical value for the size of the error in the attitude quaternions is determined only by the star tracker measurement and the star catalog errors. In other words, the amount of attitude error must be the same, regardless of the spacecraft orientation, if we use exactly the same algorithm and the same measurement and catalog errors for the attitude determination. Therefore, a special assumption can be made such as
$$\hat{W}_i = \hat{V}_i, \tag{5.11}$$
which means that the inertial and observation vectors are identical. Most of the time, Equation 5.11 is not true. But this assumption does not affect the values of error covariance matrix (or $\delta\vec{q}$).

Thus, the QUEST covariance matrix is derived as [49]

$$P_{\vec{q}\vec{q}} = \frac{1}{4}\sigma_{tot}^2[I_{3\times3} - \sum_{i=1}^{n} a_i\vec{W}_i\vec{W}_i^T]^{-1}, \tag{5.12}$$

where a_i is a weight of the measurement shown in the *Wahba problem*. The total measurement error in a frame of the CCD star tracker, σ_{tot}, is

$$(\sigma_{tot}^2)^{-1} = \sum_{i=1}^{n}(\sigma_i^2)^{-1}, \tag{5.13}$$

where σ_i is the sum of the measurement and the catalog errors and is related to the weights of each measurement by

$$\sigma_i = \sigma_{tot}/\sqrt{a_i}. \tag{5.14}$$

Applying the small angle approximation of quaternions in Equation 2.4, the covariance matrix for attitude error angles becomes

$$P_{\theta\theta} = 4\ P_{\vec{q}\vec{q}}. \tag{5.15}$$

The square roots of the diagonal components of $P_{\theta\theta}$ correspond to yaw, roll and pitch (1σ) errors, respectively.

Singular Value Decomposition(SVD)

It is well known that any matrix, B, can be decomposed as follows :

$$B = USV^T, \tag{5.16}$$

where U and V are 3×3 orthogonal matrices and

$$S = diag(s_1, s_2, s_3) \tag{5.17}$$

with

$$s_1 \geq s_2 \geq s_3 \geq 0. \tag{5.18}$$

The Equation 5.17 means that S is a diagonal matrix with diagonal elements s_1, s_2 and s_3. They are called singular values of B and Equation 5.16 is called Singular Value Decomposition (SVD) [58].

Assuming that the matrix B in Equation 5.16 is the same as the *B-matrix* defined in Equation 5.4, Markley derived the attitude matrix, A, as [28]

$$A = U[diag(1, 1, d)]V^T, \tag{5.19}$$

where

$$d \equiv (det\ U)(det\ V) = \pm 1. \tag{5.20}$$

Polar Decomposition (PD)

A very different approach to the *Wahba Problem* can be given as follows [8] : The Euclidean norm of the general real matrix Q is defined by

$$\|Q\|^2 \equiv \sum Q_{ij}^2 = tr(QQ^T), \tag{5.21}$$

where $\|Q\|$ is the matrix norm of Q and the sum is over all the matrix elements. From the assumed orthogonality of A and the properties of the trace, the matrix norm of the difference of two matrices, A and B, is

$$\|A - B\|^2 = tr[(A - B)(A - B)^T] = 3 - 2tr(AB^T) + \|B\|^2. \tag{5.22}$$

Because the orthogonal matrix A that maximizes $tr(AB^T)$ minimizes this norm, the *Wahba problem* is also equivalent to the problem of finding the proper orthogonal matrix A that is closest to B in the Euclidean norm.

The Polar Decomposition says that every real square matrix can be factored into [58]

$$Q = PR, \tag{5.23}$$

where the P matrix is orthogonal and the R matrix is symmetric positive semidefinite. If Q is invertible, then R is positive definite. This P is the closest orthogonal matrix to the matrix Q. Assuming error-free observations W_i $(i = 1, 2, ..n)$, Equation 5.4 becomes [8]

$$B = \sum_{i=1}^{n} a_i \hat{W}_i \hat{V}_i^T = \sum_{i=1}^{n} a_i A \hat{V}_i \hat{V}_i^T = A \sum_{i=1}^{n} a_i \hat{V}_i \hat{V}_i^T = AR, \tag{5.24}$$

where R is a symmetric matrix. Therefore the attitude matrix A can be found by

$$A = BR^{-1}. \tag{5.25}$$

A is not necessarily orthogonal because of the error-free assumption for attitude measurement.

Iteration Method (ITER) *and Improved Polar Decomposition* (IPD)

From the fact that the attitude matrix A is the closest orthogonal matrix to the *B-matrix*, the iterative orthogonalization algorithm [8]

$$\begin{aligned} A_0 &= B \\ A_{i+1} &= \frac{1}{2}(A_i^{-T} + A_i) \end{aligned} \tag{5.26}$$

can be applied until A_{i+1} converges to the solution of the *Wahba problem.*

The PD method can be improved by applying the orthogonalization algorithm in Equation 5.26 [8], then

$$A = \frac{1}{2}(B^{-T}R + BR^{-1}). \tag{5.27}$$

This is called the Improved Polar Decomposition.

Fast Optimal Attitude Method (FOAM)

Combining the singular values of the *B-matrix* (see Equation 5.17), the optimal attitude matrix can be rewritten as [29]

$$A = [(\kappa + \|B\|^2)B + \lambda \; adj\,(B^T) - BB^TB] \;/\; \zeta, \tag{5.28}$$

where the scalar coefficients κ, λ and ζ are determined using the singular values of the *B-matrix.* To derive A, the Wahba's loss function is set to

$$J(A) = \lambda_0 - tr(AB^T), \tag{5.29}$$

where a_i is not normalized,

$$\lambda_0 \equiv \sum_{i=1}^{n} a_i \neq 1. \tag{5.30}$$

The benefit of the FOAM over the SVD method is that the coefficients κ, λ and ζ can also be computed without using the SVD. By matrix algebra, κ and ζ could be represented as functions of λ and B, where λ is the root of the following equation :

$$0 = p(\lambda) \equiv (\lambda^2 - \|B\|^2)^2 - 8\;\lambda det\,B - 4\;\|adjB\|^2. \tag{5.31}$$

The largest root of $p(\lambda)$ minimizes the loss function $J(A)$. Since λ_0 is close to λ, we have a very good choice of the initial λ and need to iterate only a few times.

Modified Fast Optimal Attitude Method (MFOAM)

All methods except QUEST (and the *q-method*) discussed up to now in this section produce rotation matrices rather than quaternions. The quaternions can be extracted from the attitude matrix using Equation D.5.

The MFOAM [30] is the variation of FOAM in order to compute quaternions directly. Inserting λ_0 into Equation 5.28, the approximately orthogonal matrix, A_0, is obtained by

$$A_0 = M/\zeta(\lambda_0, B), \tag{5.32}$$

where

$$M = \frac{1}{2}(\lambda_0^2 + \|B\|^2)B + \lambda_0 \; adj \, B^T - BB^T B. \tag{5.33}$$

Then, the attitude matrix can be orthogonalized while extracting normalized quaternions q from A_0. The extracting equations are a modification of Equation D.5.

5.2 Extended Kalman Filter

5.2.1 Basic Algorithm

The estimation algorithm for the EKF is based on Lefferts et al.[23] and Fisher et al.[16]. Instead of the direct estimation of the four element quaternions, q, the angle error vector, $\delta\vec{\theta}$:

$$\delta\vec{\theta} = \begin{bmatrix} \delta\theta_x \\ \delta\theta_y \\ \delta\theta_z \end{bmatrix} = 2 \begin{bmatrix} \delta q_1 \\ \delta q_2 \\ \delta q_3 \end{bmatrix} \tag{5.34}$$

is estimated with the gyro bias error vector which is defined by :

$$\Delta\vec{b} \equiv \vec{b}_{true} - \hat{b}, \tag{5.35}$$

where $\vec{b}_{true}$ is the true gyro biases and $\hat{b}$ is the estimated gyro biases. $\delta q_1, \delta q_2$ and δq_3 are the vector components of small angle (or error) quaternions. The scalar component of error quaternions becomes 1, to the first order, when a small angle rotation is applied to the normal quaternions. In consequence, the dynamic model for the angle error vector is given as :

$$\frac{d}{dt}\delta\vec{\theta}(t) = [\vec{\omega}(t)]\delta\vec{\theta}(t) + \Delta\vec{b} + \vec{\eta}_1 \tag{5.36}$$

$$\frac{d}{dt}\Delta\vec{b}(t) = \vec{\eta}_2(t). \tag{5.37}$$

where $[\vec{\omega}(t)]$ is an antisymmetric matrix which is the matrix representation of the vector product :

$$[\vec{a}]\vec{b} = -\vec{a} \times \vec{b}. \tag{5.38}$$

Now, the conventional linear vector-matrix differential equation is specified by

$$\frac{d(\delta\vec{x})}{dt} = F(t)\delta\vec{x} + G(t)\vec{\eta}(t), \tag{5.39}$$

where

$$F(t) = \begin{bmatrix} [\vec{\omega}_{k-1|k-1}] & I_{3\times3} \\ 0_{3\times3} & 0_{3\times3} \end{bmatrix} \tag{5.40}$$

$$G(t) = \begin{bmatrix} I_{3\times3} & 0_{3\times3} \\ 0_{3\times3} & I_{3\times3} \end{bmatrix} \tag{5.41}$$

$$\vec{\eta} = \begin{bmatrix} \vec{\eta}_1 \\ \vec{\eta}_2 \end{bmatrix}. \tag{5.42}$$

The propagation equation for the state covariance matrix $P(t)$ is :

$$P_{k|k-1} = \Phi_{k-1} P_{k-1|k-1} \Phi_{k-1}^T + Q_{k-1}, \tag{5.43}$$

where Φ_{k-1} is the state transition matrix from t_{k-1} to t_k and Q_{k-1} is the process noise covariance matrix at time t_{k-1}. The subscript $k|k-1$ denotes a prediction value before it is updated at time t_k and $k|k$ means the updated value with new measurement at time t_k. The state transition matrix, $\Phi(t)$, is obtained by

$$\frac{d}{dt}\Phi(t, t_{k-1}) = F(t)\Phi(t, t_{k-1}) \tag{5.44}$$

with the initial condition

$$\Phi(t_{k-1}, t_{k-1}) = I_{6\times6}, \tag{5.45}$$

where $I_{6\times6}$ is a 6×6 identity matrix. For our system, the state-error transition matrix is

$$\begin{aligned} \Phi_{k-1} &\equiv \Phi(t_k, t_{k-1}) \\ &= \begin{bmatrix} \Theta_{k-1} & \Psi_{k-1} \\ 0_{3\times3} & I_{3\times3} \end{bmatrix}, \end{aligned} \tag{5.46}$$

where

$$\frac{d}{dt}\Theta(t, t_{k-1}) = [\hat{\omega}]\Theta(t, t_{k-1}) \tag{5.47}$$

$$\frac{d}{dt}\Psi(t, t_{k-1}) = [\hat{\omega}]\Psi(t, t_{k-1}) + I_{3\times3} \tag{5.48}$$

subject to

$$\Theta(t_{k-1}, t_{k-1}) = I_{3\times3} \tag{5.49}$$

$$\Psi(t_{k-1}, t_{k-1}) = 0_{3\times3}, \tag{5.50}$$

where $0_{3\times3}$ is a 3×3 zero matrix. Numerical integration, such as a Runge-Kutta method, is employed to solve for the transition matrix, $\Phi(t, t_{k-1})$. The process noise covariance matrix, Q_{k-1}, is used as a tuning parameter so that the optimal value may be found in a search to achieve the best attitude determination.

5.2.2 Observation Model

Two separate measurement models can be used for the EKF.

Unit Vector Filter (UVF) Observation Model

The measured star position is converted into a unit vector which is assumed to have the same noise characteristics for all three components regardless of the angle that the vector makes with the BD [44] [47]. The corresponding measurement covariance matrix is defined as :

$$R_k = \sigma_k^2 I_{3\times 3}, \tag{5.51}$$

where σ_k^2 is the variance of the star measurement noise on each component of the unit vector at time t_k. The measurement residual, $\vec{z}_k$, is defined by :

$$\vec{z}_k = \hat{W}_k - \hat{W}_{k|k-1}. \tag{5.52}$$

$\hat{W}_k$ is the unit vector measurement in the OBF and it is given by :

$$\hat{W}_k = A_k \hat{V}_k + \Delta \vec{W}_k \tag{5.53}$$

where $\hat{V}_k$ is the unit vector of the same star in the CRF and $\hat{W}_{k|k-1}$ is the prediction from :

$$\hat{W}_{k|k-1} = A_{k|k-1} \hat{V}_k, \tag{5.54}$$

where $\Delta \vec{W}_k$ is a white Gaussian noise. By representing the rotation as a matrix exponential [48] :

$$\begin{aligned} A_k &= e^{-[\delta\vec{\theta}]} A_{k|k-1} \\ &\approx (I - [\delta\vec{\theta}]) A_{k|k-1}. \end{aligned} \tag{5.55}$$

Inserting Equations 5.53, 5.54 and 5.55 into Equation 5.52 :

$$\vec{z}_k \approx [\hat{W}_{k|k-1}] \delta\vec{\theta}_k + \Delta \hat{W}_k. \tag{5.56}$$

The sensitivity matrix, H_k, can be derived as :

$$H_k = ([\hat{W}_{k|k-1}] \vdots 0_{3\times 3}). \tag{5.57}$$

QUEST Observation Model

The QUEST is a deterministic algorithm to compute the attitude quaternions from simultaneous vector measurements of celestial objects [49]. The vector measurement in the QUEST is given by :

$$\hat{W}_{k,i} = A_k \hat{V}_{k,i} + \Delta \hat{W}_{k,i}, \tag{5.58}$$

where the subscripts, i and k, are the measured star index and the measurement time, respectively. The QUEST algorithm furnishes attitude quaternions, p_k, as well as the error covariance matrix, R_k, which is given by :

$$R_k^{-1} = \sum_{i=1}^{n} \frac{1}{\sigma_{k,i}^2} [I - (A_k \hat{V}_{k,i})(A_k \hat{V}_{k,i})^T], \tag{5.59}$$

where $\sigma_{k,i}^2$ is the variance of star i's measurement noise at time t_k and n is the total number of the measured stars in the star tracker. The square roots of the diagonal elements of R_k are angle errors of the QUEST attitude. In the EKF, the QUEST quaternions, p_k, are combined with the predicted estimated quaternions, $q_{k|k-1}$, using to build the *O-C residuals*, $\bar{z}_k$, by

$$\bar{z}_k \equiv 2p_k \otimes q_{k|k-1}^{-1}, \tag{5.60}$$

where $\otimes$ is a quaternion composition analogous to an algebraic addition of two successive rotations [65]. $q_{k|k-1}$ is obtained by using the attitude propagation :

$$\frac{d}{dt}q(t) = \frac{1}{2}\Omega(\vec{\omega}(t))\ q(t) \tag{5.61}$$

from the estimated quaternions $q_{k-1|k-1}$ in the previous measurement time, t_{k-1}. and $\Omega(\vec{\omega})$ is :

$$\Omega(\vec{\omega}) \equiv \begin{bmatrix} 0 & \omega_z & -\omega_y & \omega_x \\ -\omega_z & 0 & \omega_x & \omega_y \\ \omega_y & -\omega_x & 0 & \omega_z \\ -\omega_x & -\omega_y & -\omega_z & 0 \end{bmatrix}. \tag{5.62}$$

The *O-C residuals* is divided into vector and scalar components :

$$\bar{z}_k \equiv \begin{bmatrix} \vec{z}_k \\ 1 \end{bmatrix}, \tag{5.63}$$

where the last component of $\bar{z}_k$ is, to the first order, 1, because $\bar{z}_k$ is expected to be a small amount of rotation. The observation-state equation thus is

$$\begin{aligned} \vec{z}_k &= \delta\vec{\theta}_k + \vec{v}_k \\ &= H_k \delta\vec{x}_k + \vec{v}_k, \end{aligned} \tag{5.64}$$

where $\vec{v}_k$ is a discrete white Gaussian noise vector originating from the QUEST measurement error. The sensitivity matrix, H_k, is

$$H_k = [I_{3\times3} \vdots 0_{3\times3}]. \tag{5.65}$$

5.2.3 Kalman Filter Update

The EKF update equations are :

$$K_k = P_{k|k-1}H_k^T(H_kP_{k|k-1}H_k^T + R_k)^{-1} \tag{5.66}$$

$$\delta\hat{x}_{k|k} = K_k\vec{z}_k \tag{5.67}$$

$$P_{k|k} = (I - K_kH_k)P_{k|k-1}(I - K_kH_k)^T + K_kR_kK_k^T \tag{5.68}$$

for both observation models. Note that $\delta\vec{x}_{k|k-1} = 0_{3\times3}$ in the EKF. For the UVF observation model, the update procedure is applied only when the measurement time changes. Finally, the new estimates at measurement time t_k are

$$q_{k|k} = 2\delta\hat{\theta}_{k|k} \otimes q_{k|k-1} \tag{5.69}$$

$$\hat{b}_{k|k} = \hat{b}_{k|k-1} + \Delta\hat{b}_{k|k}. \tag{5.70}$$

5.3 Batch Method

The normal equations for batch estimation are :

$$\delta\hat{x}_k = (H_k^T R_k^{-1} H_k + \bar{P}_k^{-1})^{-1}(H_k^T R_k^{-1} \vec{z}_k + \bar{P}_k^{-1}\delta\bar{x}_k) \tag{5.71}$$

$$P_k = (H_k^T R_k^{-1} H_k + \bar{P}_k^{-1})^{-1}, \tag{5.72}$$

where $\delta\hat{x}_k$ and P_k are the estimated state and covariance matrix at epoch time t_k while $\delta\bar{x}_k$ and $\bar{P}_k$ are the a priori state and covariance matrix at the same epoch time. Without any previous estimates, $\bar{P}_k$ is specified with arbitrarily large values. The terms containing the measurement covariance matrix, R_k in Equation 5.71 and 5.72 are computed by

$$H_k^T R_k^{-1} H_k = \sum_{i=1}^{n} (\tilde{H}_i \Phi(t_i, t_k))^T R_i^{-1} \tilde{H}_i \Phi(t_i, t_k) \tag{5.73}$$

$$H_k^T R_k^{-1} \vec{z}_k = \sum_{i=1}^{n} (\tilde{H}_i \Phi(t_i, t_k))^T R_i^{-1} \vec{z}_i, \tag{5.74}$$

where $\tilde{H}_i$ is the same as H_k in Equation 5.65 :

$$\tilde{H}_i = [I_{3\times3} \vdots 0_{3\times3}]. \tag{5.75}$$

R_i is the measurement noise covariance matrix at time t_i and $\vec{z}_i$ is the *O-C residual* vector defined in Equation 5.63 as $\vec{z}_k$. The transition matrix $\Phi(t_i, t_k)$ is obtained by :

$$\Phi(t_i, t_k) = \Phi(t_i, t_{i-1})\Phi(t_{i-1}, t_{i-2}) \cdots \Phi(t_{k+1}, t_k), \tag{5.76}$$

by computing transition matrices between all successive measurement times. This equation allows us to propagate attitude information from t_i to t_k considering noisy gyro data at each measurement time. Therefore, the attitude angle errors and gyro bias errors are determined by Equation 5.71 :

$$\delta\hat{x}_k = \begin{bmatrix} \delta\hat{\theta}_k \\ \Delta\hat{b}_k \end{bmatrix} \tag{5.77}$$

at the epoch time, t_k. Finally, quaternions and gyro biases at t_k are obtained by :

$$q_{k,m} = 2\delta\hat{\theta}_k \otimes q_{k,m-1} \tag{5.78}$$

$$\hat{b}_{k,m} = \hat{b}_{k,m-1} + \Delta\hat{b}_k, \tag{5.79}$$

where m is the iteration number. These are actually the same form as Equation 5.69 and 5.70 for the EKF, however, the states (q and $\vec{b}$) are renewed over the previous values at the epoch time in the batch estimation. The iterative procedure continues until the following condition is satisfied

$$|\vec{q}_{k,m} - \vec{q}_{k,m-1}| < \epsilon, \tag{5.80}$$

where ϵ is a pre-set value. Once the quaternions and biases are estimated at the epoch, the quaternions in every measurement time can be simulated by using Equation 5.61 through the time interval for batch. It is assumed that the estimated gyro biases are constants over a batch interval. At the next epoch, these gyro biases are used as initial values for another iteration.

5.4 Simulation Results

The CCD star tracker, Ball CT-601 or Raytheon HD-1003, has a capability of observing five or six stars simultaneously within the tracker FOV. Only a maximum of five stars were processed in our simulation. It is expected that the determined attitude quality will be slightly improved by increased number of stars in a FOV, whether it is noticeable or not.

Figure 5.1 shows the angle errors of the QUEST quaternions obtained from one orbital period of star tracker simulation data. Errors computed by comparison of the determined attitude with the true attitude show the noise-like behavior (the center part). There are two lines in the upper and lower parts corresponding to the computed 1σ values. Figure 5.2 shows the angle errors obtained from MFOAM with the same simulation data. The attitude errors (and also the computation times) obtained by two algorithms do not indicate noticeable differences. The uncertainty in each of the roll and pitch axes is about 3.5 arcseconds(1σ). The yaw error which is the angle error about an axis perpendicular to the tracker FOV is around 70 arcseconds(1σ). The estimation error in yaw is always much bigger than those in roll and pitch because the yaw axis (the zenith direction) is assumed to be aligned with the star tracker BD. For the pointing knowledge of the laser beam toward the nadir, it is required to know accurate angle rotations about the roll and pitch axes, but not about the yaw axis.

The results of attitude errors of all the SFAD methods discussed earlier are compared in Table 5.1. The five methods, QUEST, SVD, ITER, FOAM and MFOAM, do not show noticeable differences in the 1σ values. The approximate CPU times on a Hewlett Packard (HP) model 735/125 Unix machine, with 125 MHz processor, are compared in Table 5.2. Two algorithms, QUEST and MFOAM, show relatively fast performance. While the CPU time is important in real time attitude determination and control, the differences shown in Table 5.2 might be unimportant in post-processing. As long as there are no distinctive differences in accuracy, however, it would be better to choose the algorithm with the fastest performance.

Figure 5.3 shows the attitude angle errors from the EKF with the QUEST observation model. For the attitude propagation between star measurements, simulated gyro data were used. Noise-like true attitude errors and bounds (1σ envelopes) show significant improvement comparing to QUEST solutions (Figure 5.1). When less than three(≤ 2) stars are observed, gyro data are used to predict the attitude. During the absence of star tracker data, the 1σ envelope could not be drawn in Figure 5.3. The large covariance values were obtained by the restart of the EKF with the new star tracker measurements, but quickly the bound was diminished to the steady-state values.

Figure 5.4 shows the attitude angle errors obtained by the EKF with the UVF observation model. The batch estimation was performed with a 300 second batch interval and the results are shown in Figure 5.5. The batch intervals are marked by vertical dotted lines every 300 seconds in the figure. The estimated quaternions at the epoch time were propagated for 300 seconds (until the following epoch time) and the propagated quaternions were used to determine the angle errors shown in the figure. It can be seen that roll and pitch errors from the batch method are similar to those of the EKF methods.

Finally, Figure 5.6 shows the EKF with the QUEST observation model, but the EKF did not use gyro data at this time. Since angular rate information is required for quaternion propagation, the angular velocity vector, instead of gyro bias vector, was included in the

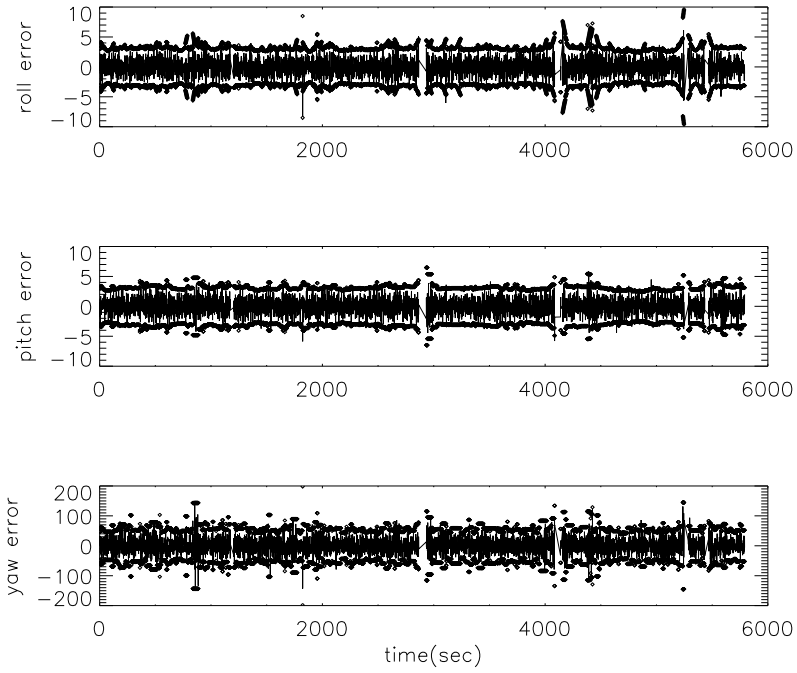

Figure 5.1: QUEST angle errors in arcsecond

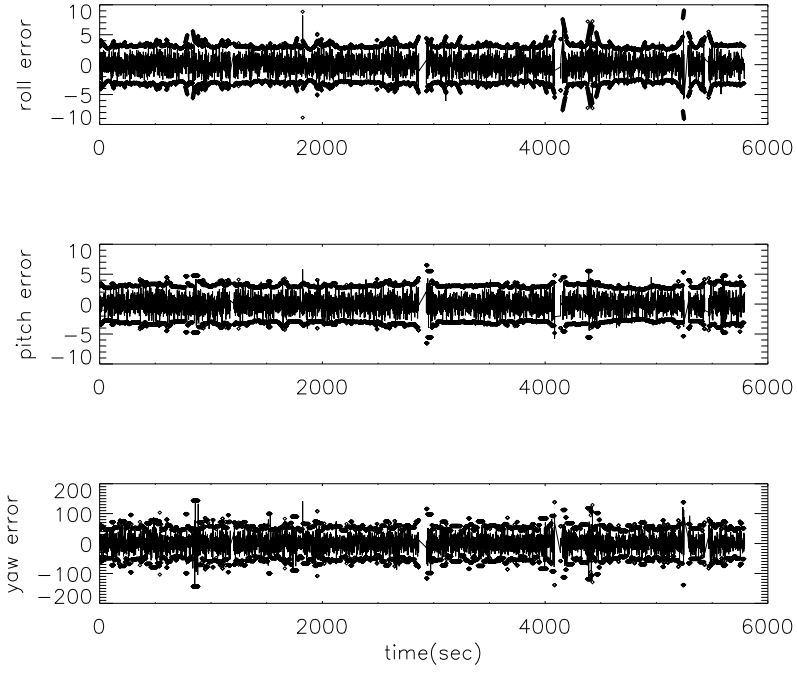

Figure 5.2: MFOAM angle errors in arcsecond

Table 5.1: SFAD output statistics. Mean errors are the averages of the determined yaw, roll and pitch errors from the known true attitude over one orbital period. The 1σs are the averages of the square root of the diagonal terms in the covariance matrix.

Method	Axis	Mean Error (arcsec)	1σ (arcsec)
QUEST	yaw	0.23	67.95
	roll	-0.00	3.40
	pitch	-0.02	3.45
SVD	yaw	-0.04	67.95
	roll	0.01	3.40
	pitch	-0.01	3.45
PD	yaw	-0.39	112.72
	roll	-1.50	5.52
	pitch	-0.27	5.71
IPD	yaw	0.55	67.95
	roll	0.04	3.40
	pitch	0.03	3.45
ITER	yaw	0.11	77.15
	roll	0.00	3.86
	pitch	-0.01	3.92
FOAM	yaw	-0.00	68.17
	roll	0.00	3.41
	pitch	-0.00	3.48
MFOAM	yaw	0.00	68.17
	roll	0.00	3.41
	pitch	-0.01	3.48

Table 5.2: SFAD computation time obtained by *time* command in HP 735/125 Unix machine with 125 MHz processor for one orbital period ($\approx$ 5800 seconds).

Method	user(sec)	system(sec)	real(min)
QUEST	92.8	23.7	1.58
SVD	99.0	23.5	2.03
PD1	93.4	23.6	1.58
PD2	94.3	23.9	2.01
ITER	107.9	23.2	2.13
FOAM	94.1	23.4	2.01
MFOAM	92.7	23.4	1.57

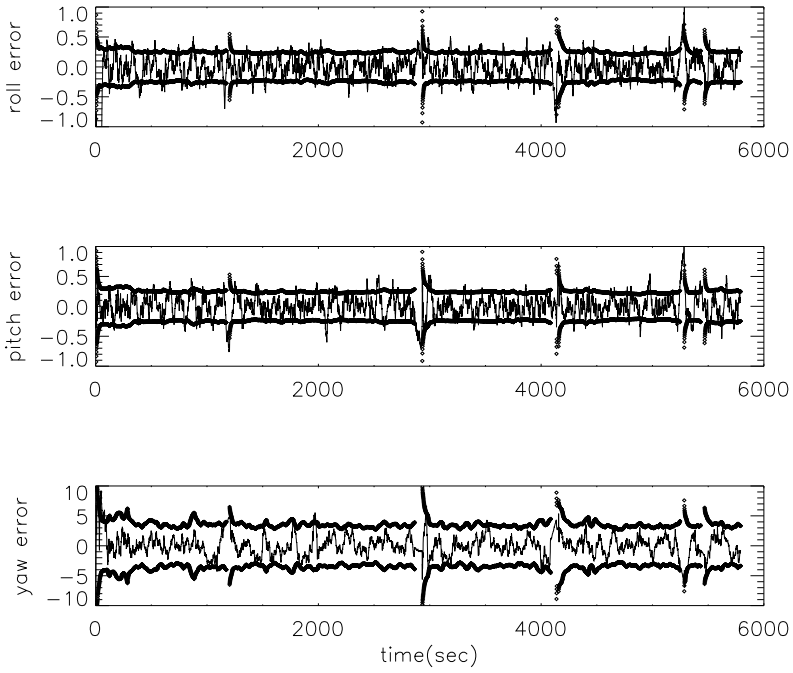

Figure 5.3: Angle errors from the EKF with QUEST observation model in arcsecond

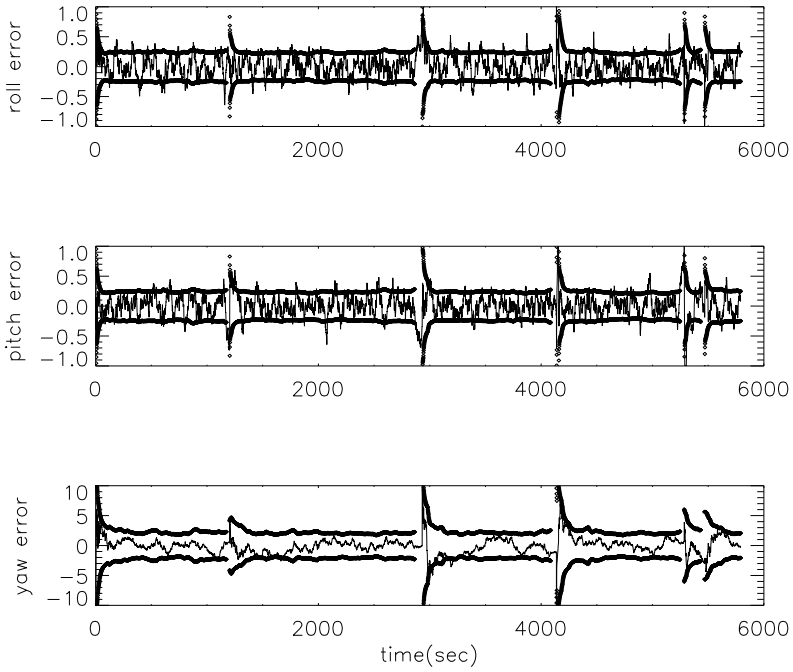

Figure 5.4: Angle errors from the EKF with UVF observation model in arcsecond

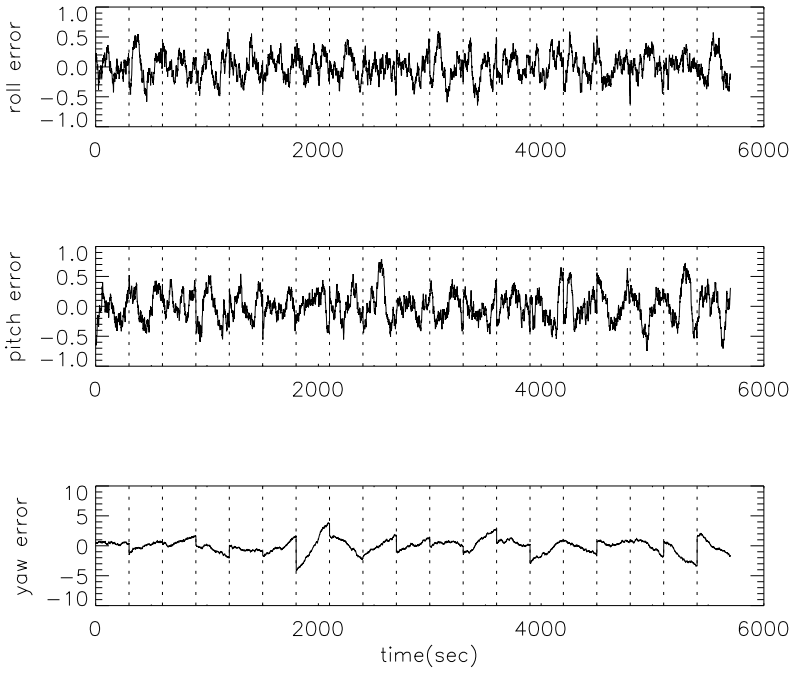

Figure 5.5: Angle errors from batch estimation in arcsecond

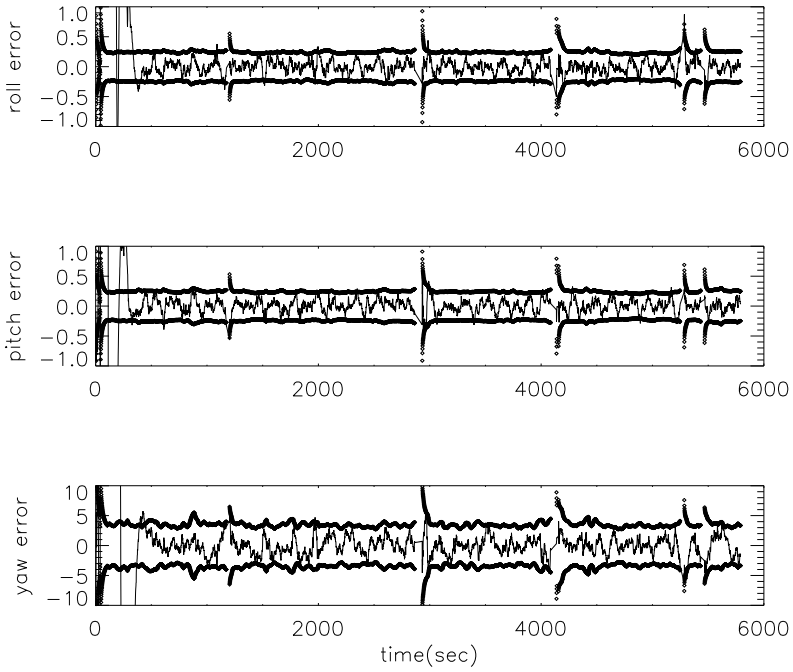

Figure 5.6: Angle errors from the EKF without using gyro data in arcsecond

Table 5.3: Computation time comparison

Method	Obs. Model		user(sec)	system(sec)	real(min)
EKF,	QUEST,	gyro	149.4	26.8	3.00
EKF,	QUEST,	non-gyro	143.9	24.7	2.51
EKF,	UVF,	gyro	341.5	10.1	6.00
BATCH,	QUEST,	gyro	451.2	92.0	9.08

state vector. Thus the equation of motions are now :

$$\frac{d}{dt}\delta\vec{\theta}(t) = [\vec{\omega}(t)]\delta\vec{\theta}(t) + \Delta\vec{\omega}(t) \tag{5.81}$$

$$\frac{d}{dt}\Delta\vec{\omega}(t) = \vec{\eta}(t), \tag{5.82}$$

where $\vec{\eta}(t)$ is white Gaussian noise on the angular acceleration. Most of the remaining equations are similar to the previous ones for the EKF using the QUEST observation model except for some modifications caused by the decrease in the number of noise parameters. The simulation results shown in Figure 5.3 and 5.6 might raise a question about the usefulness of the gyro data. However, it should be noted that the simulation did not include high frequency spacecraft jitter that may not be measured by the star camera, but could be measured by the gyros. Until the high frequency jitter is considered in the simulation (or in actual data process), it cannot be concluded that the EKFs, case using gyro data and case without using gyro data, produce the comparable results for attitude determination. The approximate computation times, required to process one orbital period of data on a HP model 735/125 Unix machine, with 125 MHz processor, are shown in Table 5.3. Both EKFs with the QUEST observation model perform the computation faster than the EKF with UVF observation model. The batch method, as expected, is slower than any EKF.

Figure 5.7 shows the relation between true estimation errors and a 1σ bound obtained from the state error covariance matrix. The numbers on the line are associated with the tuning parameter, the process noise covariance matrix. As the number increases (12, 13 $\cdots$), the magnitude of the process noise covariance matrix decreases. The EKF diverges when the process noise covariance matrix is too small.

Figure 5.8 shows the relation between true estimation errors and root mean squares (*rms*) of one orbital period EKF estimation. The trend of *rms* coincides with that of true errors. This particular case indicates the possibility of using *rms* values in the filter tuning of the actual data where the true attitude is not known.

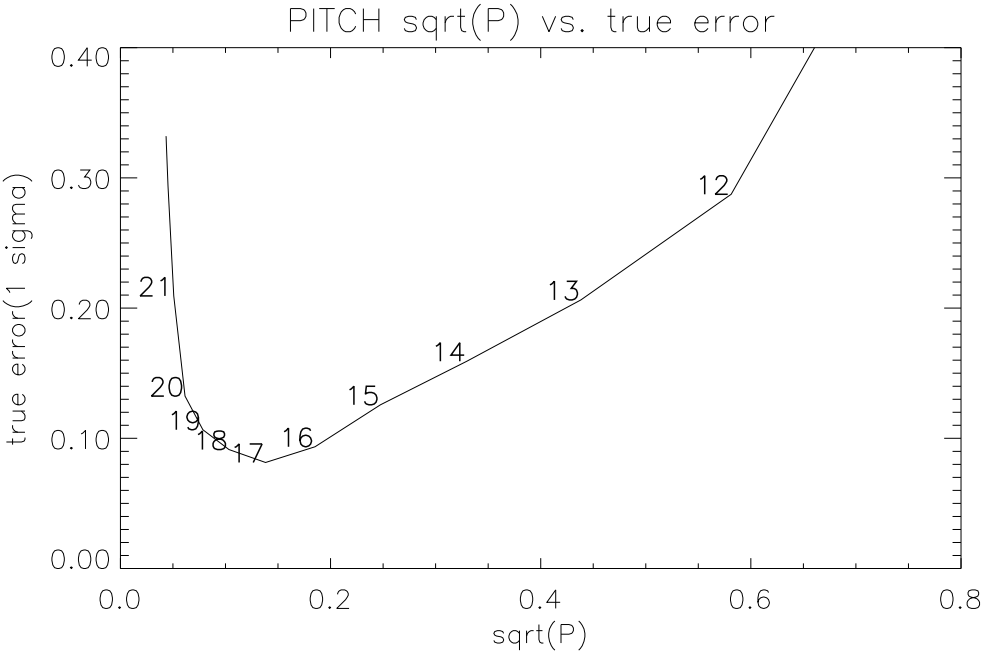

Figure 5.7: True errors versus 1σ values of EKF estimation (arcsecond)

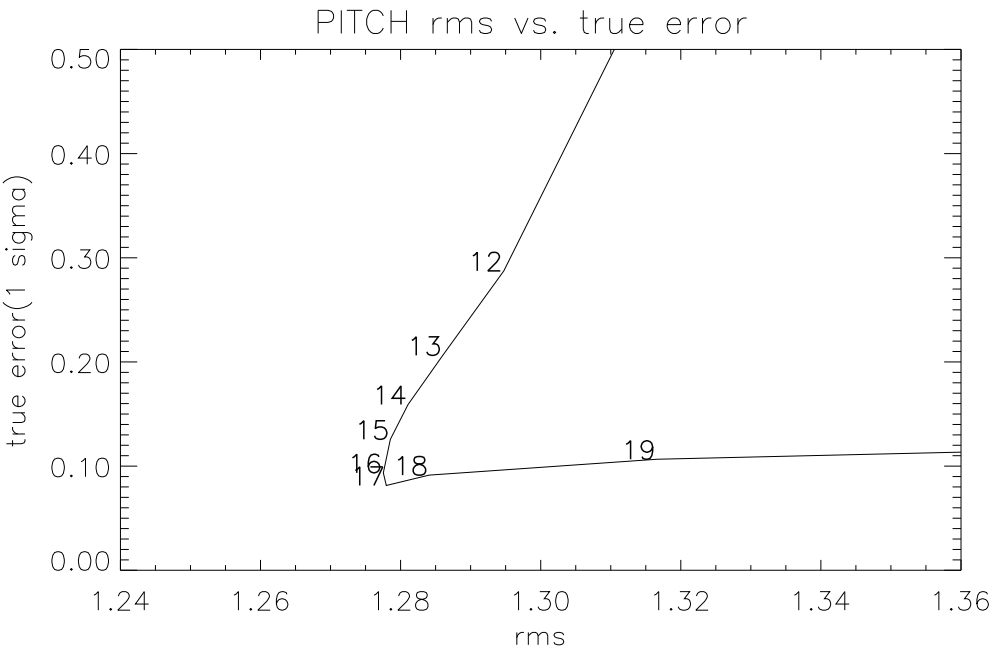

Figure 5.8: True errors versus *rms* values of EKF estimation (arcsecond)

Chapter 6

POINTING DETERMINATION

Figure 6.1 shows a conceptual sketch of the Stellar Reference System (SRS) which is being developed by Goddard Space Flight Center to measure the pointing angle of the GLAS laser beam to the required accuracy (less than 1.5 arcsecond, 1σ), relative to the star field. To reduce the alignment flexibility originating from multiple error sources, such as spacecraft jitter and temperature variation, all the components of the SRS will be attached to the GLAS optical bench. The SRS consists of a Laser Reference Camera (LRC) and the Attitude Determination System. The LRC contains optics, called Lateral Transfer Retroreflectors (LTR), which are designed to extract and redirect onto the Laser Reference Telescope (LRT) both a portion of the outgoing laser pulse and a beam from a Collimated Reference Source (CRS). The CRS is rigidly attached to a side of the star tracker and provides the alignment information of the star tracker. The LRT also observes a star (LRC star) which is brighter than 7.5 visual magnitude. All of the images observed in the LRT are projected onto a $0.5^\circ \times 0.5^\circ$ FOV Laser Reference Sensor (LRS). After locating the LRC star on the star field observed by the star tracker, other illuminated images in the LRS will subsequently be transformed to the star tracker star field in order to determine the laser altimeter pointing direction in the SCF or the OBF. When the LRC star is not available, the CRS images projected to the LRS will be monitored to check the stability of the whole system on the optical bench while the rigid body assumption is being applied. While the GLAS laser is fired at a 40 Hz rate, the LRS sees the laser at 10 Hz. The shot-to-shot direction of the laser beam is recorded by the Laser Profiling Array (LPA) with a frequency of 40 Hz. The centroids from 40 Hz laser images observed by the LPA must be located in the LRS frame and consequently in the SCF. Ultimately, the proper coordinate transformations would give us the 40 Hz laser beam pointing direction in both the TRF and the CRF. The details of the SRS instruments, such as mechanical requirements, design concepts, construction materials and statistical quantities, are provided in the GLAS Critical Design Review [60].

6.1 POINTING DETERMINATION ALGORITHM

Once a star observed in either the LRS or by the star tracker is identified, the star appears as a static point source in the CRF (see *Star Catalog* in Figure 6.2). The identified tracker stars will allow us to determine the attitude, $A(t)$, at time t by applying attitude determination algorithms. The attitude matrix transforms the star coordinates in the

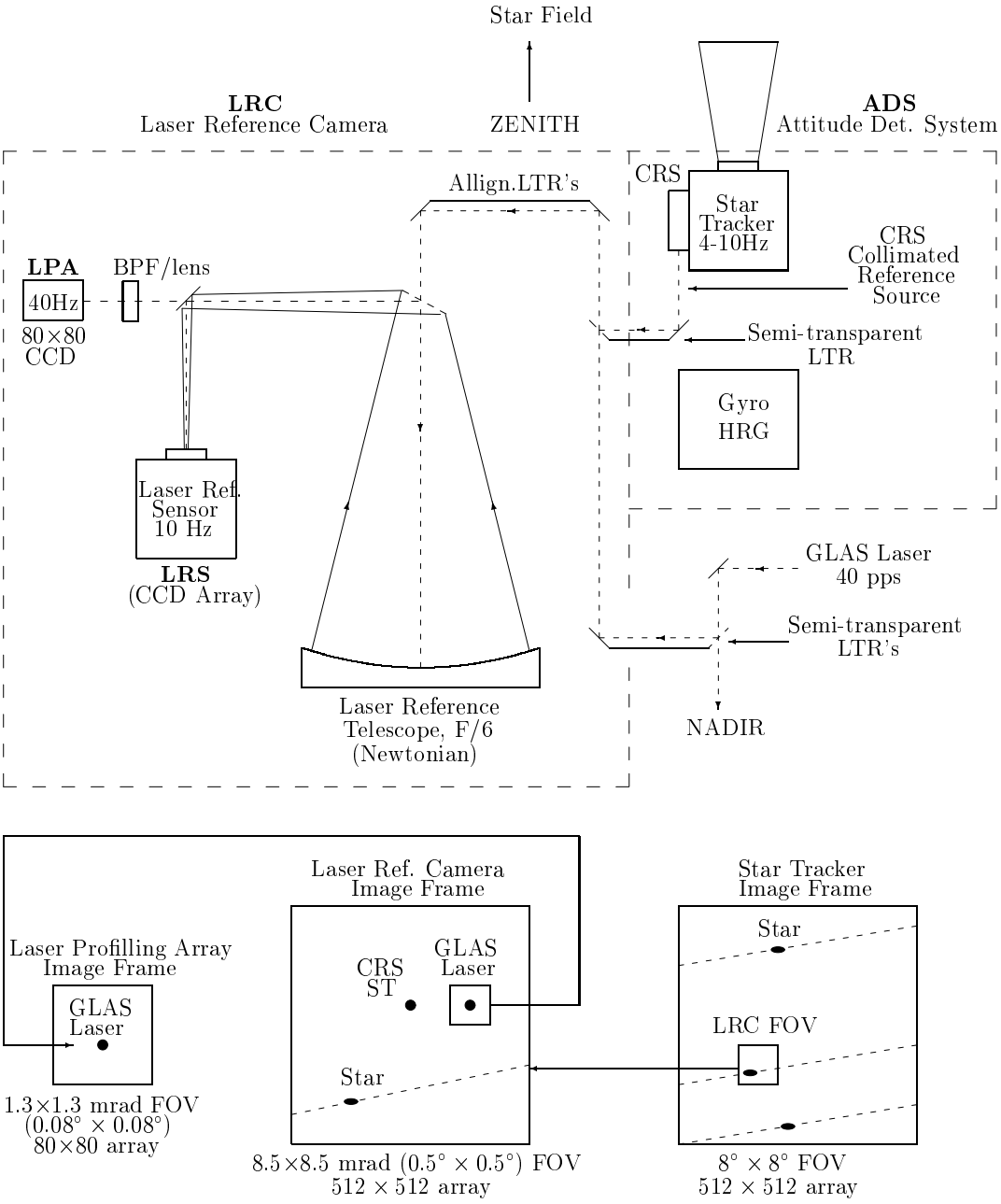

Figure 6.1: Stellar Reference System

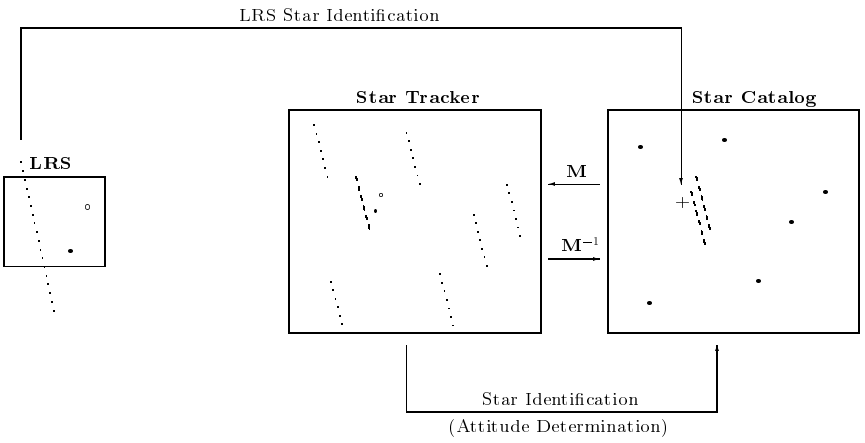

Figure 6.2: Pointing determination using the Stellar Reference System

CRF into those in the instrument OBF. If the alignment matrix, $S(t)$, which transforms the star coordinates in the OBF into those in the SCF, is temporarily presumed constant, the combined matrix, $M(t)$:

$$M(t) = S(t)A(t) \tag{6.1}$$

describes the coordinate transformation from the CRF to the SCF. Once the matrix, $M(t)$, is determined at every measurement time t, the LRC star identified in the CRF can be transformed to a dotted line at the star tracker FOV (see *Star Tracker* in Figure 6.2). The tracks of the LRC star both in the star tracker FOV and in the LRS FOV are input data to the least squares method which will be introduced in the following subsection. If the star in the LRC is brighter than magnitude 6, it will also be seen in the star tracker so that the projected LRC star positions on the star tracker FOV can be verified/calibrated with the observed star by the star tracker itself.*

6.1.1 Estimation of the LRS frame in terms of the SCF

Figure 6.3 describes the overlap of the LRS FOV on the star tracker FOV, but the LRS FOV is oversized to well visualize the relation between the two FOVs. Ideally, the two frames share the common origin. In the real situation, there might be an offset between the two origins. This offset is represented as the coordinate of the LRS origin, $(x_{offset},\ y_{offset})$, in terms of the SCF. In addition, the LRS FOV might rotate by angle θ against the SCF. Finally, the magnitude ratio of two FOVs, F, might change if focal lengths vary. Once we know these offset parameters, $(x_{offset},\ y_{offset},\ \theta,\ F)$, any point in the LRS FOV can be projected into the star tracker FOV using the following equation :

$$\begin{bmatrix} x_{star_{LRS}} \\ y_{star_{LRS}} \end{bmatrix} = F \begin{bmatrix} \cos\theta & \sin\theta \\ -\sin\theta & \cos\theta \end{bmatrix} \begin{bmatrix} x_{star_{ST}} - x_{offset} \\ y_{star_{ST}} - y_{offset} \end{bmatrix}. \tag{6.2}$$

where $(x_{star_{LRS}},\ y_{star_{LRS}})$ is the coordinate of the LRC star in the LRS frame and $(x_{star_{ST}},\ y_{star_{ST}})$ is the coordinate of the same star in the SCF. Considering the velocity

*Actual LRS performance was degraded because stars were only measured on the night side of the orbit. Laser pointing determination has been done using an alternative algorithm instead of the method described in this chapter. The new algorithm is described in Appendix B.

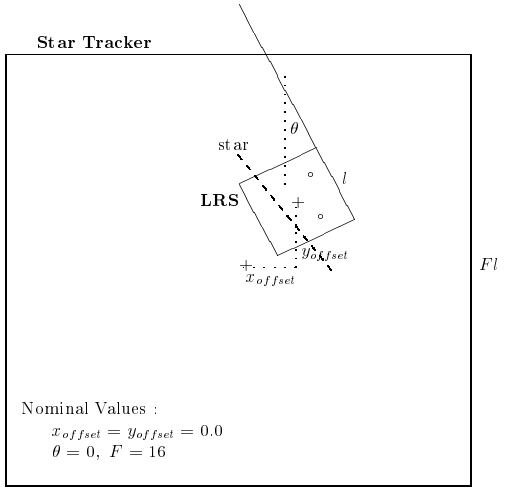

Figure 6.3: Estimation parameters for coordinate transformation between LRS frame and SCF

of the GLAS/ICESAT and the size of the LRS FOV, we will have approximately 80 points (i.e. 8 seconds) of the consecutive LRC star measurements in both FOVs. With these data, the offset parameters can be estimated by applying the least squares method [58] to the Equation 6.2. Finally, Equation 6.2 is used to locate the laser point in the star tracker FOV by inserting the estimated parameters, $\hat{x}_{offset}$, $\hat{y}_{offset}$, $\hat{\theta}$ and $\hat{F}$:

$$\begin{bmatrix} x_{laser_{LRS}} \\ y_{laser_{LRS}} \end{bmatrix} = \hat{F} \begin{bmatrix} \cos\hat{\theta} & \sin\hat{\theta} \\ -\sin\hat{\theta} & \cos\hat{\theta} \end{bmatrix} \begin{bmatrix} x_{laser_{ST}} - \hat{x}_{offset} \\ y_{laser_{ST}} - \hat{y}_{offset} \end{bmatrix}, \tag{6.3}$$

where $(x_{laser_{LRS}},\ y_{laser_{LRS}})$ are the coordinates of the LRS laser in the LRS frame and $(x_{laser_{ST}},\ y_{laser_{ST}})$ are the coordinates of the same laser point located in the SCF. Equation 6.3 is also used for the projection of the CRS point. After the laser points observed in the LRS FOV are located in the SCF, direction cosines (i.e. unit vector for the laser pointing direction) can be restored by considering the focal length of the star tracker. The construction of the laser pointing vector will be made once the laser travel time (i.e. range) is determined. The inverse of the matrix $M(t)$, $M(t)^{-1}$, should be applied to transform the laser coordinates from the SCF to the CRF. As discussed at the end of Section 1.1, the laser spot position vector will be obtained by appropriately combining the laser pointing vector with the laser pulse travel time and the POD position vector. The spot location will be produced in the Earth-fixed axes, specifically ITRF by the proper coordinate transformation [42].

A simulation result for GLAS laser pointing determination is shown in Figure 6.4. The LRC star measurement data were created from a star catalog which contains 32511 stars ranging down to magnitude 7.5. The LRC star measurement noise was in the range of 0.2 to 0.4 arcsecond depending on the star brightness [60]. In addition to the random noise in the overall SRS, the true shot-to-shot variation of the laser beam direction was given as 0.3 arcsecond (1σ). The pointing errors in the figure are the absolute differences between the true and the estimated pointing directions. For the most part, the pointing errors were below 1.5 arcseconds, satisfying the accuracy requirement.

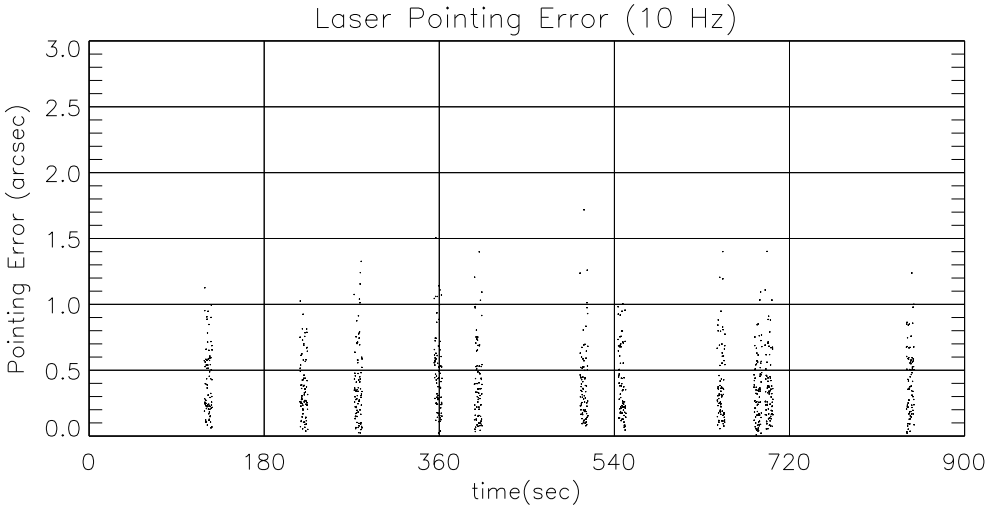

Figure 6.4: Pointing determination simulation result (10Hz)

6.1.2 Absence of the LRC Star

As shown in Figure 6.4, a half degree LRS FOV will occasionally observe stars. The time duration before a new star comes in to the LRS appears to be within a few minutes in the figure. To determine the maximum or average time between LRC star observations, simulations covering the whole sky might be necessary. The probability computation of the star tracker's star observations, from both theory and simulation, indicated that the stars in our universe do not deviate considerably from the random distribution (see Table 3.4). Using the Poisson distribution[63], the computation shows that, during an orbital period of the GLAS, a star will be observed in the LRS more than 100 occasions, meaning at least a star per minute. Therefore, the LRS would almost always observe a new star within several minutes after the dropout of an old one, especially in the polar regions where no solar or lunar blocking would occur. Expecting that the line of sight stability for the GLAS optical bench would be less than 0.1 arcsecond(1σ) during one orbital period [34] [43], we conclude that the offset parameters obtained during a LRC star observation can be used after the star leaves the LRS FOV. When a new star comes into the LRS, the parameters will be updated and used until another new star is observed. If a noticable change of instrument alignment between star tracker and LRS occurs, it would be detected by monitoring the CRS points since the LRS also observes the CRS images projected from the star tracker CRS. Figure 6.5 shows the simulation results after filling up intervals between LRS observations using constant offset parameters before a new star.

6.1.3 LPA measurement projection into LRS frame

While the LRS sees star, laser and CRS points at a 10Hz rate, the LPA observes the laser beam at a 40Hz rate. The position of the laser in the LPA needs to be located in the LRS in order to determine the 40Hz laser beam pointing direction in the CRF. Although the LPA consists of an array of 80 by 80 pixels, only 20 by 20 array containing the laser point near its center will be read. An example of the laser profile is shown in Figure 6.6.

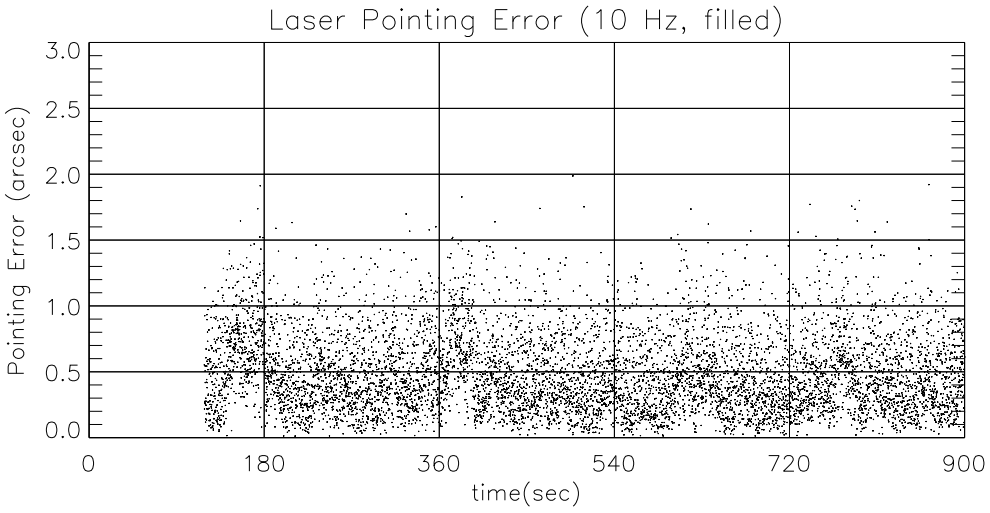

Figure 6.5: Pointing determination simulation result (10Hz, filled)

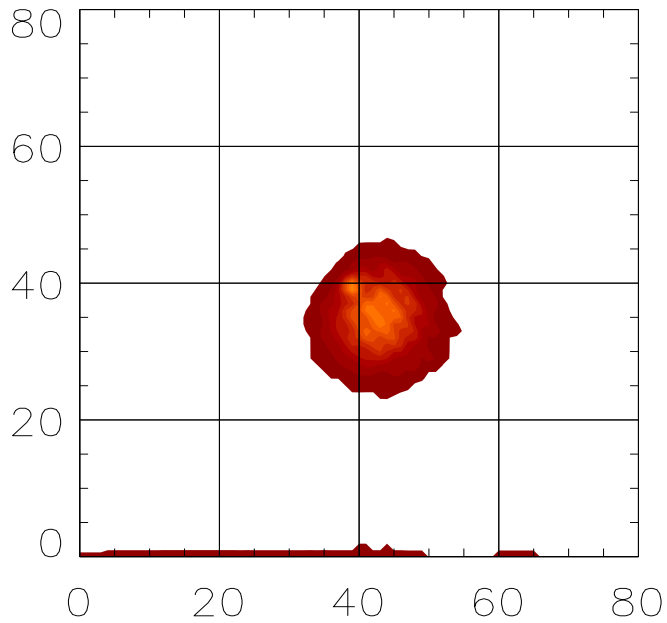

Figure 6.6: Laser profile observed at the LPA

A method to find the centroid $(x_{i,LPA}, y_{i,LPA})$ of the laser image is :

$$\begin{aligned} x_{i,LPA} &= \frac{\sum_1^{20} n \sum_1^{20} m \; I_{m,n}}{\sum_1^{20} \sum_1^{20} n \; m \; I_{m,n}} \\ y_{i,LPA} &= \frac{\sum_1^{20} m \sum_1^{20} n \; I_{m,n}}{\sum_1^{20} \sum_1^{20} n \; m \; I_{m,n}} \end{aligned} \tag{6.4}$$

where $I_{m,n}$ is the laser intensity of m row and n column.

Pre-launch calibration will provide the formula to project the LPA laser point to the LRS frame. However, the relative position of the LPA frame with respect to the LRS frame might change slowly due to launch load, temperature variation or instrument aging. The center of the LPA laser image needs to be located in the LRS FOV after launch. Since both the LRS and the LPA observe the same laser shots at a 10Hz rate (see Figure 6.1), these common measurements provide a way to project the LPA image center to the LRS coordinate frame. Measurements of laser in both LRS and LPA frames will contain both shot-to-shot noise and measurement noise. The mean position, $(x_{LPA},\ y_{LPA})$ is computed by :

$$\begin{aligned} x_{LPA} &= \frac{\sum_1^N x_{i,LPA}}{N} \\ y_{LPA} &= \frac{\sum_1^N y_{i,LPA}}{N}, \end{aligned} \tag{6.5}$$

where N is the number of total measurements, i is an index for the individual measurement and $(x_{i,LPA},\ y_{i,LPA})$ is described in Equation 6.4. Similarly, the mean position of LRS laser is calculated by :

$$\begin{aligned} x_{LRS} &= \frac{\sum_1^N x_{i,LRS}}{N} \\ y_{LRS} &= \frac{\sum_1^N y_{i,LRS}}{N}. \end{aligned} \tag{6.6}$$

Finally, an individual LPA centroid, $(x_{i,LPA_{on}LRS},\ y_{i,LPA_{on}LRS})$, is projected into the LPA frame by :

$$\begin{aligned} x_{i,LPA_{on}LRS} &= K(x_{i,LPA} - x_{LPA}) + x_{LRS} \\ y_{i,LPA_{on}LRS} &= K(y_{i,LPA} - y_{LPA}) + y_{LRS}, \end{aligned} \tag{6.7}$$

where K is the ratio of size difference between the two frames. The projection procedure is illustrated in Figure 6.7 as a linear transformation of a coordinate system whose origin is located at the mean position of the LPA centroids.

The laser point projection represented by Equation 6.7 is based on the assumption that the coordinate axes of the LPA are parallel to those of the LRS. The rotation angle of the LPA frame, θ, with respect to the LRS frame is illustrated in Figure 6.8 where the mean position of the LPA centroids is moved to the origin of the LRS frame. If we consider the rotation angle θ, the observed or uncorrected LPA laser point, $(x_{i,uncor},\ y_{i,uncor})$, will become the corrected one, $(x_{i,cor},\ y_{i,cor})$, by :

$$\begin{bmatrix} x_{i,cor} \\ y_{i,cor} \end{bmatrix} = \begin{bmatrix} \cos\theta & \sin\theta \\ -\sin\theta & \cos\theta \end{bmatrix} \begin{bmatrix} x_{i,uncor} \\ y_{i,uncor} \end{bmatrix}. \tag{6.8}$$

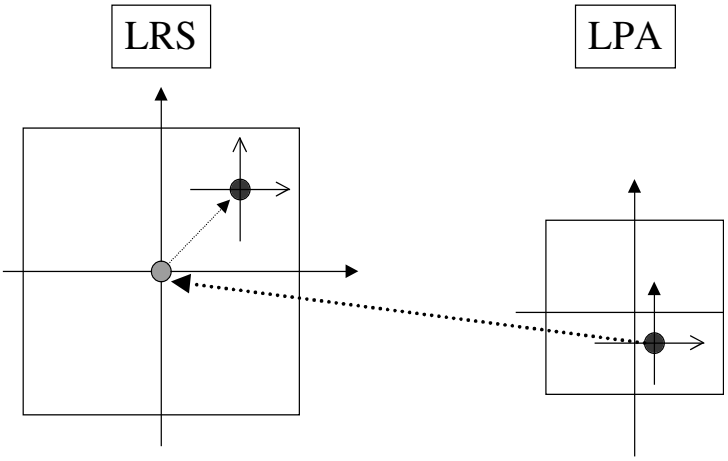

Figure 6.7: Projection of LPA frame on LRS frame

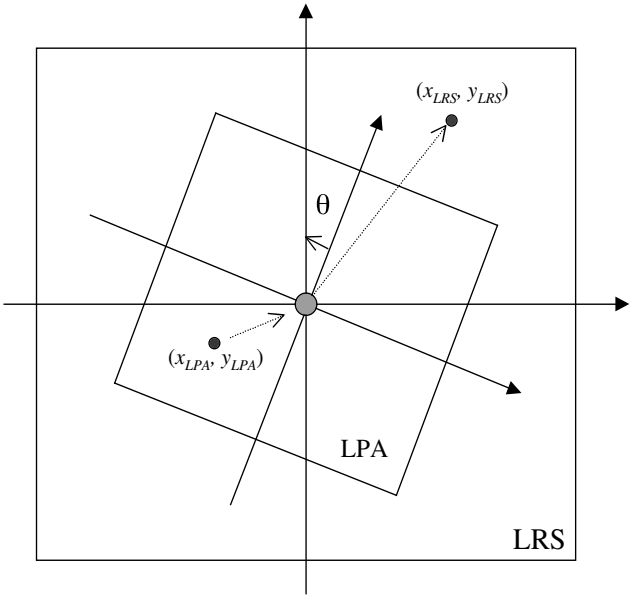

Figure 6.8: Rotation of LPA frame with respect to LRS frame

Errors of LPA position, when the rotation is not considered, are computed by :

$$\Delta r_i = (\Delta x_i^2 + \Delta y_i^2)^{\frac{1}{2}}, \tag{6.9}$$

where

$$\begin{aligned} \Delta x_i &= x_{i,cor} - x_{i,uncor} \\ \Delta y_i &= y_{i,cor} - y_{i,uncor}. \end{aligned} \tag{6.10}$$

Equation 6.8 implies that the size of Δr_i is determined by both θ and δr_i, where δr_i is defined by :

$$\delta r_i = (x_{i,uncor}^2 + y_{i,uncor}^2)^{\frac{1}{2}}. \tag{6.11}$$

As we mentioned before, the uncertainty of δr_i on LPA measurements consists of two components: measurement noise and shot-to-shot variation. The peak shot-to-shot variation is expected to be one arcsecond [50]. The magnitude of the measurement noise would be less than one arcsecond (1σ) [32]. The optical bench vibration and instrument distortion are expected to be 0.45 arcsecond in total (1σ). The systematic component for those errors is not clearly quantified, but the long term line of sight instabilities of the instrument optical benches observed or required in other missions [20] [34] [43] lead us to believe that the value should remain within 0.5° (3 σ) during 5 years in orbit even in the worst case. Inserting values

$$\begin{aligned} \delta r_i &< 4\ arcseconds(3\sigma) \\ \theta &\ll 0.5^\circ (= 1800\ arcseconds), \end{aligned}$$

into Equation 6.8, 6.9 and 6.10, we have

$$\Delta r_i = 0.06\ arcsecond.$$

This is clearly negligible when we consider other error sources in the SRS [32]. Therefore, Equation 6.7 would be sufficient to project the LPA centroids into LRS frame without worrying about the effect of the relatively rotated coordinate axes between two frames.

6.1.4 40 Hz LPA measurements

Equation 6.7 should apply to 40 Hz LPA measurement data even though the mean position of the LRS laser image will be obtained from 10 Hz measurement data. In order to use Equation 6.1 for transforming all of the laser points from the SCF to the CRF, the attitude, $A(t)$, needs to be known at a 40 Hz rate. Since the attitude, $A(t)$, is determined from star tracker and gyro data whose measurement rates are only 10 Hz, a linear interpolation is required to get the instrument attitude at 40 Hz. This interpolation can be justified only if the LPA frame is relatively fixed with respect to the LRS frame during the interval in which the interpolation is applied (i.e. 1 second). If the instrument or optical bench has significant high frequency jitter, the interpolated attitude might produce unacceptable pointing error, then it might be necessary to use gyros capable of 20 Hz or 40 Hz rate measurements.

Figure 6.9 illustrates the overall measurement relations between star tracker, LRS and LPA. The final products of the PAD are laser pointing unit vectors in both ICRF and ITRF.

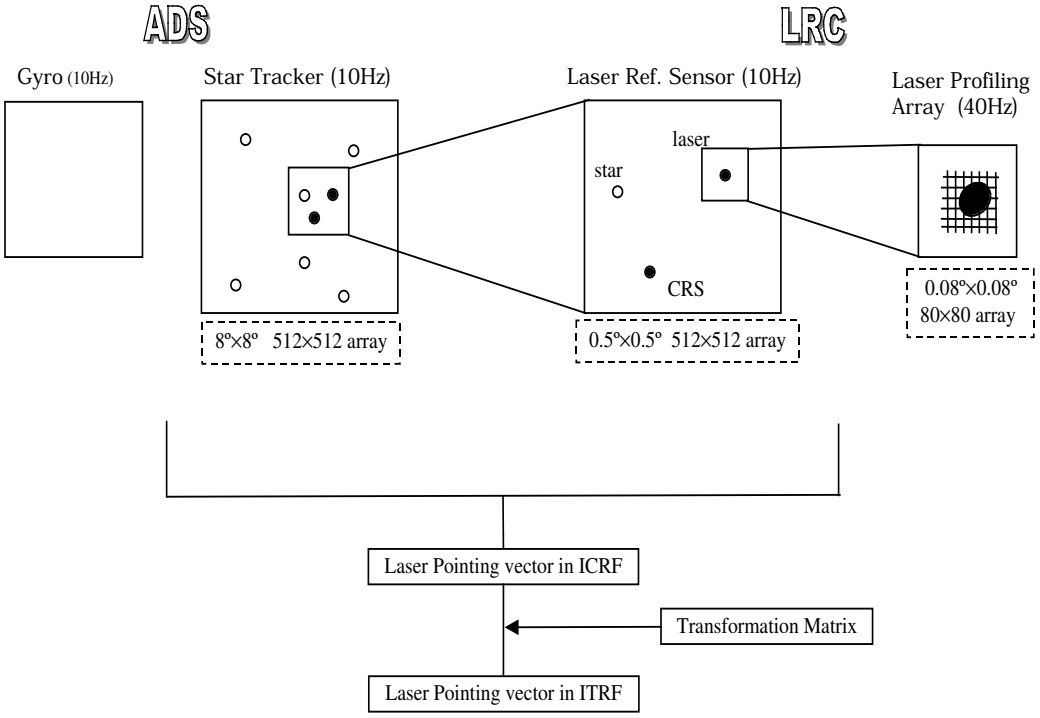

Figure 6.9: SRS overall procedure

6.1.5 Collimated Reference Source (CRS)

The CRS, which will be mounted kinematically to the reference surface on the star tracker, will maintain true pointing direction and collimation of its own laser pulse. The stability requirement is 0.2 arcseconds (1σ) over a $\pm 0.5°$C gradient [60]. From the error sources in the relay of the CRS beam including LRT distortion and LRC centroid error, the measurement error in the LRC is expected to be similar to that of the LRC star. The monitoring of the CRS beam image over time will allow us to monitor the SRS structure stability and to verify the image quality in the LRC. Furthermore, during the loss of star tracker data due to, for example, solar and lunar eclipsing - the maximum duration is about 20 minutes (see Section 3.3) - the offset parameters in Equation 6.2 may be presumed as constants if the CRS image remains in the stable position without any systematic change. The angular diameters of the Sun and the Moon are both approximately 0.5°, which is the size of the LRC FOV. As long as the LRC is not under the direct illumination of the Sun or the Moon, the LRC is expected to provide centroids of both CRS and laser images at the 10 Hz rate. By applying the algorithm depicted in the previous sections, the 40 Hz laser pointing determination will be available with the LPA laser images.

6.2 Spacecraft Velocity Influence on Laser Pointing

In Section 3.3.3, a simplified algorithm, to correct the stellar aberration, was shown. The PAD of the spacecraft is determined within the CRF and must be corrected for this effect,

stellar aberration being the result of the spacecraft (and the star tracker) motion with respect to the relatively fixed stars. In like manner, the motion of the spacecraft with respect to a point on the surface of the Earth will cause a similar effect that can be tentatively called *pointing aberration*. Figure 6.10 illustrates both stellar and pointing aberrations. Since the aberration is a function of relative velocity, and not the distance, between the observer and the source, the same algorithm can be applied. For pointing aberration, the applicable velocity is the relative velocity of the Earth with respect to the spacecraft. The magnitude of the pointing aberration can be calculated by Equation 3.14 :

$$\begin{aligned} \beta_p &= \frac{|\vec{v}|}{c} \sin\theta \\ &= \frac{|-\vec{v}_{s/c}|}{c} \\ &\cong 5.2 \text{ arcseconds} \end{aligned}$$

where the θ is always close to 90° because of the near-nadir pointing direction of the laser.

The pointing aberration will shift the angle of incidence from the laser direction that will be determined by the PAD processing. In other words, the laser spot will not be located at the path of the laser determined by the PAD. Instead, the laser will hit the ground at the path of the shifted direction. Without applying the effect of the pointing aberration the laser pointing direction determined from the GLAS instrument data will miss the actual laser spot by about 15 meters corresponding to 5.2 arcseconds.

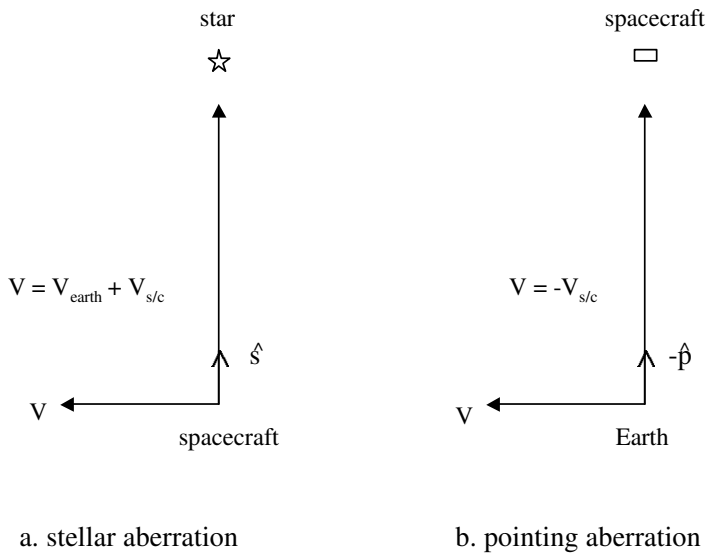

Figure 6.10: Two aberrations due to the motion of the spacecraft

6.3 Systematic Errors

6.3.1 Systematic Errors in the Stellar Reference System

The pointing determination algorithm described in the previous section applied the inverse of the matrix $M(t)$, $M(t)^{-1}$, to transform the estimated laser pointing direction from the SCF to the CRF. The laser pointing direction was determined in the SCF by referencing the LRC star trajectory transformed from the CRF to the SCF using the matrix $M(t)$. Since we are ultimately interested in the laser beam direction in the CRF, the systematic errors embedded in the matrix $M(t)$ might be canceled out by two way (i.e. direct and inverse) implication of the matrix $M(t)$ to and from the SCF at a measurement time t. The matrix $M(t)$ is the combination of the attitude matrix, $A(t)$, and the alignment matrix, $S(t)$. The conceivable systematic error sources for the attitude matrix $A(t)$ are the star tracker CCD array pixel biases, gyro non-orthogonality and aberration correction errors. The alignment matrix $S(t)$ can contain the systematic error due to the excursion of the star tracker BD.

The excursion of the BD was added to the simulated star tracker data. The laser pointing direction was determined by the process introduced in earlier section. Figure 6.11 shows the computed laser pointing errors (i.e. true laser pointing direction minus estimated laser pointing direction) for 600 seconds with various amount of the BD error. The first plot (a) is the result when no BD error was included in star tracker data. The average of the pointing error during the LRC star presence was 0.49 arcsecond. The addition of the 200 arcseconds error on the star tracker BD did not change the pointing determination error. The average of the pointing error was again 0.49 arcsecond in the second plot (b). When the BD error becomes 1 degree, the average of the pointing error increased to 0.84 arcsecond as seen in the third plot (c). With a BD error of 5 degrees, the pointing estimation no longer produces acceptable results as shown in the fourth plot (d). A similar simulation can be applied for the effect of the systematic errors included in the attitude matrix $A(t)$. However, different approaches for the attitude systematic errors are discussed in the following section.

6.3.2 Systematic Errors in Attitude Determination

A Ball CT-601 star tracker was used for the high accuracy attitude determination of the Midcourse Space Experiment (MSX) mission [19]. The highest accuracy that the MSX had to achieve for the instrument pointing stability was 2 arcseconds (1σ). While the pre-launch simulation showed the fulfillment of the attitude determination/pointing requirement, the MSX could not determine the attitude to the required accuracy from the actual star tracker and gyro data. In the attitude determination simulation before launch, some fundamental assumptions were made. Eventually, the assumptions turned out to be inadequate for the actual data processing. One of these assumptions concerned the characteristics of the star tracker measurement errors. While these errors were presumed to be adequately modeled as *white noise* in the simulation, the individual pixel of the star tracker CCD array included its own bias, eventually, resulting in the error of the star image centroid. Since the effect of the systematic error can not be removed by the usual statistical estimation procedures, the attitude determined by the *white noise* assumption could not satisfy the accuracy requirement.

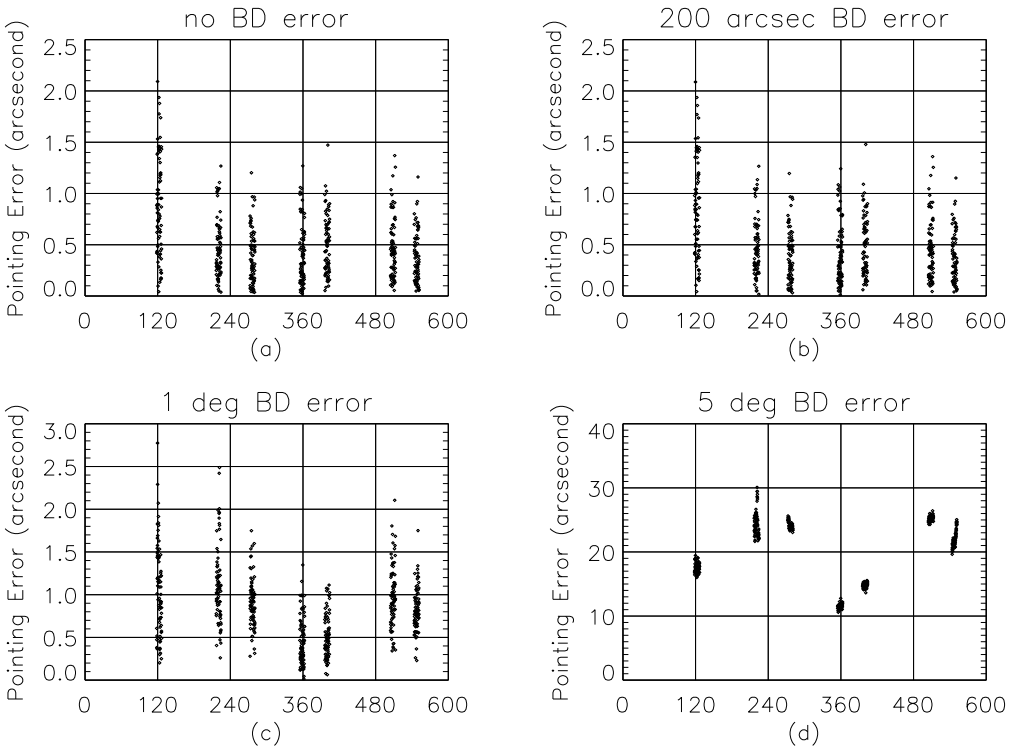

Figure 6.11: Effect of the BD error in the Stellar Reference System

While the MSX is completely versatile, with science scenarios varying from inertial stares to whole sky scans to tracking satellites, ballistic missiles and their surrogates, and covering about anything in between, the GLAS/ICESAT will maintain one attitude scenario : altimeter laser pointing toward the near-nadir direction in near-circular and near-polar orbit. A star would come in and move across the $8^\circ \times 8^\circ$ FOV with a relatively constant rate for about 4 minutes until it exits. By considering 512 by 512 pixels in the CCD array, a star will stay on a pixel about 0.25 seconds. Unlike the case of the inertial staring attitude where one pixel sees a star for long duration, the pixel's local bias will affect the star measurement in two or three snaps, and then the star moves into the next pixel that would be characterized by its own size and direction for bias. Moreover, the attitude determination algorithms will utilize multiple stars which will be located at all different pixels in the tracker CCD array at a measurement time. In this situation, the change of pixel biases of five or six star observations should be considered as random and the residual effect of the systematic error sources would be negligible.

By using the bias correction tables within the post facto attitude determination software, the Roentgen Satellite (ROSAT) mission corrected the star tracker cameras' measurements in pointing mode [37]. For the GLAS, it is expected that the manufacturer will provide the built-in bias calibration function of the star tracker [50] to remove both the individual pixel biases and the large distortion of the CCD array before the data are actually taken. This self-calibration ability of the star tracker will, at least, reduce the size of the bias errors significantly, if not remove them completely.

The SRS ability to cancel out the measurement systematic error was also discussed

in the previous section. The laser pointing determination algorithm using the specially designed SRS will avoid the systematic errors embedded in the alignment matrix $S(t)$, as well as in the attitude matrix $A(t)$. When we consider only instrument pointing determination, the SRS should be able to remove the effects of many systematic error sources even at the inertially staring attitude mode of the spacecraft.

Besides the *white noise* model for the star tracker measurements, another inadequate assumption for the MSX attitude determination system was the obtainability of the uninterrupted star tracker attitude data at its nominal update rate of ≈ 9 Hz. Extensive analytic studies indicated *fairly strongly that glint from the Sun is a significant problem, possibly because of unanticipated reflections off the SPIRIT III (one of the MSX's instrument) shield* [19]. The unexpected glint would require the tracker integration time to be longer than anticipated, which will result in the large image smearing and interrupted data rate. The Kalman filters and the batch algorithm introduced in Chapter 2 are capable of estimating the gyro biases as well as the spacecraft attitude quaternions. The high frequency attitude update due to 10 Hz star tracker measurement rate will make the gyro biases include not only true bias but also other effects such as gyro non-orthogonality, gravity or magnetic effects [59]. Since the star tracker and gyro unit are located on the optical bench which is designed to hold the rigidity between instruments, the self-calibrating capability of gyro systematic errors by estimating gyro biases will be kept as long as the star tracker provides high frequency observations. The failure to achieve the star tracker measurements at the anticipated rate probably made the MSX attitude determination suffer from the MSX gyros systematic errors other than true biases. The GLAS requires the precise attitude/pointing determination in the high latitude regions such as Greenland and Antarctica ($|\delta| > 60°$). Since the Sun and the Moon, the possible cause of the glint, are located near the ecliptic plane ($|\delta| \approx 23.5°$), the effect of the Sun and the Moon light on the star tracker measurement should be minimal and uninterrupted tracker data rate is expected. Consequently, the Kalman filter that estimates both the attitude quaternions and the gyro bias simultaneously would provide the auto-calibration feature for the gyro's systematic errors, if the HRG of the GLAS suffers from problems similar to the MSX gyro.

Chapter 7

IMPLEMENTATION CONSIDERATIONS

7.1 Standards

To facilitate generation of the laser pointing direction, the attitude should be expressed using reference frames common to those used in description of the orbit position. As discussed by Rim and Schutz [35], the POD process will provide the position of the spacecraft/instrument center of mass in the ICRF which is the specific implementation of the CRF. The determination of the transformation matrix between the spacecraft-fixed axes and the CRF depends, in part, on the adopted star catalog used with the analysis of star camera data. In mid 1997, the Hipparcos star catalog was released containing more than 100,000 sources with position precision better than one mas (see Table 3.5). Although additional analysis will be required, it is expected that the Hipparcos catalog will be the foundation of the GLAS PAD.* Additional stars were available with the Hipparcos release, known as the Tycho catalog, but with precision at the 30 mas level. Nevertheless, the Tycho contribution contains about one million stars. The Hipparcos source coordinates will be defined for an epoch corresponding to J2000 and the reference system will be realized through the ICRF. The proper motions in the catalog are better than 1 mas/yr. The Hipparcos catalog will link the optical sources (used by Hipparcos) to the radio sources (used by the IERS) at a level better than 1 mas [27]. Further discussion is given by McCarthy [31].

Conceptually, the determination of the laser spot location will be determined in the ICRF using the spacecraft center of mass ephemeris from the POD and the transformation matrix from the PAD to determine the measured height vector. This height vector will be transformed into the ITRF using the IERS measured UT1, as well as precession and nutation parameters. The same transformation between the ICRF and the ITRF is required in the POD process. The transformation into the ITRF from the ICRF is well established at the milliarcsecond level.

*The Hipparcos and Tycho catalogs provide high-quality astrometric and photometric data for virtually all SKY2000 stars in Version 2 and later versions. The *SKY2000 Master Catalog* (Version 2) was used in practice as the foundation of the GLAS PAD.

Table 7.1: Overall attitude determination accuracy goal

	roll(arcsec)	pitch(arcsec)
1.Attitude Determination	0.47	0.47
2.Velocity Aberration	0.03	0.03
3.Star Position Accuracy	0.03	0.03
4.Ephemeris	0.01	0.01
RSS(2,3,4) + 1	0.52	0.52

7.2 Ancillary Inputs

Ancillary inputs include a subset of a master star catalog.† and a luni-solar-planetary ephemerides, such as DE-200 or later [55]. The latter complements the star catalog by enabling identification of solar system bodies in camera images. For the generation of the transformation between the spacecraft-fixed axes and the ICRF, the velocity aberration corrections of the observed stars are needed (see Section 3.3.3 and Table 7.1). The ephemeris of the GLAS satellite determined in the POD processing will be known with accuracy better than the real time flight operations ephemeris. In addition, to expedite the PAD process, access to the real time attitude determination from the flight operations segment is required. This information will reduce the search time to identify stars in the star camera images by providing a priori attitude information of modest accuracy.

The POD process requires real time attitude information as well as a modest accuracy a priori ephemeris. The present algorithm development will pursue independent POD and PAD processes to simplify software validation, even though these processes (including the laser pointing process) share common aspects. The common parameters will be made available through shared files.

7.3 Accuracy and Validation

An estimate of the attitude determination accuracy is shown in Table 7.1 [60]. While the star catalog is expected to introduce no significant errors into the estimation process, the star camera will be the dominant source of error. The RSS of roll and pitch, which will affect the laser pointing direction, is 0.85 arcsecond. The overall RSS of all the error sources for the laser pointing determination is expected to be 1.20 arcsecond (1σ) (see Table 1.1). The simulation in this document did not include unmeasured errors, stemming from the unsensed bench vibration and the unsensed angular distortions. Even though the pointing errors shown in the plots in Chapter 6 will increase slightly when these unmeasured errors are taken into account, the resultant 1σ value should be smaller than 1.20 arcsecond considering the magnitude of the unmeasured errors and our simulation results.

Detailed discussion for the attitude validation is contained in the Calibration/Validation Plan [61]. In summary, a first order validation of attitude will be conducted by comparisons with the real time determination. This approach, however, is limited because the real time requirements are about 10-20 arcseconds (1σ), compared to 1 arcsecond (1σ)

†The master star catalog is SKY2000 catalog. The subset is GLAS PAD mission star catalog.

required for science analysis. As described in this plan, validation of the attitude at the 1 arcsecond level is inherently linked to laser pointing. Experiments to validate the laser pointing will simultaneously assess the PAD.

7.4 Computational: CPU, Memory and Disk Storage

The requirements for the product of the PAD, the 3×3 transformation matrix between spacecraft-fixed axes and the ICRF, will require about 300 MB/day. Alternatively, about 150 MB/day would be required if 4 quaternion elements were used at each time instead of 9 matrix elements. Preliminary tests show that an HP735-level machine can support the required attitude determination; however, further tests will be conducted to provide a more definitive estimate for CPU, memory and disk storage.

The approximate CPU times for one orbital period of data processed with the EKF algorithms on a HP model 735/125 Unix machine were given in Table 5.2. From the table, the processing time for one day attitude of data is estimated to be approximately 45 minutes for the EKF using the QUEST observation model and 90 minutes for the one using the UVF model. The batch algorithm is expected to require about 135 minutes for the same amount of data. The overall PAD process will require additional CPU time for the SRS data processing discussed in Chapter 6 and the data preprocessing.

7.5 Sensor Failures

Although the PAD study has been done with a star tracker in the instrument optical bench, there will exist two additional CCD star trackers (Ball CT-602) mounted on the spacecraft structure. The primary purpose of the spacecraft star trackers is to provide data for the real time attitude determination. The spacecraft star tracker data will be available on the ground and the additional star measurement data can be used for PAD in post-processing. Since the BDs of the CT-602 star trackers will not be parallel to that of the instrument star tracker, the contribution of this star tracker to the determination of the laser pointing direction is limited by the amount of the angle between star trackers' BDs. However, in case the instrument star tracker malfunctions, the Ball CT-602 star trackers' data must be used to produce the best laser pointing information.

This idea can be extended when the optical bench star tracker loses data temporarily due to solar and lunar eclipsing with no permanent failure. Instead of totally depending on the CRS image stability as discussed in Section 6.1.5, it might be possible to use the attitudes obtained by the CT-602 star trackers whose BDs are 30° away from the optical bench star tracker. The calibrated data of the CT-602 trackers in terms of the instrument star tracker will provide 10 Hz attitude determination for the PAD with degraded accuracy.

Meanwhile, the situation is not the same for gyro failure since there is no alternative system in the spacecraft. There are two possible ways to generate angular rates without the actual rate measurement even though the accuracy level is in doubt. The first choice is to use the Euler equation (Equation 2.18) to compute the spacecraft angular rates. For this case, the numerical or analytical expression for external torques must be modeled as a function of time as well as a function of the position and attitude of the spacecraft. The other choice is already mentioned in Section 5.4 when the EKF simulation results were discussed. The EKF without using gyro data showed equal or better accuracy in

attitude determination. However, it was indicated that the real spacecraft motion may contain high frequency noise which can be detected only by gyros. Even though the replaced system/method to the original PAD system will not determine the attitude to the required accuracy level, preparation of alternatives to produce the most accurate attitude determination as a backup plan is prudent.

Bibliography

[1] European Space Agency. *The Hipparcos and Tycho Catalogues.* ESA Publications Division, 1997.

[2] S. Bae, R. Ricklefs, N. Smith, and B. Schutz. Time tag issues in the star tracker and gyro data for ICESat precision attitude determination. *AAS*, (09-128), 2009.

[3] S. Bae and B. Schutz. ICESat/GLAS attitude determination using a batch least squares estimator during star tracker starless periods. *AIAA*, (2002-4915), 2002.

[4] S. Bae and B. Schutz. Star tracker misalignment calibration for the ICESat mission. *AAS*, (06-107), 2006.

[5] S. Bae, N. Smith, and B. Schutz. ICESat attitude and pointing correction using the laser reference sensor. *AAS*, (10-140), 2010.

[6] S. Bae, C. Webb, and B. Schutz. GLAS PAD calibration using Laser Reference Sensor data. *AIAA*, (2004-4857), 2004.

[7] Ball Aerospace Engineering. *CT-601 Solid-State Star Tracker.*

[8] I.Y. Bar-Itzhack. Polar decomposition for attitude determination from vector observation. *AIAA*, (92-4545), 1992.

[9] E. Bertin and S. Arnouts. SExtractor:Software for source extraction. *Astronomy and Astrophysics Supplement*, 117(2), 1996.

[10] C. Buil. *CCD Astronomy : Construction and Use of an Astronomical CCD Camera.* Willmann-Bell, Richmond, Va., 1st English edition, 1991.

[11] L.W. Cassidy. Miniature star tracker for precise attitude reference in space. Technical Report PA 1868, Hughes Danbury Optical Systems, Inc., 1995.

[12] V. Chobotov. *Spacecraft Attitude Dynamics and Control.* Krieger Publishing Co., Malabar, 1991.

[13] Raytheon Systems Company. GLAS Star Tracker Test Results. Systems Engineering Memorandum, March 2000.

[14] R.L. Farrenkopf. Analytic steady-state accuracy solutions for two common spacecraft attitude estimators. *Journal of Guidance and Control*, 1(4), Jul–Aug 1978.

[15] D.R. Fink, K.B. Chapman, W.S. Davis, J.A. Hashmall, S.E. Shulman, S.C. Underwood, J.M. Zsoldos, and R.R. Harman. Experience gained from launch and early orbit support of the Rossi X-ray Timing Explorer(RXTE). In *Flight Mechanics/Estimation Theory Symposium*, Publication 3333. National Aeronautics and Space Administration Conference, May 1996.

[16] H.L. Fisher, M.D. Shuster, and T.E. Strikwerda. Attitude determination for the star tracker mission. *AAS*, (89-365), 1989.

[17] R. Fowell, N. Smith, S. Bae, and B. Schutz. Bad stars. *AAS*, (09-012), 2009.

[18] D.T. Greenwood. *Principles of Dynamics*. Prentice-Hall, Inc., New Jersey, 1988.

[19] D.R. Haley, T.E. Strikwerda, H.L. Fisher, and G.A. Heyler. Attainable pointing accuracy with star trackers. *AAS*, (98-072), 1998.

[20] K.A. Havey, G.L. Compagna, and N. Lynch. Precision Thermal Control Trades for Telescope Systems. *SPIE*, 3356, 1998.

[21] S.B. Howell, editor. *Astronomical CCD Observing and Reduction Techniques*, volume 23 of *Astronomical Society of the Pacific conference series*, San Francisco, California, 1992. Astronomical Society of the Pacific.

[22] J.L. Junkins and J.D. Turner. *Optimal Spacecraft Rotational Maneuvers*. Elsevier Publishing Company, New York, 1986.

[23] E.J. Lefferts, F.L. Markley, and M.D. Shuster. Kalman filtering for spacecraft attitude estimation. *Journal of Guidance, Control, and Dynamics*, 5(5), 1982.

[24] I.T. Lewis, A.G. Ledebuhr, T.S. Axelrod, J.F. Kordas, and R.F. Hills. WFOV star tracker camera. *Sensors and Sensor Systems for Guidance and Navigation, SPIE*, 1478, 1991.

[25] C.C. Liebe. Star trackers for attitude determination. *IEEE Aerospace and Electronic Systems Magazine*, Jun 1995.

[26] S. Lim and B.E. Schutz. Repeat ground track analysis for the geoscience laser altimeter system. *AAS*, (96-205), 1996.

[27] L. Lindegren and J. Kovalevsky. Linking the Hipparcos catalogue to the extragalactic reference frame. *Astron. Astrophys.*, 304, 1995.

[28] F.L. Markley. Attitude determination using vector observations and the singular value decomposition. *The Journal of the Astronautical Sciences*, 36(3), Jul–Sep 1988.

[29] F.L. Markley. Attitude determination and parameter estimation using vector observations : Theory. *The Journal of the Astronautical Sciences*, 37(1), Jan–Mar 1989.

[30] F.L. Markley. New quaternion attitude estimation method. *Journal of Guidance, Control, and Dynamics*, 17(2), Mar–Apr 1994.

[31] D. McCarthy. IERS Conventions (1996). *Int. Earth Rotation Serv. Tech. Note 13*, July 1996.

[32] P.S. Millar. Stellar Reference System. In *GLAS Critical Design Review*. NASA/GSFC, March 1999.

[33] D. Mortari. A fast on-board autonomous attitude determination system based on a new star-ID technique for a wide FOV star tracker. *AAS*, (96-158), 1996.

[34] D.C. Neam and J.D. Gerber. Structural Design and Analysis for an Ultra Low CTE Optical Bench for the Hubble Space Telescope Corrective Optics. *SPIE*, 1690, 1992.

[35] H.J. Rim and B.E. Schutz. GLAS Precision Orbit Determination (POD). Algorithm Theoretical Basis Document (ATBD) Version 2.1, February 2001.

[36] H.J. Rim, C. Webb, and B.E. Schutz. Analysis of GPS and Satellite Laser Ranging (SLR) data for ICESAT precision orbit determination. *AAS*, (99-146), 1999.

[37] Th. Rupp and G. Schneiders. High-accurate attitude determination for the X-ray satellite Rosat. *Journal of Guidance, Control, and Dynamics*, 15(3), May–Jun 1992.

[38] B. Schutz, S. Bae, L. Magruder, R. Ricklefs, H. Rim, E. Silverberg, C. Webb, and S. Yoon. Precision orbit and attitude determination for ICESat. *AAS*, (03-282), 2003.

[39] B. Schutz, S. Bae, N. Smith, and M. Sirota. Precision orbit and attitude determination for ICESat. *AAS*, (08-305), 2008.

[40] B. Schutz, H. Zwally, C. Shuman, D. Hancock, and J. DiMarzio. Overview of the ICESat mission. *Geophysical Research Letters*, 2005. 32, L21S01, doi:10.1029/2005 GL024009.

[41] B.E. Schutz. Spaceborne Laser Altimetry : 2001 and Beyond. In *Book of Extended Abstracts, WEGENER-98*. Norwegian Mapping Authority, Honefoss, Norway, 1998.

[42] B.E. Schutz. GLAS Laser Footprint Location (Geolocation) and Surface Profiles. Algorithm Theoretical Basis Document (ATBD) Version 2.1, February 2001.

[43] R.B. Schweickart and M.M. Buchko. Flexible Heat Pipes for CCD Cooling on the Advanced Camera for Surveys. *SPIE*, 3356, 1998.

[44] J. Sedlak and D. Chu. Kalman filter estimation of attitude and gyro bias with the QUEST observation model. *AAS*, 93(297), 1993.

[45] S.W. Shepperd. Quaternion from rotation matrix. *J. Guidance and Control*, 1, 1978.

[46] M.D. Shuster. Maximum likelihood estimation of spacecraft attitude. *The Journal of the Astronautical Sciences*, 37(1), Jan–Mar 1989.

[47] M.D. Shuster. Kalman filtering of spacecraft attitude and the QUEST model. *The Journal of the Astronautical Sciences*, 38(3), Jul–Sep 1990.

[48] M.D. Shuster. A survey of attitude representation. *The Journal of the Astronautical Sciences*, 41(4), Oct–Dec 1993.

[49] M.D. Shuster and S.D. Oh. Three-axis attitude determination from vector observations. *J. Guidance, Control, and Dynamics*, 4(1), 1981.

[50] M. Sirota. Goddard Space Flight Center. Private Communication.

[51] N. Smith. *Localized Distortion Estimation and Correction for the ICESat Star Trackers.* M.s. thesis, Department of Aerospace Engineering Mechanics, The University of Texas at Austin, 2006.

[52] N. Smith, S. Bae, and B. E. Schutz. Biased star tracker measurements of forty-nine stars from flight data. *Journal of Spacecraft and Rockets*, 47(6), 2010.

[53] N. Smith, R. Fowell, S. Bae, and B. E. Schutz. Improved star tracker instrument magnitude prediction from ICESat flight telemetry. *AAS*, (11-086), 2011.

[54] M.T. Soyka and P.J. Melvin. Hercules : Gyro-based, real-time geolocation for an astronaut camera. *AAS*, 91(533), 1991.

[55] E. Standish. Orientation of the JPL ephemerides, DE200/LE200, to the dynamic equinox of J2000. *Astron. Astrophys.*, 114, 1982.

[56] J. Stauffer. Creation of a Guide Star Catalog for the BASG CT-601 Star Tracker. personal contact, 1994.

[57] C. Sterken and J. Manfroid. *Astronomical Photometry : A Guide*, volume 175, chapter 13. Kluwer, Academic Publishers, Dordrecht, The Netherlands, 1992.

[58] G. Strang. *Linear Algebra and Its Applications.* Harcourt Brace Jovanovich College Publishers, Orlando, FL, 1986.

[59] T.E. Strikwerda and J.L. Junkins. Star pattern recognition and spacecraft attitude determination. Technical Report ETL-0260, U.S. Army Engineer Topographic Laboratories, Fort Belvoir, Virginia, May 1981.

[60] GLAS Instrument Team. GLAS Critical Design Review. March 1999.

[61] GLAS Science Team. GLAS Calibration/Validation Plan. Version 0.9, August 2000.

[62] R.W.H. van Bezooijen. True-sky demonstration of an autonomous star tracker. *SPIE*, 2221, 1994.

[63] J.D. Vedder. Star trackers, star catalogs, and attitude determination : Probabilistic aspects of system design. *Journal of Guidance, Control, and Dynamics*, 16(3), May–Jun 1993.

[64] G. Wahba. A least squares estimate of satellite attitude. *SIAM Review*, 8(3), Jul 1996.

[65] J.R. Wertz, editor. *Spacecraft Attitude Determination and Control.* D. Reidel, Dordrecht, the Netherlands, 1978.

[66] D. Wright and D. Bunke. The HRG as applied to a satellite attitude reference system. *AAS*, (94-004), 1994.

[67] D. Zimbelman. CT-601 star tracker behavior, April 1998. Goddard Space Flight Center.

ACKNOWLEDGMENTS

The authors would like to acknowledge the contributions of Marcos Sirota, Pamela Miller, Joe Garrick and Peter Gonzales, all from NASA Goddard Space Flight Center. Preparation of this document has been supported by NAS5-99005.

Appendix A

ICESAT MISSION OUTLINE

The Ice, Cloud and land Elevation Satellite (ICESat) was launched on 13 January 2003. The Geoscience Laser Altimeter System (GLAS) instrument onboard ICESat made its first laser elevation measurement of the Earth on 21 February 2003 and its last on 11 October 2009. The three lasers employed by GLAS did not perform as long as expected, and following the failure of Laser 1 on 5 March 2003 the ICESat mission was modified to meet the requirement for capturing a multi-year time series of ice sheet elevations [40]. For the modified mission scenario, the spacecraft entered a 91-day repeat science orbit (compared to a planned 183-day repeat) and the lasers were activated for about 33 days of this 91-day repeat, two or three times per year. This campaign mode operation is summarized in Table A.1, and other significant parameters and events are listed in Table A.2.

Table A.1: ICESat Laser Operation Campaigns

Campaign	Year	Day of year	Calendar Dates	Number of days (d)	Repeat orbit (d)	Repeat tracks[1]
L1a	2003	051-088	20 Feb-21 Mar	37	8	001-072 to 006-023
L2a	2003	268-277/ 277-322	25 Sep-4 Oct/ 4 Oct-21 Nov	54	8/ 91	028-088 to 029-100/ 1098 to 0421
L2b	2004	048-081	17 Feb-21 Mar	33	91	1284 to 0421
L2c	2004	139-173	18 May-21 Jun	34	91	1283 to 0434
L3a	2004	277-313	3 Oct-8 Nov	37	91	1273 to 0452
L3b	2005	048-083	17 Feb-24 Mar	35	91	1258 to 0426
L3c	2005	140-174	20 May-23 Jun	34	91	1275 to 0421
L3d	2005	294-328	21 Oct-24 Nov	34	91	1282 to 0421
L3e	2006	053-087	22 Feb-28 Mar	34	91	1283 to 0424
L3f	2006	144-177	24 May-26 Jun	33	91	1283 to 0421
L3g	2006	298-331	25 Oct-27 Nov	33	91	1283 to 0423
L3h	2007	071-104	12 Mar-14 Apr	33	91	1279 to 0426
L3i	2007	275-309	2 Oct-5 Nov	34	91	1280 to 0421
L3j	2008	048-081	17 Feb-21 Mar	33	91	1282 to 0422
L3k	2008	278-293	4 Oct-19 Oct	15	91	1283 to 0145
L2d	2008	330-352	25 Nov-17 Dec	22	91	0096 to 0423
L2e	2009	068-101	9 Mar-11 Apr	33	91	1286 to 0424
L2f	2009	273-284	30 Sep-11 Oct	11	91	1280 to 0084

[1] There are 119 tracks in the 8-day orbit and 1354 tracks in the 91-day orbit. Cycle numbers are included for the 8-day repeat periods.

ICESat laser campaigns are designated by a laser number (L1, L2 or L3), followed by a letter in the sequence of operation. Following campaign L2f, attempts to restart any of the lasers were not successful. The spacecraft was put through a series of engineering tests in early 2010. De-orbit maneuvers were carried out in June and July 2010. The spacecraft was *passivated* on 14 August and reentered the Earth's atmosphere on 30 August 2010 over the Barents Sea northeast of Norway.

Table A.2: Significant ICESat Parameters and Events by Campaign

Cam-paign	Year	Day of year	S/C orient-ation[1]	Start Beta' Angle (º)	End Beta' Angle (º)	Start Laser Infrared Energy (mJ)	End Laser Infrared Energy (mJ)	Mean footprint semi-major axis (m)	Day of year – comments
-	2003	013	-	-	-	-	-	-	013 – launch
L1a	2003	051-088	-Y/+X	-45	-32	72	51	149	080 – yaw flip 085 – safe hold, adjust temperature
L2a	2003	268-277/ 277-322	+Y	51	69	80	55	100	277 – orbit change 286 – laser temperature anomaly 287, 302 – adjust temperature 311 – GPS solar flare anomaly
L2b	2004	048-081	+Y	54	40	57	33	90	
L2c	2004	139-173	-X	13	-4	33	5	88	142-147 – adjust temperature
L3a	2004	277-313	-Y	-48	-58	67	62	56	293 – adjust temperature
L3b	2005	048-083	-Y	-56	-45	68	54	80	054 – suspected amplifier bar drop, begin footprint anomaly[2] 068 – suspected amplifier bar drop
L3c	2005	140-174	+X	-20	-4	49	44	55	
L3d	2005	294-328	+Y	51	63	43	39	52	
L3e	2006	053-087	+Y	62	48			52	
L3f	2006	144-177	-X	20	4			51	
L3g	2006	298-331	-Y	-44	-54			53	310 – begin ITRF 2005
L3h	2007	071-104	-Y	-60	-47			56	
L3i	2007	275-309	+Y	32	46			57	
L3j	2008	048-081	+Y	74	62			59	
L3k	2008	278-293	+X	-28	-32			52	
L2d	2008	330-352	-Y	-45	-53			-	343-344 – adjust temperature
L2e	2009	068-101	-Y	-71	-59			-	094-095 – adjust temperature
L2f	2009	273-284	-X	20	25			-	
-	2010	242	-	-	-	-	-	-	242 – reentry

[1] The spacecraft is said to be in "Sailboat" mode for ±Y orientations and in "Airplane" mode for ±X orientations, where the direction indicates the solar panel orientation with respect to the spacecraft velocity using the GLAS coordinate frame.
[2] The footprint diameter during L3b changed from a mean of 54 m (day of year 048-053) to 84 m (055-068). The reason for the larger footprint size during the latter part of the campaign is unknown, although a suspected amplifier bar dropout occurs near the event.

Appendix A was written by Tim Urban at Center for Space Research, The University of Texas at Austin.

Appendix B

PROCESSING METHODS FOR POINTING DETERMINATION

The pointing determination algorithm described in Chapter 6 was developed based on the intended SRS behavior. In other words, the algorithm was a pre-launch processing design corresponding to the pre-launch SRS design. After launch, there were significant problems with the SRS system and the pointing determination algorithm was adapted to on-orbit SRS performance. For example, there were significant problems with the Laser Reference Sensor (LRS). It was deactivated after two weeks of intermittent operation [38]. Before the second laser campaign, in September 2003, an LRS software change resulted in continuous but degraded LRS operation. The degraded LRS measured CRS and laser spots continuously, but stars were only acquired and tracked during eclipse. No stars were measured in daylight. The LRS was designed to tie the LPA reference frame to the IST reference frame. Without continuous LRS star measurements, the LRS could not be used to transform laser measurements from the LPA reference frame into the IST reference frame. Significant modifications were made to the algorithm described in Chapter 6, particularly for the LRS. The modified algorithm was described in detail in reference [6].

B.1 IST Bracket Motion

Degraded LRS star measurements limited the SRS self-calibration capability described in Section 6.3.1. This place more emphasis on LRS measurements of the CRS and laser spots. These measurements included evidence of orbital variations of the spot positions. The CRS was attached to the IST mounting bracket. CRS spot motions reflected IST bracket motions. Smaller but similar motions of the laser spot suggested thermal variations of the GLAS optical bench due to sunlight. Early in the mission, the CRS and laser spot variations were incorporated into the processing algorithm [6].

The CRS signal was generated using green wavelength light from the GLAS laser. The energy of this light source decreased rapidly from January 2004. From the fall of 2004, the LRS was no longer able to measure the CRS spot. A batch-EKF correction method was developed to replace the CRS spot measurements [4]. It compared a batch method attitude with an EKF attitude. The batch method attitude was estimated using gyro measurements alone, so was independent from the IST bracket motion. The EKF attitude was estimated using IST measurement so included the bracket motion. The difference

between the two attitudes represented the IST bracket motion. IST measurements were corrected using the batch-EKF results.

B.2 Time-tag Problems in IST and SIRU Data

Several issues were found in the IST and SIRU time-tags: a 0.1 seconds IST time-tag shift, periodic SIRU rate spikes, SIRU data compression and bias. These problems caused anomalies in the attitude and pointing solutions. Analysis of the IST and SIRU data revealed the root causes and corrections were applied during reprocessing, as discussed in reference [2].

B.3 IST Sun-Blinding

ICESat's two primary attitude modes were sailboat mode and airplane mode. Each primary mode had two sub-modes separated by a 180° rotation. The primary mode was selected based on the beta prime angle (the angle between the orbit plane and the sun). Airplane mode was used when the absolute value of the beta prime angle was less than 33°. Sailboat mode was used otherwise. The IST was periodically blinded by the sun during airplane mode campaigns. For example, the sun-blinding data gaps on May 20, 2005 (beta prime angle $-20°$) were approximately 400 seconds long. On June 23, 2005 (beta prime angle $-4°$) the data gaps were approximately 700 seconds long. The IST was also intermittently blinded by the moon, usually for less than 100 seconds.

When the IST was blinded and star measurements were not available, attitude estimation was based on gyro data alone. The gyro data included errors from several sources including bias instability, scale factor error, and sense-axes misalignments. Attitude errors could grow to tens of arcseconds when using gyro data alone. There were several alternatives for improving attitude accuracy during IST blinding. One method was to use measurements from the BSTs, but this introduced uncertainty because the BSTs were pointed 30° away from the zenith. A method based on batch processing to estimate additional gyro parameters such as misalignments and scale factor errors resulted in better attitude estimates during data gaps [39]. A slight modification of the *variable interval* batch method [3] also provided good attitude estimates when the batch interval included approximately 100 seconds of star tracker data at the beginning and end of the data gap.

During IST data gaps, batch processing was used instead of the EKF. For verification, the batch estimates were compared to the EKF estimates for the BSTs [39]. The batch estimates were also compared to EKF estimates before and after the data gaps. This was particularly useful when the beta prime angle was near 0° and both of the BSTs were blinded as well, for example during June 2004.

B.4 Distortion Correction

Star measurements were represented in the GLA04 data as unit vectors in a tracker coordinate frame. Two methods were used to express the unit vectors. BST1 and BST2 output two scaled angles $k\theta_h$ and $k\theta_v$ where the scaling factor k converted from radians to arcseconds. To convert the angles to a unit vector y, an intermediate vector $x = [x_1\ x_2\ x_3]^T$ was

calculated with x_3 defined equal to one, x_1 defined as the horizontal coordinate h, and x_2 defined as the vertical coordinate v, so that $x = [h\ v\ 1]^T$ where

$$h \equiv x_1/x_3 = x_1/1 = \tan\theta_h$$
$$v \equiv x_2/x_3 = x_2/1 = \tan\theta_v$$

The unit vector y was then the normalized version of x

$$y = [h\ v\ 1]^T/(h^2 + v^2 + 1)^{1/2} \tag{B.1}$$

The native outputs of the IST and LRS were kh and kv. The IST and LRS performed the trigonometric calculations $h = \tan\theta_h$ and $v = \tan\theta_v$ internally. Because θ_h and θ_v were small angles, kh and kv were nearly equal to $k\theta_h$ and $k\theta_v$, but confusing the two types of output produced errors on the order of thirty arcseconds across an eight degree field of view. From GLA04 Release 24 (2005.12.21) onwards the IST values were converted from kh and kv to $k\theta_h$ and $k\theta_v$. If LRS star measurements are to be used, it is helpful to validate the LRS coordinates using a case where the IST and LRS are simultaneously measuring the same star. There is a ninety degree rotation between the IST and LRS coordinate frames. There is also a release dependent scaling factor for the LRS outputs, defined in the GLA04 release notes.

Distortion corrections were applied to the measured star unit vectors before use. The corrections were estimated using a least squares fit of third-order polynomials to a large sample of measurements. An iterative method was used to accumulate the factors $A \equiv H^T H$ and $B \equiv H^T y$ for the least squares solution, where $y = [y_1\ y_2]^T$ was an effective measurement. The iterations were initialized with $A_0 = 0_{20\times20}$ and $B_0 = 0_{20\times1}$. Given a measured unit vector $u = [u_1\ u_2\ (u_1^2+u_2^2)^{1/2}]^T$ and a predicted unit vector $v = [v_1\ v_2\ (v_1^2+v_2^2)^{1/2}]^T$ expressed in the tracker frame, the measurement components were $y_1 = u_1 - v_1$ and $y_2 = u_2 - v_2$. Two measurement models $y_1 = h_1\,x + \varepsilon_1$ and $y_2 = h_2\,x + \varepsilon_2$ were defined using a twenty-component vector of coefficients x and third-order polynomials

$$h_1 = [1\ \ u_1\ \ u_2\ \ u_1^2\ \ u_1u_2\ \ u_2^2\ \ u_1^3\ \ u_1^2u_2\ \ u_1u_2^2\ \ u_2^3\ \ 0_{1\times10}]$$
$$h_2 = [0_{1\times10}\ \ 1\ \ u_1\ \ u_2\ \ u_1^2\ \ u_1u_2\ \ u_2^2\ \ u_1^3\ \ u_1^2u_2\ \ u_1u_2^2\ \ u_2^3]$$

A_j and B_j were accumulated by

$$A_j = A_{j-1} + h_1^T h_1 + h_2^T h_2$$
$$B_j = B_{j-1} + h_1^T y_1 + h_2^T y_2$$

The estimated coefficients $\hat{x}$ were calculated using the least squares normal equation

$$\hat{x} = (H^T H)^{-1} H^T y = A^{-1} B$$

The corrected unit vector w for the measured unit vector u was then

$$\begin{aligned} w_1 &= u_1 - [1\ \ u_1\ \ u_2\ \ u_1^2\ \ u_1u_2\ \ u_2^2\ \ u_1^3\ \ u_1^2u2\ \ u_1u_2^2\ \ u_2^3][x_1 ... x_{10}]^T \\ w_2 &= u_2 - [1\ \ u_1\ \ u_2\ \ u_1^2\ \ u_1u_2\ \ u_2^2\ \ u_1^3\ \ u_1^2u2\ \ u_1u_2^2\ \ u_2^3][x_{11} ... x_{20}]^T \\ w &= [w_1\ \ w_2\ \ (w_1^2 + w_2^2)^{1/2}]^T \end{aligned}$$

Distortion correction magnitudes were up to 2.5 arcseconds for the IST and up to 5 arcseconds for the BSTs. Detailed descriptions of the distortion corrections are available in a reference [51].

B.5 Bad Star Removal

Predicted and measured star positions were compared and used to form star position residuals. The residuals were a direct measure of the attitude estimate accuracy. Daily mean values of the residuals were used to monitor estimation performance and in several cases were used to detect bad stars. The first case occurred during the fall 2003 laser campaign. The mean residual values were large on several days and were traced to a single star with large residuals. Excluding the star from the attitude estimation process resulted in normal mean residuals values. Here the definition of a bad star is a star with large residuals.

Figure B.1 shows the individual star position residuals over one orbit from 2008 day 50. The residuals are cutoff above twenty arcseconds because all such measurements were automatically rejected in an early stage of the processing. The residuals were generally less than ten arcseconds, but strong peaks are apparent near 10,800 seconds and 11,450 seconds. The individual stars that were being measured during the peaks were designated as possible bad stars or suspects. Means and standard deviations for the position residuals of individual suspects were then used to classify them as normal or bad. The bad stars were included in a list of stars that were automatically rejected in an early stage of processing. Figure B.2 corresponds to Figure B.1 but show the results after bad stars were detected and rejected.

A relatively small number of stars, less than one percent, were found to have statistically significant position and brightness biases, primarily due to nearby bright stars. These stars are discussed in detail in references [17] [52] [53].

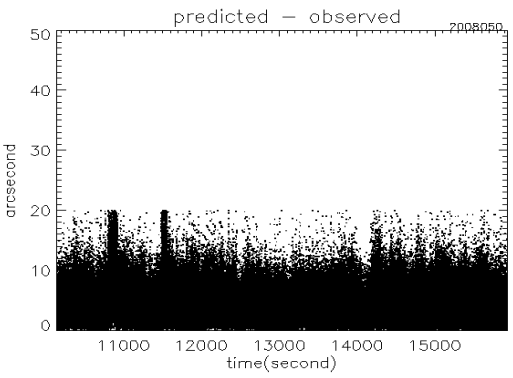

Figure B.1: Star position residual in day 50 of year 2008

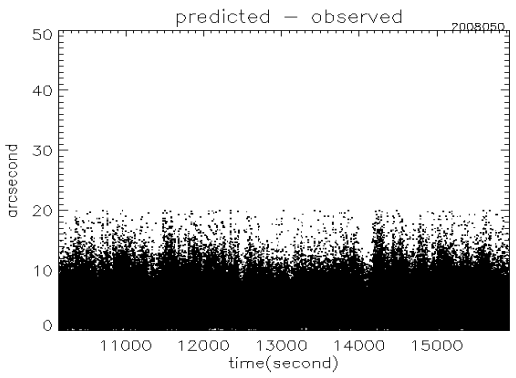

Figure B.2: Star position residual in day 50 of year 2008 after bad star removal

Appendix C

LPA IMAGE CHARACTERISTICS

The final PAD product was referred to as ANC09. It was generated daily and sent to GSFC where it was combined with orbit and range information to calculate earth surface elevation. ANC09 contained a time-series of PAD pointing vectors that were estimated using the algorithm described in Appendix B. It also contained parameters describing the laser images measured by the LPA. The parameters included centroid position, orientation, major-axis, eccentricity, and total intensity. Orientation was represented by two angles: angle of major-axis from LPA x-axis, and angle of major-axis from topocentric north. The parameters were calculated using algorithms in Source Extractor, a program designed to catalog objects in astronomical images [9].

LPA data consisted of images with 80x80 pixels at 40 Hz. The Stellar Reference System was designed to capture a portion of the laser energy within a 20x20 portion of the LPA. The image pixel intensity values represented the energy distribution in the laser beam.

LPA images of Laser 1 initially had an elliptical center with an irregular shape at one edge as shown in Figure C.1.* The irregular shape grew and detached from the central ellipse over about 30 days as shown in Figure C.2. Laser 2 laser images were elliptical like Laser 1, but without irregularities. An example of Laser 2 image is shown in Figure C.3. The ellipse orientation changes over time but the size and shape are almost consistent. Laser 3 laser images were roughly circular and constant over years of operation. Figure C.4 shows an example of Laser 3 laser image. LRS image is similar to LPA image except for a 90° rotation due to their coordinate rotations to each other [5].

LPA characteristics were calculated for all 40 Hz data. For each laser image, $1/e^2$ rule was applied as a cut off value : pixels having intensity less than a cut-off value were ignored. Daily averages of LPA characteristics were calculated from these 40 Hz output. Then campaign averages were calculated from the daily averages in each campaign. Figure C.5 shows changes of orientation (about LPA x-axis), major-axis and eccentricity of laser image, from L1 (2003) to L3k (2008) campaigns. Figure C.6 has intensity information: total intensity, maximum intensity, and number of pixels whose intensity are greater than cut-off values. Figure C.7 shows centroid coordinates of LPA images: in x-axis, in y-axis, and the overall distance from the LPA origin,(0,0). As indicated in Table A.2 of Appendix A, the major-axis value changed abruptly on day 54 of 2005. It explains

*LPA images are reconstructed using IDL from digitized numbers.

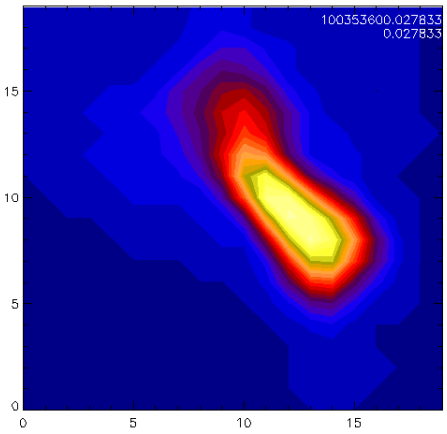

Figure C.1: Laser 1 LPA image (067/2003)

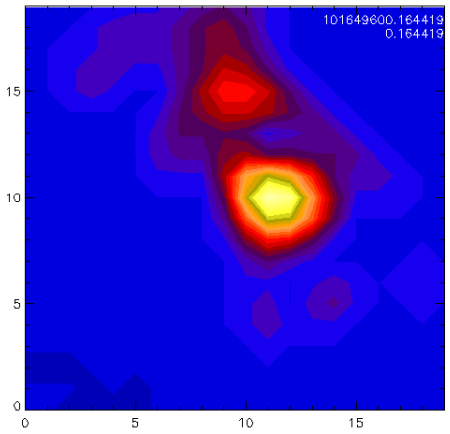

Figure C.2: Laser 1 LPA image (082/2003)

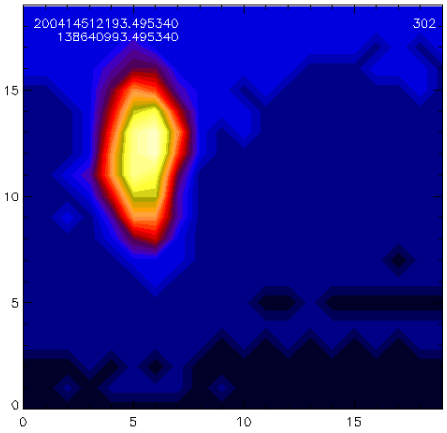

Figure C.3: Laser 2 LPA image (145/2004)

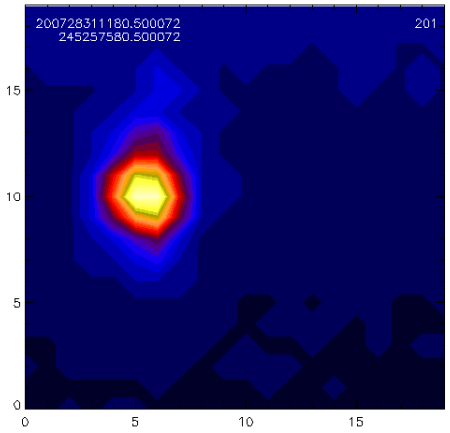

Figure C.4: Laser 3 LPA image (283/2007)

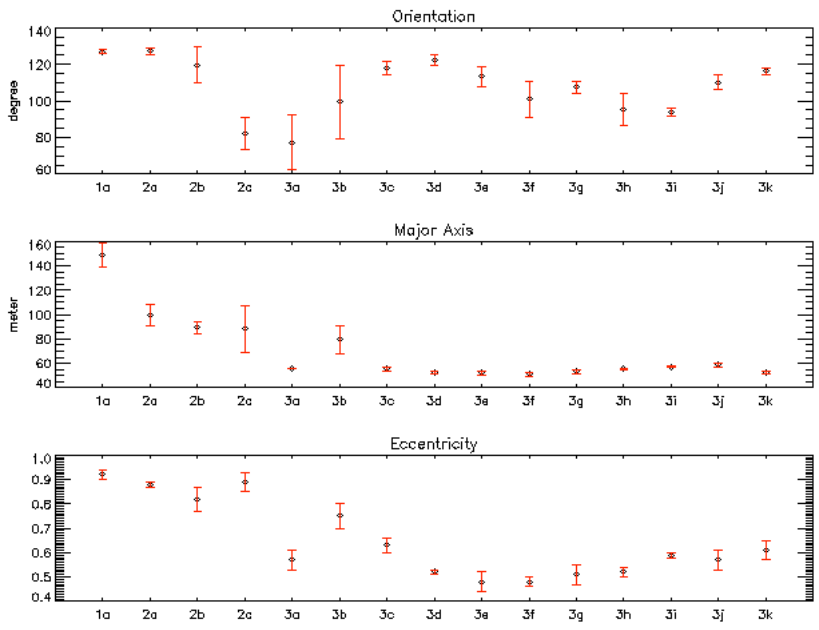

Figure C.5: LPA image characteristics : Campaign averages

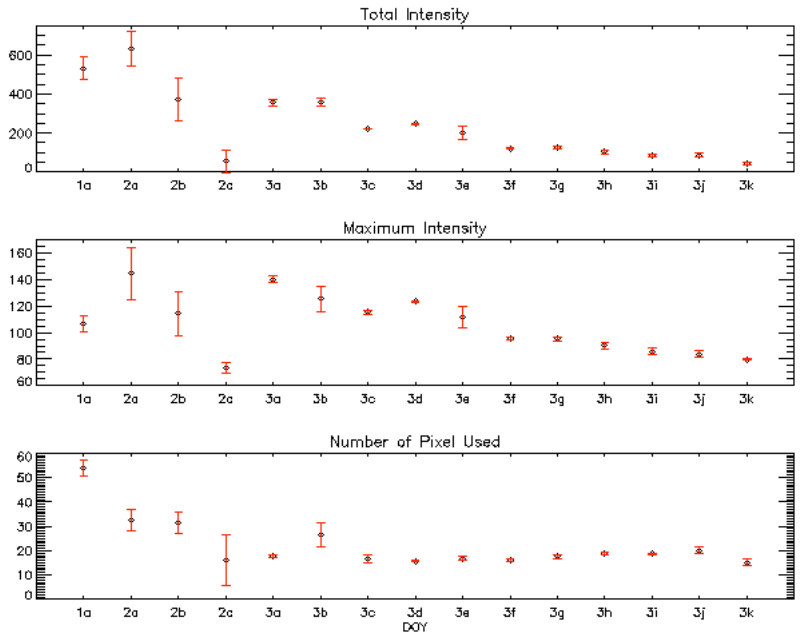

Figure C.6: LPA image characteristics : Campaign averages

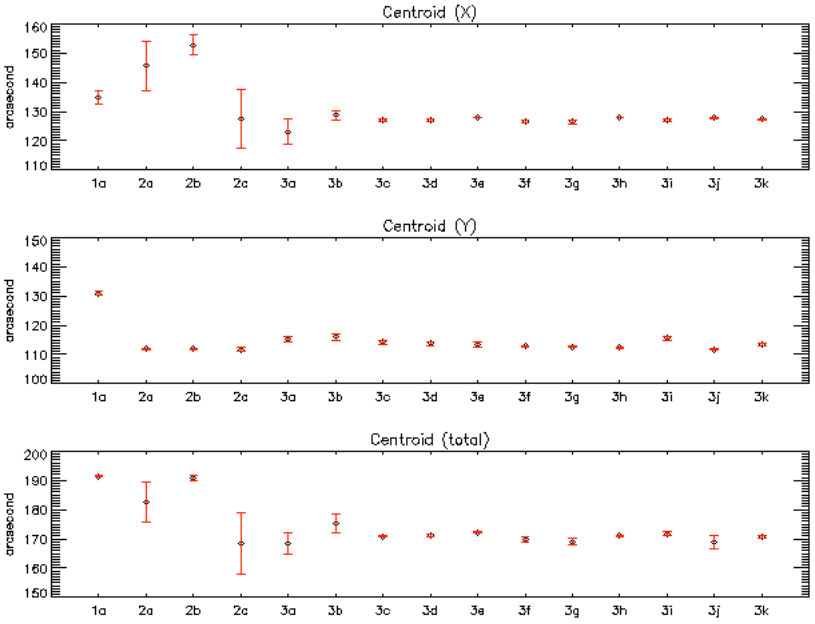

Figure C.7: LPA image characteristics : Campaign averages

abnormal jumps in major-axis and eccentricity plots for L3b campaign. The size of the image went to back down to previous range after L3b campaign. Daily variations of LPA characteristics in all laser campaigns are shown in Figure C.8, Figure C.9, and Figure C.10.

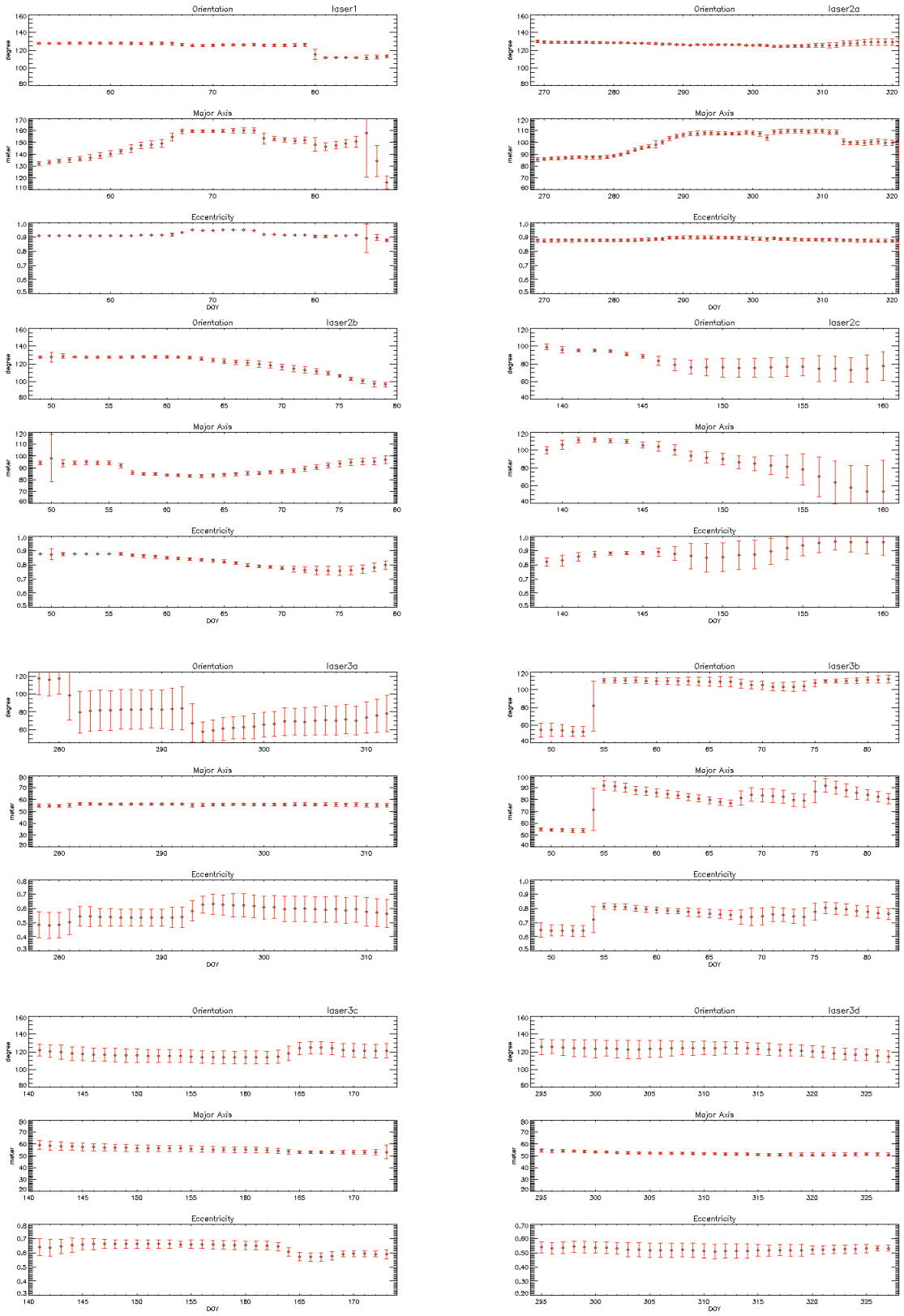
Orientation
laser1
degree
Major Axis
meter
Eccentricity
DOY
Orientation
laser2a
degree
Major Axis
meter
Eccentricity
DOY
Orientation
laser2b
degree
Major Axis
meter
Eccentricity
DOY
Orientation
laser2c
degree
Major Axis
meter
Eccentricity
DOY
Orientation
laser3a
degree
Major Axis
meter
Eccentricity
DOY
Orientation
laser3b
degree
Major Axis
meter
Eccentricity
DOY
Orientation
laser3c
degree
Major Axis
meter
Eccentricity
DOY
Orientation
laser3d
degree
Major Axis
meter
Eccentricity
DOY

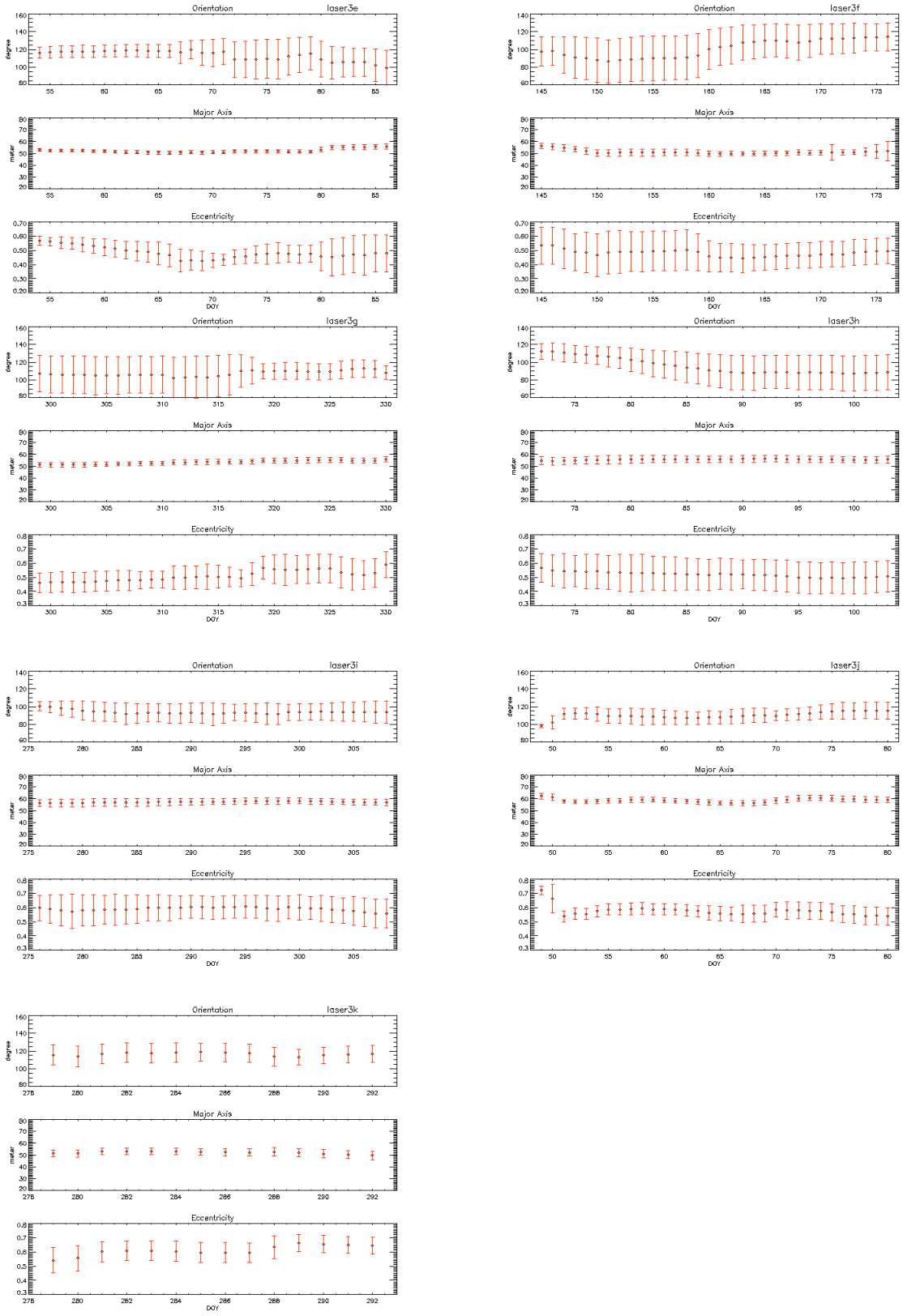

Figure C.8: LPA orientation, major-axis and eccentricity : daily averages

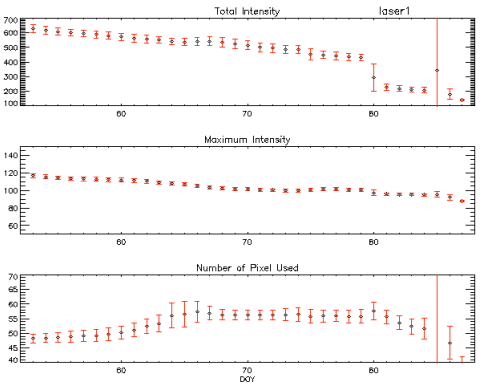
Total Intensity
laser1
Maximum Intensity
Number of Pixel Used
DOY

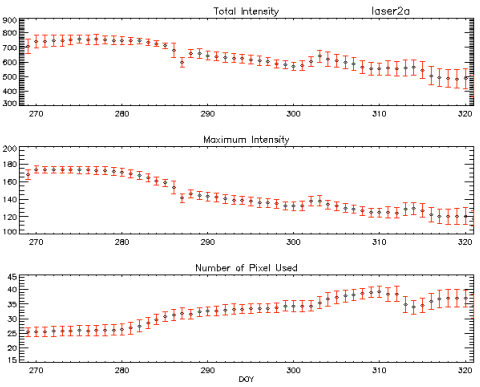
Total Intensity
laser2a
Maximum Intensity
Number of Pixel Used
DOY

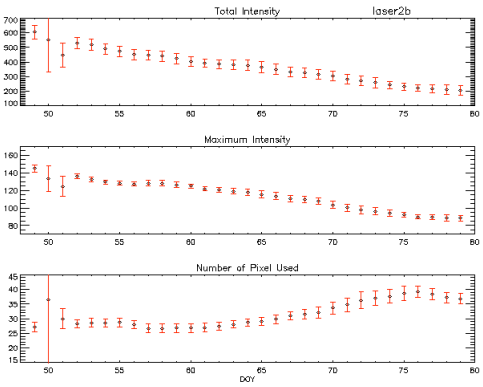
Total Intensity
laser2b
Maximum Intensity
Number of Pixel Used
DOY

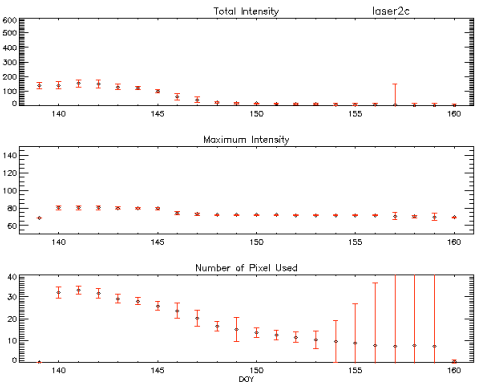
Total Intensity
laser2c
Maximum Intensity
Number of Pixel Used
DOY

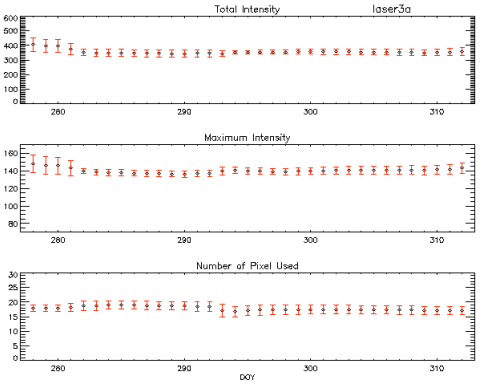
Total Intensity
laser3a
Maximum Intensity
Number of Pixel Used
DOY

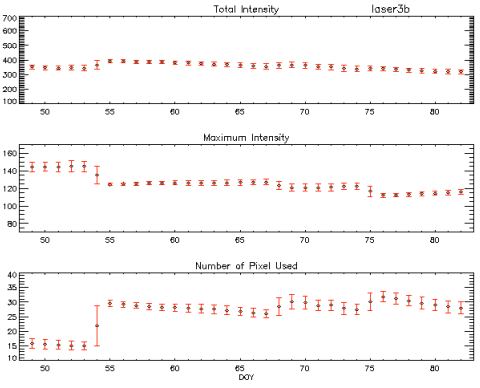
Total Intensity
laser3b
Maximum Intensity
Number of Pixel Used
DOY

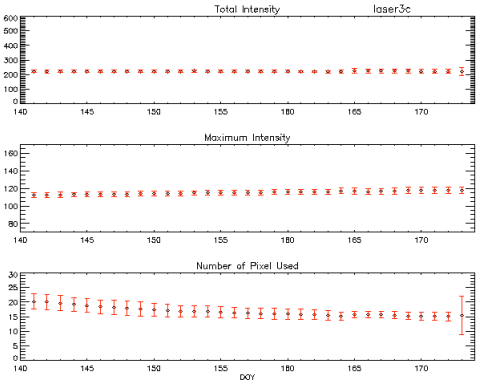
Total Intensity
laser3c
Maximum Intensity
Number of Pixel Used
DOY

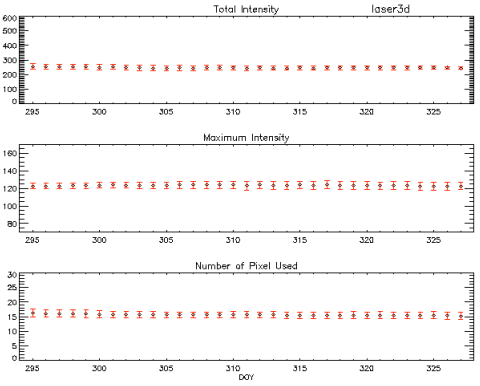
Total Intensity
laser3d
Maximum Intensity
Number of Pixel Used
DOY

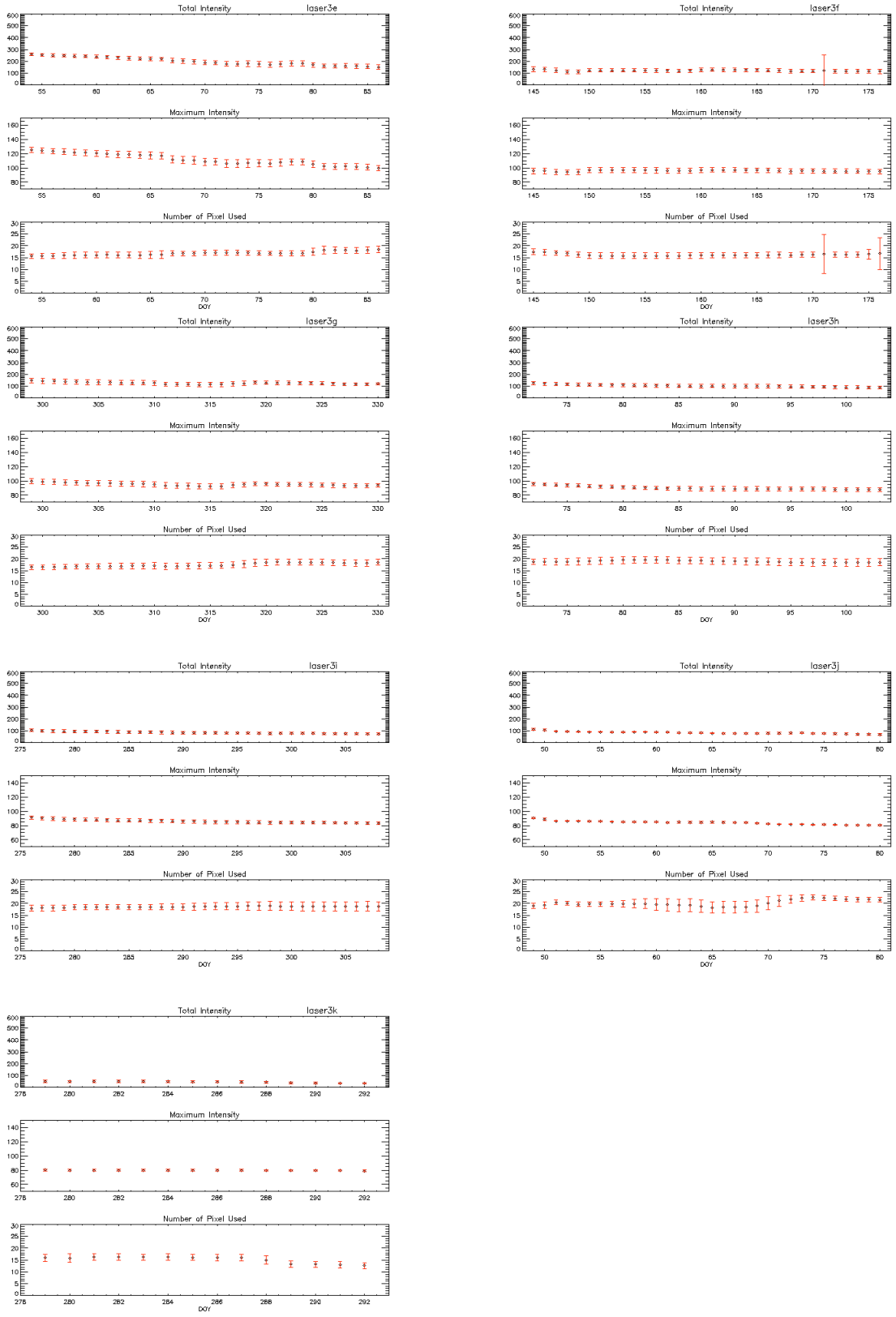

Figure C.9: LPA total intensity, maximum intensity, number of used pixels : daily averages

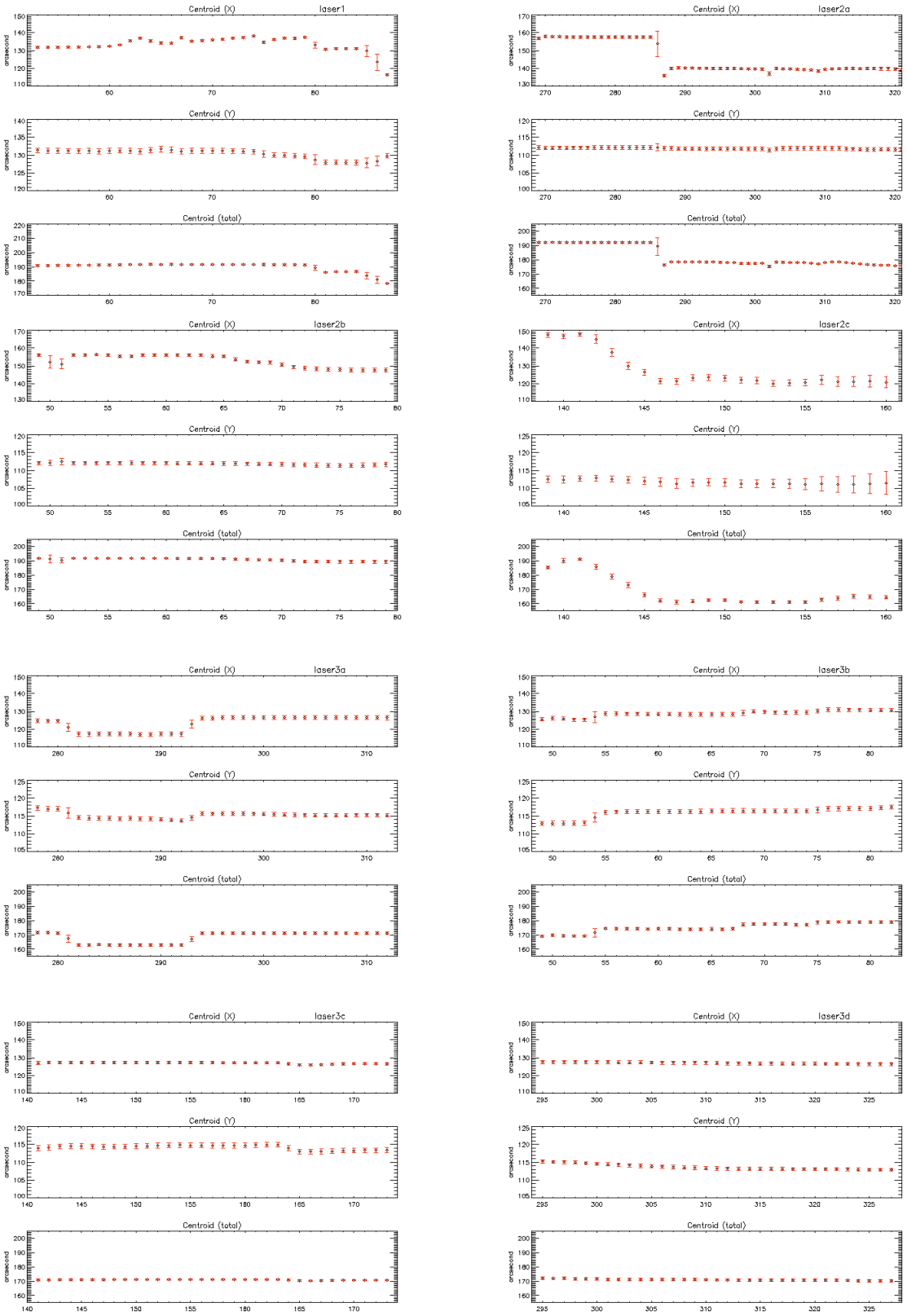
Centroid (X)
laser1
Centroid (Y)
Centroid (total)
laser2a
laser2b
laser2c
laser3a
laser3b
laser3c
laser3d
arcsecond

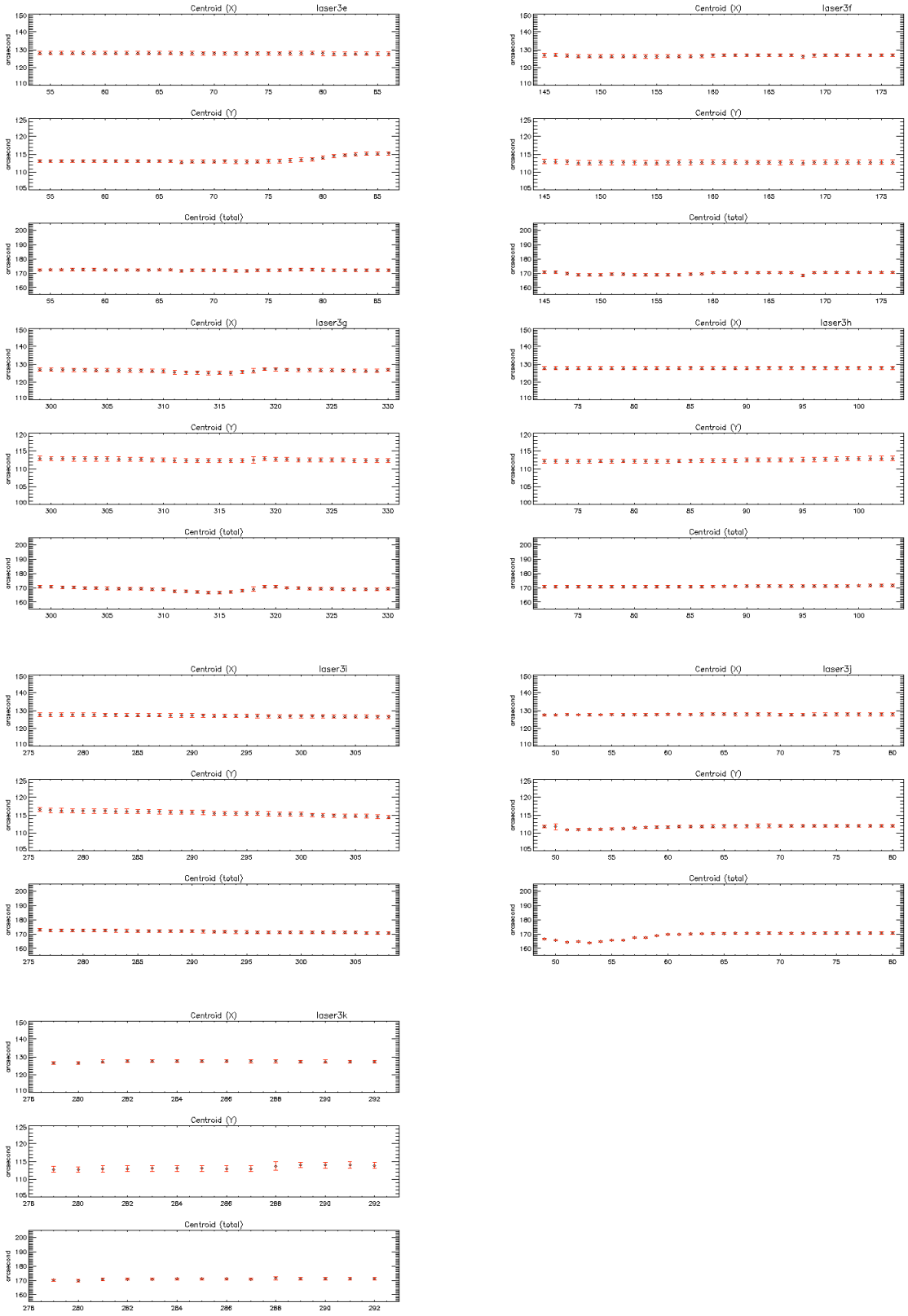

Figure C.10: LPA centroid location: in x-axis, in y-axis, from origin : daily averages

Appendix D

PROPERTIES OF QUATERNION

The four component quaternions are defined in Equation 2.1 with a constraint Equation 2.2. They are often divided into the three component vector, $\vec{q}$, and one scalar component, q_4 :

$$q = \begin{bmatrix} \vec{q} \\ q_4 \end{bmatrix} = [q_1, q_2, q_3, q_4]^T. \tag{D.1}$$

The inverse quaternion is defined as :

$$q^{-1} \equiv \begin{bmatrix} -\vec{q} \\ q_4 \end{bmatrix}. \tag{D.2}$$

This corresponds to the reverse rotation of the same amount of angle $\Delta\theta$ about the same rotation axis.

Quaternions, as well as Euler angles, can be used to construct 3×3 rotation matrix. Unlike the Euler angles, which have 12 different sets for the rotation matrix, quaternions have a unique combination for the rotation matrix such as :

$$C(q) = \begin{bmatrix} q_1^2 - q_2^2 - q_3^2 + q_4^2 & 2(q_1q_2 + q_3q_4) & 2(q_1q_3 - q_2q_4) \\ 2(q_1q_2 - q_3q_4) & -q_1^2 + q_2^2 - q_3^2 + q_4^2 & 2(q_2q_3 + q_1q_4) \\ 2(q_1q_3 + q_2q_4) & 2(q_2q_3 - q_1q_4) & -q_1^2 - q_2^2 + q_3^2 + q_4^2 \end{bmatrix}. \tag{D.3}$$

It is easy to see that the change of signs for all quaternions simultaneously does not affect the rotation matrix. Inversely,

$$\begin{aligned} q_1 &= \frac{1}{4q_4}(C_{23} - C_{32}) \\ q_2 &= \frac{1}{4q_4}(C_{31} - C_{13}) \\ q_3 &= \frac{1}{4q_4}(C_{12} - C_{21}) \\ q_4 &= \pm\frac{1}{2}(C_{11} + C_{22} + C_{33} + 1)^{1/2}, \end{aligned} \tag{D.4}$$

where C_{ij} is a matrix component in ith row and jth column. A computationally convenient algorithm has been developed as follows [45].

$$\begin{aligned} q_1^2 &= \frac{1}{4}(1+2C_{11}-T) \\ q_2^2 &= \frac{1}{4}(1+2C_{22}-T) \\ q_3^2 &= \frac{1}{4}(1+2C_{33}-T) \\ q_4^2 &= \frac{1}{4}(1+2C_{44}-T), \end{aligned} \tag{D.5}$$

where

$$T = C_{44} = trace\, C = C_{11} + C_{22} + C_{33} \tag{D.6}$$

and selects the q_i which has the largest absolute value assuming it to be positive. The other three q_j's can be obtained by dividing q_i into the appropriate three of the following six equations:

$$\begin{aligned} q_1 q_4 &= \frac{1}{4}(C_{23}-C_{32}) \qquad q_2 q_4 = \frac{1}{4}(C_{31}-C_{13}) \\ q_3 q_4 &= \frac{1}{4}(C_{12}-C_{21}) \qquad q_2 q_3 = \frac{1}{4}(C_{23}+C_{32}) \\ q_3 q_1 &= \frac{1}{4}(C_{31}+C_{13}) \qquad q_1 q_2 = \frac{1}{4}(C_{12}+C_{21}). \end{aligned} \tag{D.7}$$

One important property is the simple form for combining sequential rotations, q' and q'', into an equivalent single rotation, q, by

$$q = \begin{bmatrix} q_4'' & q_3'' & -q_2'' & q_1'' \\ -q_3'' & q_4'' & q_1'' & q_2'' \\ q_2'' & -q_1'' & q_4'' & q_3'' \\ -q_1'' & -q_2'' & -q_3'' & q_4'' \end{bmatrix} q'. \tag{D.8}$$

This is the quaternion composition that is usually written as the following form

$$q = q'' \otimes q' \tag{D.9}$$

using *natural* order, while some literatures prefer to write the same equation as

$$q = q' \odot q'' \tag{D.10}$$

using *historical* order. Thus any set of q's can be solved universally as a simple, nonsingular, bilinear combination of the other two. The matrix representation for quaternion composition is

$$C(q) = C(q'')C(q'). \tag{D.11}$$

Therefore, many equations for quaternion computation are easily derived using the rotation matrix manipulations.

From the definition in Equation 2.1, quaternions can also be parameterized in terms of the Euler angles :

$$\begin{aligned} q(\hat{\mathbf{1}},\theta) &= [\sin(\theta/2)\ 0\ 0\ \cos(\theta/2)]^T \\ q(\hat{\mathbf{2}},\theta) &= [0\ \sin(\theta/2)\ 0\ \cos(\theta/2)]^T \\ q(\hat{\mathbf{3}},\theta) &= [0\ 0\ \sin(\theta/2)\ \cos(\theta/2)]^T, \end{aligned} \tag{D.12}$$

where θ is a rotated angle and $\hat{1}$,$\hat{2}$,$\hat{3}$ are rotation axes employed sequentially. For example, the 3-1-3 Euler angles rotation can be written as

$$\begin{aligned} q_{313}(\theta_1, \theta_2, \theta_3) &= q(\hat{\mathbf{3}}, \theta_3) \otimes q(\hat{\mathbf{1}}, \theta_2) \otimes q(\hat{\mathbf{3}}, \theta_1) \\ &= \begin{bmatrix} \sin\theta_2 \cos(\theta_1 - \theta_3) \\ \sin\theta_2 \sin(\theta_1 - \theta_3) \\ \cos\theta_2 \sin(\theta_1 + \theta_3) \\ \cos\theta_2 \cos(\theta_1 + \theta_3) \end{bmatrix}. \end{aligned} \tag{D.13}$$

To convert quaternions to Euler angles, the rotation matrix must first be calculated from quaternions by Equation D.3. Then, the Euler angles are derived from the rotation matrix according to the chosen set of Euler angle sequences.

To transform Euler angles to quaternions, the inverse process of the previous method can be used. A more convenient way for use in computer programming is as follows [22] :

$$\begin{bmatrix} \dot{q}_4 \\ \dot{q}_1 \\ \dot{q}_2 \\ \dot{q}_3 \end{bmatrix} = R \begin{bmatrix} 1 \\ 0 \\ 0 \\ 0 \end{bmatrix}, \tag{D.14}$$

where

$$R = (\cos\frac{1}{2}\theta_1 R_4 + \sin\frac{1}{2}\theta_1 R_3)(\cos\frac{1}{2}\theta_2 R_4 + \sin\frac{1}{2}\theta_2 R_2)(\cos\frac{1}{2}\theta_3 R_4 + \sin\frac{1}{2}\theta_3 R_1) \tag{D.15}$$

and

$$\begin{aligned} R_1 &= \frac{1}{2}\begin{bmatrix} 0 & -1 & 0 & 0 \\ 1 & 0 & 0 & 0 \\ 0 & 0 & 0 & 1 \\ 0 & 0 & -1 & 0 \end{bmatrix} \qquad R_2 = \frac{1}{2}\begin{bmatrix} 0 & 0 & -1 & 0 \\ 0 & 0 & 0 & -1 \\ 1 & 0 & 0 & 0 \\ 0 & 1 & 0 & 0 \end{bmatrix} \\ R_3 &= \frac{1}{2}\begin{bmatrix} 0 & 0 & 0 & -1 \\ 0 & 0 & 1 & 0 \\ 0 & -1 & 0 & 0 \\ 1 & 0 & 0 & 0 \end{bmatrix} \qquad R_4 = \frac{1}{2}\begin{bmatrix} 1 & 0 & 0 & 0 \\ 0 & 1 & 0 & 0 \\ 0 & 0 & 1 & 0 \\ 0 & 0 & 0 & 1 \end{bmatrix}. \end{aligned}$$